From Terminus to Sill: Feedbacks between Fjord Stratification, Subglacial Discharge, and Glacier Ice

by

Nicole Lanier Abib

A dissertation accepted and approved in partial fulfillment of the

requirements for the degree of

Doctor of Philosophy

in Earth Sciences

Dissertation Committee:

David Sutherland, Chair

Jason Amundson, Core Member

Alan Rempel, Core Member

Valerie Sahakian, Core Member

Sarah Cooley, Institutional Representative

University of Oregon

Spring 2024

DISSERTATION ABSTRACT

Nicole Lanier Abib

Doctor of Philosophy in Earth Sciences

Title: From Terminus to Sill: Feedbacks between Fjord Stratification, Subglacial Discharge, and Glacier Ice

Mass loss from tidewater glaciers worldwide has increased in recent decades, partially attributed to changes occurring at the ice-ocean interface. The melting of the Greenland and Antarctic Ice Sheets have contributed up 14 mm of sea level rise over the past 20 years, and there remains large uncertainty into how these numbers will evolve into the future. At present, ~one-half of the ice lost annually from the Greenland Ice Sheet is due to frontal ablation, or the combination of submarine melting and iceberg calving, with similar percentages observed in Antarctica and other locations where glaciers reach the ocean. Frontal ablation changes the geometry of a glacier's terminus, influencing glacier dynamics, the fate of upwelling plumes, and the distribution of submarine meltwater input into the ocean. Directly observing frontal ablation and terminus morphology below the waterline is difficult, however, limiting our understanding of these coupled ice-ocean processes.

In this dissertation, I use both remotely sensed and field-based observations to investigate the processes that contribute to tidewater glacier evolution. In Chapter II, I combine 3-D multibeam point clouds of the subsurface ice face at LeConte Glacier, Alaska, with concurrent environmental conditions to show that the terminus morphology is predominately overcut despite high multibeam sonar-derived melt rates. This finding challenges the assumption that tidewater glacier termini are largely undercut during periods of high submarine melting and suggests that important glacier-ocean feedbacks are missing from current submarine melt rate theory.

In Chapter III and IV, I examine one currently understudied piece of glacial fjord dynamics – the input of meltwater from ice mélange in the upper layers of the water column. I use field observations collected before and after an ephemeral ice mélange event in front of Kangilliup Sermia, Greenland, to directly investigate the extent to which ice mélange meltwater can modify glacier-adjacent water properties. I show that ice mélange can cause substantial cooling and freshening of the water column, leading to a stratification change down to the depth of the outflowing discharge plume and substantial modification of upper layer hydrography. I then expand this analysis to a suite of glacial fjords in Central West Greenland to investigate the conditions under which ice mélange forms and dissipates, finding that for glacial fjords with a deep grounding line, ice mélange breakup date is highly correlated with subglacial discharge plume evolution. This implies that future changes to ocean stratification or subglacial discharge magnitude will alter the duration over which ice mélange is present, thereby changing the timing of its meltwater injection into the proglacial fjords on which it sits and the length of time it is able to supply buttressing force to glacier termini.

This dissertation includes previously published and unpublished co-authored material.

ACKNOWLEDGMENTS

I would like to first thank my advisor, Dave Sutherland, who has provided me with the guidance, mentorship, and resources that I have needed to be successful during my Ph.D. Dave has always encouraged me to take ownership of my dissertation: urging me to explore the research ideas that interest me the most, attend field expeditions that stretch the limits of my knowledge on ice-ocean interactions, and to be a kind and inquisitive collaborator. My growth as a scientist and a person has been exponential working with him.

I feel lucky to have many colleagues who have served as unofficial advisors to me, including but not limited to Jason Amundson, Fiamma Straneo, and Erin Pettit. Despite having no real obligation to help me with my graduate degree, they were always available to answer my questions on glaciers, the ocean, and academia as a whole. Knowing that they believed in my capabilities pushed me through on those days when imposter syndrome tried to get the best of me.

Similarly, the support and friendship I have found in my fellow early career colleagues at UO, OSU, and beyond, has been the essential ingredient to this Ph.D. Throughout the years, the Ocean-Ice Lab Group has been an oasis of glacio-oceanography nerdiness at UO, and I am grateful for all of the belly-laughs and chalkboard sessions we have had. Beyond my lab group, I want to thank the 2019 new graduate student cohort. Immediately going through a pandemic after starting graduate school would have been entirely different without their continual efforts to maintain community in the Zoom World. In addition, I spent the first two years of my degree taking classes at OSU, and I feel fortunate to have found a second cohort of physical oceanographers and glaciologists to journey through graduate school with there.

I want to thank my additional committee members, Valerie Sahakian, Alan Rempel, and Sarah Cooley, for their guidance and suggestions during my Ph.D. I always looked forward to our committee meetings and lively discussions. I am also deeply appreciative of the UO ERTH Front Office Staff, Marla Trox, Dave Stemple, and Sandy Thoms, who work tirelessly behind the scenes to ensure our degrees and research go as smoothly as possible.

Throughout my Ph.D., I attended several summer courses that aided my growth as an interdisciplinary scientist. I am most grateful to the ICESat-2 HackWeek at University of Washington and the Greenland Ice Sheet Ocean Science Network Summer School for providing me with the tools to access new data sources and collaborate across scientific disciplines. I also want to thank the several scientific organizations who have given me the opportunity to present my research to fellow scientists throughout my degree, such as the American Geophysical Union and the International Glaciological Society. I have always appreciated the focus on early career presenters at these conferences, and these opportunities have given me the chance to become a better science communicator.

My support network during my Ph.D. has extended far beyond Oregon, and I would be remiss to not thank my family, friends, and mentors from previous life stages. Mom and Dad, thank you for supporting my dream of studying how ice melts, even when it takes me to far away places (come visit AK anytime!). Claire, the last year of my Ph.D. was only doable with your support, love, and wacky ideas about how we should be studying glaciers. To my friends and mentors from Madeira, Cornell, and Duke, I appreciate your never-ending belief in me.

Finally, I want to acknowledge the several funding sources that made this Ph.D. possible, including the UO Department of Earth Sciences, the National Science Foundation, and the National Aeronautics and Space Administration FINESST fellowship.

DEDICATION

This dissertation is dedicated to Parker, without whom this Ph.D. would not have been possible.

TABLE OF CONTENTS

Chapter Page

I. INTRODUCTION 19

II. PERSISTENT OVERCUT REGIONS DOMINATE THE TERMINUS MORPHOLOGY OF A RAPIDLY MELTING TIDEWATER GLACIER 23

2.1 Introduction 23
2.1.1 Physical setting 27
2.2 Methods 28
2.2.1 Submarine glacier morphology 28
2.2.2 Subaerial glacier morphology 30
2.2.3 Ice velocity 31
2.2.4 Glacier change in time 32
2.2.5 Environmental forcing 34
2.3 Results 36
2.3.1 Glacier morphology and change in time 36
2.3.2 Environmental forcings 42
2.4 Discussion 44
2.4.1 Persistent overcutting across the glacier terminus 44
2.4.2 Seasonal overcutting in the vicinity of a subglacial discharge outlet 46
2.4.3 An example of extreme overcutting: submarine ice ramps 48
2.4.4 Further evidence for elevated submarine melt rates 50
2.4.5 Implications of overcut terminus morphology on plume-melt theory 52
2.5 Conclusions 54
2.6 Bridge 56

III. ICE MÉLANGE MELT DRIVES CHANGES IN OBSERVED WATER COLUMN STRATIFICATION AT A TIDEWATER GLACIER IN GREENLAND 57

3.1 Introduction 57
3.1.1 Physical setting 60
3.2 Materials and methods 62
3.2.1 Ship-based observations 62

3.2.2 Subglacial plume model 63
3.2.3 Ice mélange melt rate 64
3.3 Results 66
3.4 Discussion 71
3.4.1 Alternative water column transformation mechanisms do not explain stratification change 72
3.4.2 Short-term ice mélange events as a driver of water column change 73
3.4.3 Implications for fjords with summertime ice mélange 76
3.5 Conclusions 79
3.6 Bridge 80
IV. SUBGLACIAL DISCHARGE DRIVES ICE MÉLANGE BREAKUP AT DEEPLY GROUNDED GLACIERS 81
4.1 Introduction 81
4.1.1 Physical Setting 86
4.2 Methods 87
4.2.1 Ice Mélange Characteristics 87
4.2.2 Environmental, Dynamic, and Geometric Forcings 89
4.2.3 Subglacial Plume Model 91
4.3 Results 92
4.3.1 Ice mélange in the Uummannaq region 92
4.3.2 Environmental, Dynamic, and Geometric Forcings 97
4.4 Discussion 100
4.4.1 Iceberg keel depth varies with glacier geometry 101
4.4.2 Ice mélange duration depends primarily on ice mélange breakup processes 102
4.4.3 Subglacial discharge drives ice mélange breakup at deeply grounded glaciers . 105
4.4.4 Case Study: Basin wide ocean cooling leads to a change in ice mélange regime 108
4.5 Conclusions 112
V. CONCLUSIONS 115
APPENDICES
VI. CHAPTER II: ADDITIONAL INFORMATION ON ICE VELOCITY AND ENVIRONMENTAL CONDITIONS AT LECONTE GLACIER 118

A.1 Ice Velocity and Environmental Conditions 118
A.2 Supplementary Movie Captions 121
VII. CHAPTER III: ADDITIONAL INFORMATION ON OCEAN HYDROGRAPHY AND SUBGLACIAL DISCHARGE IN FRONT OF KANGILLIUP SERMIA 122
VIII. CHAPTER IV: ADDITIONAL INFORMATION ON ENVIRONMENTAL FORCINGS IN THE UUMMANNAQ REGION 128

LIST OF FIGURES

Figure Page

Figure 2.1. Study area. (a) Sentinel 2-A image of LeConte Glacier and Bay in September 2018 with markers indicating the location of the terrestrial radar interferometer and the upper time-lapse cameras (yellow square), the lower time-lapse cameras (yellow triangle), as well as the collected multibeam point clouds (Black: August 2016, Red: May 2017, Blue: September 2018). An example reference transect (black line) and rotated coordinate system (red dashed lines) is shown overtop the glacier. Map is referenced to UTM Zone 8N and inset shows location of LeConte Glacier in southeast Alaska. (b) Example output from multibeam sonar showing the subaerial and submarine terminus geometry, gridded bathymetry, and reference plane used for projection and gridding of the point clouds (grey rectangle). Image of the subaerial terminus was acquired from UAV imagery and manually lined up with the submarine terminus. Dashed lines correspond with the transects taken for panels a, b, and c in Fig. 2, and all vertical transects are shown in a Supplementary Video..... 28

Figure 2.2. Short term changes in terminus morphology for August 2016 (top), May 2017 (middle), and September 2018 (bottom). (a) Across glacier cross-section taken from 100-110 m depth. Each color indicates a different multibeam scan. (b) Vertical cross-section taken at 490-510 m across-glacier (Line A, north side of terminus, Fig. 1b). (c) Vertical cross-section taken at 200-220 m across-glacier (Line B, south side of terminus, Fig. 1b). All vertical cross-sections are shown in a Supplementary Video. 38

Figure 2.3. (a) Percentage of the terminus that is overcut (red line), vertical (black line), and undercut (blue line) over time in the field campaigns in August 2016 (top), May 2017 (middle), and September 2018 (bottom). Circle markers indicate the time at which multibeam data was collected. (b) The average percent overcut (red), vertical (black), and undercut (blue) over the duration of the field campaign with error bars indicating ± 1 standard deviation..... 38

Figure 2.4 Average vertical terminus slope for August 2016 (top), May 2017 (middle), and September 2018 (bottom). (a) Variation in terminus slope with depth, error bars indicate ± 1 standard deviation. (b) Average terminus slope for each grid cell across the entire glacier terminus. (c) Variation in terminus slope across the width of the glacier. The brown shaded region indicates the bed along the grounding line of the glacier, and the black rectangle indicates the location of the likely subglacial discharge outlet, based on hydropotential analysis (Fig. 7). Angles < 0 (blue) are undercut, whereas angles > 0 (red) are overcut regions of the terminus..... 39

Figure 2.5 Plan view of average frontal ablation rates across the glacier terminus in (a) August 2016, (b) May 2017, and (c) September 2018. The brown shaded region indicates the bed along the grounding line of the glacier, and the black rectangle indicates the location of the likely subglacial discharge outlet, based on hydropotential analysis (Fig. 7). The average vertical angle is shown in red-blue color scale above the average frontal ablation rates, where angles < 0 (blue) are undercut, whereas angles > 0 (red) are overcut regions of the terminus..... 40

Figure 2.6 Average submarine melt rate with depth. Error bars indicate ± 1 standard deviation. Comparison to Sutherland and others (2019) is shown in dashed lines. The vertical shaded region shows the terminus area average value for each field campaign. 41

Figure 2.7 Overview of environmental forcings. (a) Summary of ocean temperature beneath 75m depth for August 2016, May 2017, and September 2018. (b) Summary of subglacial discharge for 2016, 2017, and 2018. (c) Likely subglacial discharge channels as predicted by the hydropotential analysis (red-yellow color scale) and location of CTD casts taken in the proglacial fjord overlaid on top of our study area map. Channels marked by 1 and 2 indicate the discharge outlets with the highest and second highest upstream flow contribution respectively..... 43

Figure 3.1: (a) True color Landsat 8 image from 07 August 2014, showing the proglacial fjords of Kangilliup Sermia (RNK) and Kangerlussuup Sermia (KAS) overlaid by the location of repeat CTD transects (red line), mooring deployed outside of sill (red triangle), meteorological station (red circle), and time-lapse camera (red square). Red arrow shows direction of riverine sediment plume deflection and inset shows location of image in Greenland. (b) Imagery from a time-lapse camera (full video in supplement) shows how the ice mélange forms over the course of 6 hours in front of Kangilliup Sermia following an iceberg calving event on 05 August 2014. (c) Thalweg bathymetry of Kangilliup Sermia and Kangerlussuup Sermia extracted from BedMachine v5 (Morlighem et al., 2017, 2022). 61

Figure 3.2: Changes in T (a), S (b), and N^2 (c) pre- (black line; August 4) and post-event (blue line; August 11; full profiles shown in Fig. S1). Thin lines indicate individual CTD casts across the width of the glacial fjord, while thick lines indicate the average. In (c), N^2 has been smoothed with a 10 m moving average. 68

Figure 3.3: (a) Average water column properties pre- (black dots) and post-event (blue dots) overlaid on isopycnal contours (density in kg m^{-3} –1000). Mixing lines between freshwater discharge (dashed lines) and submarine melting of ice

(solid lines) with ambient ocean water are included, and a white square marker indicates the depth at 50 m intervals between 0-800 m. Roman numerals correspond with locations described in text. (b) Zoom-in on (a) with data only shown between depths of 50-100 m. (c) Gridded ADCP-derived along-fjord velocity on August 11, 2014, with positive values indicating flow toward the glacier and a black contour at 0 m s^{-1}. Distance across fjord increases from southward. The location of the predicted minimum (93 m), maximum (235 m), and mean (158 m) depth of neutral buoyancy of the subglacial discharge plume is shown (black dashed lines). 69

Figure 3.4 Full-depth water column properties outside of the sill (a) and near the termini of Kangilliup Sermia (b) and Kangerlussuup Sermia (c) in T-S space, with water column properties colored by depth in the water column. Mixing lines with freshwater runoff (dashed line) and submarine meltwater (solid line) are superimposed. 79

Figure 4.1 Study area map of the Uummannaq region with the inset showing the location relative to Greenland. Background imagery is from a composite of two Landsat-8 images taken on September 19 and 21, 2018. Bathymetry from BedMachine v5 is shown in the blue-green colormap. The terminus position in 2017 is shown as a purple line, and the hydrographic casts used in the plume model are shown as red dots. A day of year to month conversion calendar is shown in inset for reference 85

Figure 4.2 Seasonal ice mélange breakup day (A), formation day (B), and duration (C) for all study fjords. Formation date often spans across the new year, so 366 days were added to formation dates less than day 100 to enable easier interannual comparison. Boxes indicate the 25th to 75th percentile of the data, while whiskers show the full range of the data not considered outliers, which are indicated by black dots. 93

Figure 4.3 Ice mélange duration (A), breakup date (B), formation date (C), JJA average subglacial discharge (D), and DJF average air temperature (E) for each study glacier in the Uummannaq region. Formation date often spans across the new year, so 366 days were added to formation dates less than day 100 to enable easier interannual comparison. It is possible for ice mélange to undergo a seasonal cycle where it forms early in the year (doy < 100), breaks up in the summer melt season, and reforms before the start of the next year, which will appear as multiple formation dates for one calendar year in panel (C). 95

Figure 4.4. Iceberg drafts within the ice mélange for study glaciers with available ArcticDEM strips. Each grey bar indicates the distribution from one DEM, with darker shading suggesting a higher likelihood that icebergs occupy that depth bin. Blue dashed lines indicate the maximum depth of the grounding line, with the grounding line depths for UMI (496m), RNK (1,033 m), SIL (556 m), and STR (485 m) beyond the plot limits. 96

Figure 4.5. Overview of investigated environmental forcings between 2013-2021 for each study glacier: (A) DJF air temperature, (B) JJA subglacial discharge, and (C) JJA ice flux. Boxes indicate the 25th to 75th percentile of the data, while whiskers show the full range of the data not considered outliers, which are indicated by black dots..... 98

Figure 4.6. Overview of plume modeling inputs and outputs, with the conservative temperature (A) and absolute salinity (B) shown with the effective depth of the fjord indicated as a square marker. The effective depth for RNK is beyond the plot limit at 703 m. The derived plume neutral buoyancy depth (Znb) for tested values of subglacial discharge is shown (C) with the neural buoyancy depth that corresponds with the average JJA subglacial discharge value shown as a square marker..... 100

Figure 4.7. T2M (A), Runoff (B), and Neutral Buoyancy Depth (C) index for each fjord studied in the Uummannaq region against maximum grounding line depth, with square markers indicating the average over the study period and error bars indicating ± 1 standard deviation. T2M index (A) is the number of days between air temperatures rising above 0 °C and ice mélange breakup, while runoff index and Znb indices are the number of days between subglacial discharge start (B) or the plume reaching the mean iceberg keel depth (C) and ice mélange breakup. 105

Figure 4.8. Example of time series of plume neutral buoyancy depth (black lines with red shading for +/- 1 standard deviation) for LIL (top) and STR (bottom) overlaid on seasonal ice mélange presence/absence data (grey shading, with grey indicating seasonal ice mélange is present) and the average iceberg keel depth within the ice mélange (blue shading) for the entire study period (left) and two annual subsections (middle and right). A figure with all glaciers represented is shown in the supplement (Figure S-9). 107

Figure 4.9. (A) Summer ocean temperature at 250 m in the Uummannaq trough with ± 1 standard deviation indicated superimposed with ice mélange breakup day at SIL. Summer temperature was determined as the average temperature between 240 – 260 m for all available OMG shipboard CTD and AXCTD casts in the trough. (B) Mean JJA subglacial discharge with ± 1 standard deviation indicated by error bars. (C) Ice mélange velocities from April 16, 2020 with lateral boundaries of the sill superimposed (yellow dotted line) as defined by a 500 m deep isobath. (D) Sentinel 2 image from August 25, 2019, showing compressive arches between mid-fjord grounded icebergs and fjord walls. 110

Figure A.1 Campaign averaged ice velocity fields derived using the Terrestrial Radar Interferometer in August 2016 (a) and May 2017 (b) and drone imagery in September 2018 (c) with the reference transect superimposed (black line). For frontal ablation calculations, ice velocities were extracted across a transect

that was as close to the terminus as possible while still capturing a complete across-glacier profile (d). 118

Figure A.2 Change in waterline position between each multibeam pass derived from TRI in August 2016 (a) and May 2017 (b), and time-lapse imagery in September 2018 (c). Thick black line indicates the average waterline ablation between all multibeam passes. Horizontal line at 20 m/d in August 2016 and 10 m/d in May 2017 and September 2018 show the threshold used for the characteristic calving rate in the separation of frontal ablation between iceberg calving and submarine melting. 119

Figure A.3 (a) Hydrographic data collected by the CTD casts located in Fig. 7c shown in T-S space and overlaid with melt and runoff mixing lines. Profiles of temperature (b) and salinity (c) with depth from the same CTD casts. Ocean temperature and salinity data were averaged from 75m depth (horizontal black line) to the grounding line to remove the influence of the outflowing glacially modified plume. 120

Figure A.4 (a) Time series of air temperature (top row) and precipitation (middle row) taken from Petersburg Airport used to force the subglacial discharge model (bottom row) over the course of all field campaigns (August 2016: black dashed line, May 2017: red dashed line, September 2018: blue dashed line). (b) The same time series zoomed into the dates of each field campaign, with the bolded lines indicating the time period of multibeam data collection. 121

Figure B.1 Changes in T (a), S (b), and N2 (c) pre- (black line; August 4) and post-event (blue line; August 11; zoomed in profiles shown in Figure 2). Thin lines indicate individual CTD casts across the width of the glacial fjord, while thick lines indicate the average. In (c), N2 has been smoothed with a 10 m moving average. 122

Figure B.2 Across-fjord averaged water column properties before (orange, black, and purple dots) and after (blue dots) the ephemeral ice mélange event in the (a) depth range of significant stratification change and (b) in the surface water column. 123

Figure B.3 (a) ADCP-derived ocean velocities averaged over the northern half, southern half, and total width of the fjord. (b) Modeled iceberg melt rates averaged across all depth classes for each average ocean velocity profile with error bars indicating ± 1 standard deviation (thin lines) and keel-depth averaged iceberg melt rate for an iceberg that extends 200 m into the water column (thick lines). 123

Figure B.4 Gridded SADCP-derived along-fjord velocities prior to the ice mélange event (August 3) and after the ice mélange event (August 10) taken at the hydrographic transect in Figure 1a. Positive values indicate glacierward flow,

and a black contour is present at 0 m/s. The surface recirculation is strongest just after the ice mélange event but is present in all water column velocity transects..... 124

Figure B.5 Time series of (a) air temperature and (b) wind speed collected at a meteorological station on the north side of Kangilliup Sermia's terminus (Fig. 1a) and used as input to the iceberg melt model. Weather stations were recovered just before the observed ice mélange event, and we therefore use the average air temperature and wind speed during the final 5 days of the data record. 124

Figure B.6 Time series of ocean temperature taken at the depth of each instrument (legend) on a subsurface mooring located outside of the sills of Kangilliup Sermia and Kangerlussuup Sermia (Fig. 1a), with the timing of hydrographic observations that bound the investigated ephemeral ice mélange event indicated by the red shaded box. The thick lines indicate a 1-day moving average of ocean temperature taken at 15-minute intervals (thin lines). Hydrographic moorings were recovered, serviced, and redeployed between July 25 and August 11, leading to a gap in the hydrographic record and a slight change in deployment depths indicated in the figure legend. 125

Figure B.7 Time series of subglacial discharge with grey shading indicating sensitivity of the model to high and low melt scenarios from Carroll et al. (2016). The red shaded box indicates the timing of hydrographic observations that bound the investigated ephemeral ice mélange event. 125

Figure B.8 Sensitivity of the height of neutral buoyancy calculation from buoyant plume theory to subglacial discharge magnitude (a) and prescribed line plume width (b). Dashed line indicates the parameters discussed in the main text. 126

Figure B.9 (a) Riverine freshwater outlets (dots) entering the proglacial fjord of Kangilliup Sermia from Mankoff et al. (2020b), with bounding box used to isolate near-glacier freshwater outlets (red dots) for runoff calculation indicated by the red line. (b) Total freshwater discharge into the proglacial fjord from near-glacier outlets in 2014 derived by adding together the discharge from all near-glacier riverine outlets highlighted in (a) by red dots..... 126

Figure C.1 Time series of ice mélange presence/absence data with the GEEDiT-derived optical time series shown as grey shading, with grey indicating seasonal ice mélange is present, and ice mélange rigidity shown as black dots. 128

Figure C.2 Daily time series of fjord-average air temperature derived from ERA5 colored by year and climatology from the entire time series (black lines are average ± 1 standard deviation) All measurements were smoothed with a 30-day moving mean to highlight monthly trends. 129

Figure C.3 Daily time series of subglacial discharge derived from Mankoff and others (2022; black lines) colored by year and climatology from the entire time series (black lines are average ± 1 standard deviation). All measurements were smoothed with a 30-day moving mean to highlight monthly trends. 129

Figure C.4 Profile of the depth of the grounding line at the location of the terminus in 2017 as derived from BedMachine v5. Distance increases from south to north. 130

Figure C.5 Profile of the fjord bathymetry along the deepest point in the fjord between the 2017 terminus and the entrance to the fjord as derived from BedMachine v5. Distance increases away from the glacier terminus. 130

Figure C.6 Profiles of ocean temperature with depth for all fjords with available CTD Data from OMG and field data measurements. The dashed lines represent the grounding line depth (blue) and effective depth (i.e., sill depth if one is located between the cast and the grounding line (black). The original data is shown in black solid lines, whereas the extrapolated data used as input to the subglacial plume model is shown in red solid lines. 131

Figure C.7 Plume neutral buoyancy depth (Znb) derived from each CTD cast input into the subglacial plume model for all tested values of subglacial discharge with the legend showing the OMG CTD Cast ID Number and date. Casts that were derived from field data show an ID Number of #0. 132

Figure C.8 Yearly averaged OMG CTD profiles with depth of the salinity (left) and temperature (right) of the water present in Uummannaq Trough. 133

Figure C.9 Time series of plume neutral buoyancy depth (black lines with red shading for +/- 1 standard deviation) for all study fjords overlaid on seasonal ice mélange presence/absence data (grey shading, with grey indicating seasonal ice mélange is present) and the average iceberg keel depth within the ice mélange (blue shading) for the entire study period (left) and two annual subsections (middle and right). 134

LIST OF TABLES

Table Page

Table 4.1. Summary of environmental, geometric, and dynamic forcings presented in manuscript. The grounding line depth is taken at the location of the 2017 glacier terminus. Values for ice flux and subglacial discharge are the JJA average, while air temperature is the DJF average. Plume neutral buoyancy presented here is for the JJA average value of subglacial discharge. 114
Table B.1. Summary statistics of temperature and salinity from 5-200 m depth both before and after an ephemeral ice mélange event in front of Kangilliup Sermia. Statistics for the full water column are shown in parentheses. 127

CHAPTER I
INTRODUCTION

Ice loss from glaciers and ice sheets worldwide has accelerated in recent decades, largely attributed to a decrease in surface mass balance and an increase in ice discharge to the ocean (King et al., 2020; Smith et al., 2020; Van Den Broeke et al., 2016). One primary driver of this phenomenon is processes occurring at ice-ocean boundaries, such as the frontal ablation of tidewater glaciers, or the combination of iceberg calving and submarine melting at glacier termini (Benn, Cowton, et al., 2017). In particular, recent work has found that one-third to one-half of the ice lost annually from the Greenland Ice Sheet is due to this combination of iceberg calving and submarine melting (Enderlin et al., 2014; Greene et al., 2024; Kochtitzky et al., 2022, 2023), with similar proportions being reported in Alaska (20%; McNabb & Hock, 2015) and Patagonia (34%; Minowa et al., 2021), and much larger proportions in Antarctica (~100%; Depoorter et al., 2013). Despite the suggested importance of frontal ablation on tidewater glacier evolution, the processes that govern it remain largely unconstrained due to difficulties safely obtaining measurements at glacier termini in ice-choked fjords.

Current models of ocean-driven frontal ablation at the ice-ocean interface rely on parameterizations that were developed to describe the submarine melting of near-horizontal ice shelves in Antarctica (Holland & Jenkins, 1999) and remain largely untested at the vertical face of tidewater glacier termini. These parameterizations assume that heat and salt transport at the ice-ocean interface scale with the velocity of the glacier-adjacent water, which would result in submarine melt rates that are highest where the subglacial discharge plume exits at the base of the glacier and ~2 orders of magnitude less away from subglacial discharge outlets (Carroll et al., 2016; Cowton et al., 2015; Jackson et al., 2020; Jenkins, 1999; Slater et al., 2015). These results

have led to the current understanding that the underwater shape of most tidewater glacier termini is either vertical or undercut due to preferential melting near the base of these glaciers where the subglacial discharge plume originates (Fried et al., 2015, 2019; Kimura et al., 2014; Ma & Bassis, 2019; Rignot et al., 2015; Slater, Nienow, Goldberg, et al., 2017; Slater et al., 2021; Wood et al., 2018, 2021). Data to validate this understanding, however, has remained elusive (Abib et al., 2023). Understanding the processes that control the evolution of a glacier's submarine terminus has important implications for feedbacks with both near-terminus glacier dynamics (Benn, Aström, et al., 2017; Catania et al., 2018; Podrasky et al., 2014) and fjord circulation (Jenkins, 2011; Slater, Nienow, Sole, et al., 2017).

Ocean-driven frontal ablation is primarily driven by 1) the thermodynamic processes involved in the direct melting of ice at the glacier terminus discussed above (Jenkins, 2011), and 2) large scale fjord circulation that transfers heat from the global ocean to the glacier terminus (Straneo & Heimbach, 2013). While substantial progress has been made in understanding how variations in factors such as fjord bathymetry and the dynamics of subglacial discharge plumes can alter exchange between glacial fjords and ambient ocean waters (Carroll et al., 2015; Mortensen et al., 2011; Slater et al., 2016, 2020; Xu et al., 2013), there remain many underconstrained components of water column modification in the glacial fjord system. For example, feedbacks between upper layer freshwater inputs, such as iceberg meltwater, and fjord stratification remain largely untested by observations (Abib et al., 2024). Numerical modeling results, however, point to the disproportionate impact that the input of buoyancy from iceberg melting can have on mixing the water column and enhancing exchange between the fjord and shelf waters (Davison et al., 2020, 2022; Hager et al., 2024). Processes that modify the water column between a fjord's sill and the glacier terminus can impact the heat available for

submarine melting and frontal ablation, the resulting shape of the submarine terminus, the upwelling of the subglacial discharge plume, and the long-term evolution of the glacier terminus.

In this dissertation, I investigate the feedbacks between glacier frontal ablation, submarine terminus morphology, and fjord-scale circulation, with the ultimate goal of understanding processes that impact the evolution of tidewater glaciers. In Chapter II, I combine direct measurements of terminus morphology collected by a multibeam sonar with concurrent observations of environmental conditions to investigate the evolution of a tidewater glacier's subsurface ice face across three field campaigns. I show that the terminus morphology is predominately overcut at this tidewater glacier and is accompanied by high multibeam sonar-derived melt rates. In particular, I find that periods of high subglacial discharge lead to localized undercutting at the glacier face, but adjacent to these outlets the glacier terminus maintains significantly overcut geometry, challenging the assumption that tidewater glacier termini are largely undercut during periods of high submarine melting. This chapter was previously published in the Annals of Glaciology and was co-authored with Dr. David Sutherland, Dr. Jason Amundson, Dan Duncan, Dr. Emily Eidam, Dr. Rebecca Jackson, Dr. Christian Kienholz, Dr. Mathieu Morlighem, Dr. Roman Motyka, Dr. Jonathan Nash, Bridget Ovall, and Dr. Erin Pettit.

In Chapter III, I move from the glacier terminus to the proglacial fjord to investigate the role that meltwater released from ice mélange – a combination of sea ice, brash ice, and icebergs – plays on stratification of the water column and its implications for submarine melting of the glacier terminus. In particular, I use direct observations of water column hydrography collected before and after the melt, breakup, and down-fjord transport of an ephemeral ice mélange to investigate the extent to which ice mélange meltwater can modify glacier-adjacent water properties. I find that even a short-lived ice mélange can cause substantial cooling and freshening

of the water column that leads to changes in fjord stratification down to the depth of the outflowing discharge plume. Finally, I compare these observations to those of an adjacent fjord where ice mélange seldom forms to show that the presence or absence of ice mélange melt creates fundamental differences in their upper layer hydrography that need to be accounted for in ocean circulation models to ensure accurate predictions of tidewater glacier evolution. This work is currently under review in The Cryosphere with contributions from co-authors Dr. David Sutherland, Rachel Peterson, Dr. Ginny Catania, Dr. Jonathan Nash, Dr. Emily Shroyer, Dr. Leigh Stearns, and Dr. Timothy Bartholomaus.

Chapter IV builds directly from Chapter III and investigates the conditions that lead to ice mélange formation and dissolution and the corresponding implications for interannual glacier evolution. In this chapter, I use a remote sensing approach to characterize ice mélange in a varied suite of glacial fjords in Central West Greenland. I find that for tidewater glaciers with deep grounding lines, which are currently exhibiting the largest magnitude of terminus retreat in Greenland, the timing of seasonal ice mélange breakup is controlled by the evolution of the subglacial discharge plume in the proglacial fjord. I use a case study from a large outlet glacier to show how interannual changes in the magnitude of subglacial discharge and ambient ocean temperature combine to extend the duration of seasonal ice mélange in this fjord. I discuss the implications that future climate-induced changes to environmental forcings in the region will have on the length of the ice mélange season and what this means for near-terminus tidewater glacier dynamics and the underlying ocean. This chapter will be submitted to the Journal of Glaciology with Dr. David Sutherland, Dr. Jason Amundson, Dr. Michalea King, and Dr. Ian Joughin as co-authors.

CHAPTER II

PERSISTENT OVERCUT REGIONS DOMINATE THE TERMINUS MORPHOLOGY OF A RAPIDLY MELTING TIDEWATER GLACIER

This chapter was previously published as:

Abib, N., Sutherland, D. A., Amundson, J. M., Duncan, D., Eidam, E. F., Jackson, R. H., Kienholz, C., Morlighem, M., Motyka, R. J., Nash, J. D., Ovall, B., and Pettit, E. C. (2023). Persistent overcut regions dominate the terminus morphology of a rapidly melting tidewater glacier. Annals of Glaciology 1–12. https://doi.org/10.1017/aog.2023.38

Author Contributions: Nicole Abib and David A. Sutherland conceived the study. Nicole Abib conducted the analysis and wrote the original manuscript. Jason M. Amundson and Christian Kienholz collected and processed the photogrammetry from the drone imagery. David A. Sutherland, Jason M. Amundson, Emily F. Eidam, Rebecca H. Jackson, Matthieu M. Morlighem, Bridget Oval, and Erin C. Pettit supported the interpretation of the results and contributed to preparation of the manuscript. David A. Sutherland, Jason M. Amundson, Dan Duncan, Emily F. Eidam, Rebecca H. Jackson, Jonathan D. Nash, and Erin C. Pettit developed the original ideas to conduct fieldwork and obtained the field observations presented here.

2.1 Introduction

Ice loss from tidewater glaciers worldwide has accelerated in recent decades (e.g., Mouginot and others, 2019) due to a decrease in surface mass balance and an increase in ice discharge to the ocean (e.g., Enderlin and others, 2014; Van Den Broeke and others, 2016). A

primary driver of increased mass loss into the ocean has been oceanic warming, through its influence on glacier frontal ablation, which is the combination of iceberg calving and submarine melting (Motyka and others, 2003; Holland and others, 2008; Howat and others, 2008; Straneo and others, 2013; Wood and others, 2018; Kochtitzky and others, 2022). Frontal ablation changes the geometry of a glacier's terminus, and can influence glacier dynamics by reduced resistance to glacier flow (Podrasky and others, 2014) through detachment from pinning points in the fjord (Benn and others, 2007) and retreat from a stable grounding line (Catania and others, 2018). Changes in terminus geometry can also impact the upwelling of subglacial discharge plumes (Jenkins, 2011; Slater and others, 2017), thereby altering near-glacier ocean currents that affect submarine melt rates and creating a complex feedback loop between glacier change and ocean circulation. While the feedbacks between ocean properties and glacier change have been recognized as important, process-based understanding of this relationship is still underdeveloped, largely due to the lack of observational data close to tidewater glacier termini.

The timing and magnitude of changes in tidewater glacier geometry are controlled by two processes: iceberg calving and submarine melting. Iceberg calving events occur due to brittle failure of ice, causing rapid and jagged changes in shape (Benn and others, 2007; Fried and others, 2019). On the other hand, submarine melting is thought to depend on the velocity and temperature of the ocean near the ice-ocean interface, resulting in more gradual changes to glacier terminus geometry (Holland and Jenkins, 1999; Jenkins, 1999; Fried and others, 2019). Based on the assumption that submarine melt scales with water velocity adjacent to the ice, melt rates near the location of upwelling subglacial discharge plumes are thought to be higher than those away from discharge outlets (Slater and others, 2015; Cowton and others, 2015; Carroll and others, 2016). Recent work, however, has shown that submarine melt rates can be up to two

orders of magnitude higher than those predicted by plume-melt theory (Sutherland and others, 2019; Jackson and others, 2020, 2022), which describes the coupling of buoyant plume theory with a 3-equation melt parameterization (Holland and Jenkins, 1999; Jenkins 2011; Cowton and others, 2015), particularly away from the direct influence of discharge plumes.

Although often considered separately, submarine melting can influence iceberg calving through changes to the geometry of the submarine terminus. Several studies have suggested that submarine melting alters the stress state in the near terminus region, exerting a first-order control on the calving regime of tidewater glaciers (e.g., O'Leary and Christoffersen, 2013; Benn and others, 2017; Cowton and others, 2019; Ma and Bassis, 2019; Slater and others, 2021). When iceberg calving rates are larger than they would be in the absence of submarine melting, this is referred to as a "calving multiplier" (O'Leary and Christoffersen, 2013; How and others, 2019; Ma and Bassis, 2019). In glacier evolution models, iceberg calving events are typically parameterized based on ice thickness, grounding line depth, ice stresses, and glacier velocities (Amaral and others, 2020). The dearth of temporally evolving 3D terminus geometries has made validation of these models difficult (Ma and Bassis, 2019); therefore, prior investigations into "calving multipliers" have relied on idealized submarine terminus morphologies, typically either undercut or assuming a vertical calving face. A growing body of evidence suggests the presence of various overcut morphologies, including underwater ice ramps (Hunter and Powell, 1998; Motyka and others, 1998; Rignot and others, 2015; Wagner and others, 2016; Wagner and others, 2019; Mercenier and others, 2019, 2020), terraces (Sugiyama and others, 2019), or grounding line toes (Fried and others, 2019), for which the influence on near terminus stresses is largely uninvestigated. Understanding the 3D geometry and evolution of the subsurface terminus

is therefore essential for predicting feedbacks between ocean-driven melting and near terminus glacier dynamics.

Directly observing time-varying terminus geometry is challenging due to hazardous field conditions near the front of tidewater glaciers. A handful of studies have used multibeam sonar in Alaska (Sutherland and others, 2019) and Greenland (Fried and others, 2015, 2019; Rignot and others, 2015; Wagner and others, 2019) to map the terminus beneath the waterline in three-dimensional space. These surveys show heterogeneous morphology across the width of the terminus, with evidence of large undercut regions present at the location of subglacial discharge plumes and more vertical terminus slopes away from these discharge outlets (Fried and others, 2015, 2019; Rignot and others, 2015). Such variations in terminus morphology are unlikely to be driven by glacier flow, which is often dominated by sliding near the terminus and typically assumed to be nearly spatially uniform from the bed to the surface. This suggests that these varying morphologies result from different frontal ablation processes across the width and depth of a glacier's terminus: melting by deep, warm water drawn in by subglacial discharge at depth (Rignot and others, 2015; Fried and others, 2019) can produce undercutting, calving in the upper water column (Fried and others, 2019) would produce overcutting, and ocean-driven ambient melting away from the discharge plume (Sutherland and others, 2019, Wagner and others, 2019) may create differing local geometries. Each of these surveys, however, is limited to one point in time, preventing us from investigating the evolution of the submarine terminus and understanding the relationship between local environmental forcings, terminus geometry, and glacier dynamics.

Here we use a novel dataset from LeConte Glacier (Xeitl Sít' in Tlingit), Alaska, to investigate the temporal evolution of the subsurface terminus and relate it to the spatial patterns

and drivers of frontal ablation. We combine high-resolution maps of the glacier's submarine terminus from repeat multibeam sonar imaging with concurrent observations of subaerial geometry derived from terrestrial radar interferometry and time-lapse imagery collected during three field campaigns between 2016 – 2018. Our results provide the first concurrent observations of time-varying three-dimensional terminus geometry and environmental forcings, allowing us to investigate the evolution of the submarine terminus across a wide parameter space of environmental conditions.

2.1.1 Physical setting

LeConte Glacier is a fast-flowing (15-25 m d^{-1}) tidewater glacier that terminates in LeConte Bay (Xeitl Geeyi' in Tlingit), ~30 km from Petersburg in Southeast Alaska (Fig. 1a; O'Neel and others, 2001). With a terminus width of ~1 km and a maximum grounding line depth of 200 m (Sutherland and others, 2019), the dimensions of LeConte Glacier make it a relatively accessible analog for smaller outlet glaciers around the periphery of the Greenland Ice Sheet. In addition, the springtime oceanic temperature and water column stratification at LeConte Glacier are similar to typical conditions observed in Greenlandic proglacial fjords (Jackson and others, 2022). Throughout the year, the glacial system is exposed to a range of ocean temperatures (4 – 7 °C at depth; Hager and others, 2022) and subglacial discharge (20 – 350 m^3 s^{-1}; Amundson and others, 2020), with outflowing plumes (Motyka and others, 2003) and a recirculation gyre (Kienholz and others, 2019) typically visible in the near-terminus surface waters. Several prior studies at LeConte Glacier using a combination of ocean observations both further from (~1.5 km away; Motyka and others 2003, 2013; Jackson and others, 2022) and near the glacier terminus (~ 350 m away; Jackson and others, 2020), as well as multibeam sonar (Sutherland and

others, 2019), found very high rates of ocean-driven melting at the glacier (up to 15 m d^{-1}), accounting for up to 50% of the total ice flux to the terminus in the summer months. Additional near-terminus autonomous kayak surveys revealed the ubiquitous presence of ambient meltwater intrusions into the proglacial fjord, suggesting elevated rates of submarine melting even several hundred meters from the upwelling subglacial discharge plume (Jackson and others, 2020).

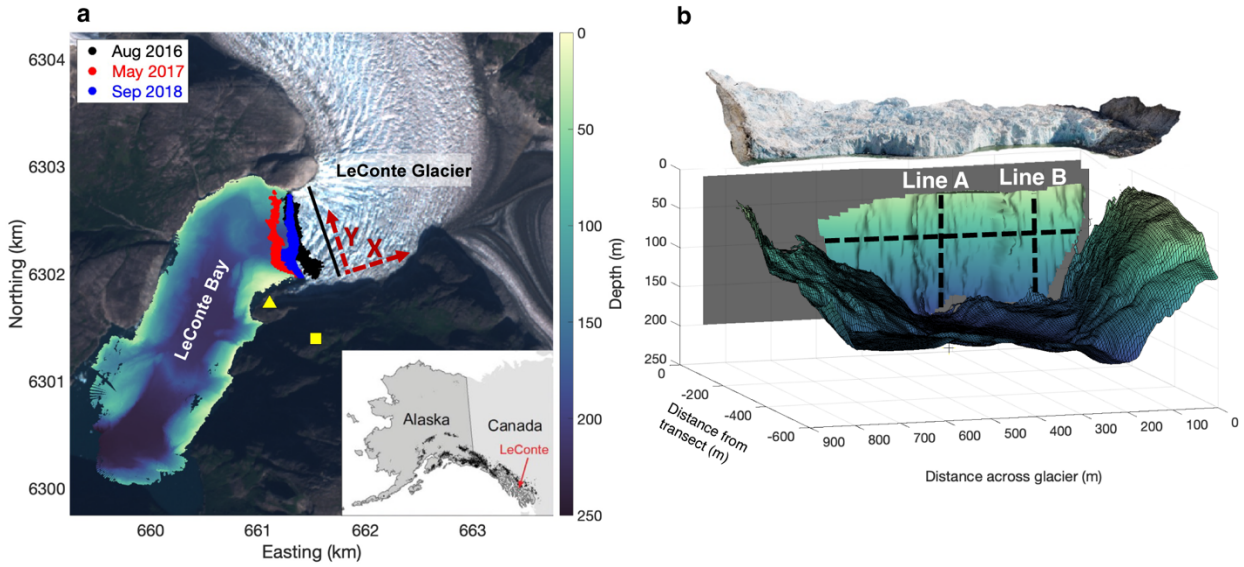

Figure 2.1. Study area. (a) Sentinel 2-A image of LeConte Glacier and Bay in September 2018 with markers indicating the location of the terrestrial radar interferometer and the upper time-lapse cameras (yellow square), the lower time-lapse cameras (yellow triangle), as well as the collected multibeam point clouds (Black: August 2016, Red: May 2017, Blue: September 2018). An example reference transect (black line) and rotated coordinate system (red dashed lines) is shown overtop the glacier. Map is referenced to UTM Zone 8N and inset shows location of LeConte Glacier in southeast Alaska. (b) Example output from multibeam sonar showing the subaerial and submarine terminus geometry, gridded bathymetry, and reference plane used for projection and gridding of the point clouds (grey rectangle). Image of the subaerial terminus was acquired from UAV imagery and manually lined up with the submarine terminus. Dashed lines correspond with the transects taken for panels a, b, and c in Fig. 2, and all vertical transects are shown in a Supplementary Video.

2.2 Methods

2.2.1 Submarine glacier morphology

We surveyed the glacier terminus and proglacial bathymetry using a Reson SeaBat 7111 multibeam echosounder and Applanix POS/MV 320 Wave Master in August 2016 and a Reson

SeaBat T50-P multibeam system in May 2017 and September 2018 to investigate the three-dimensional geometry and evolution of the submarine terminus (Fig. 1b). We inserted a 15-degree wedge into the multibeam system to enable scanning of the grounding line and the submarine ice face at a distance of ~300 m from the terminus following the methods of Sutherland and others (2019). This side-scanning multibeam sonar produces a 3-dimensional point cloud from the fjord floor to ~20 m below the fjord's surface. We determined the grounding line by using a break in the slope of the point cloud (Sutherland and others, 2019; Eidam and others, 2020). Scans of the terminus collected within one hour of each other were combined so that each scan then represented a single trip to the ice face and covered as much of the submarine terminus as possible. This resulted in 6 near-complete terminus scans between August 9-15, 2016, 5 scans between May 10-12, 2017, and 13 scans between September 13-18, 2018. To assess the error of these point clouds, we compared the data over two patches of bedrock (~15,000–17,000 m^2) near the terminus, finding maximum errors of 5.3 m in August 2016, 2.6 m in May 2017, and 2.4 m in September 2018 (Sutherland and others, 2019; Eidam and others, 2020).

Next, we defined a 2-dimensional reference plane up-glacier from the terminus and perpendicular to ice flow onto which we projected and gridded the point clouds at resolutions of 5-20 m to account for uncertainty in our projection of a 3-dimensional point cloud onto a 2-dimensional plane (Fig. 1b; Sutherland and others, 2019). For the gridded scans, we calculated the vertical and horizontal slope of the terminus for each grid cell. These slopes were then smoothed with a box filter (3x3 grid cells) for each scan to remove high-frequency noise.

2.2.2 Subaerial glacier morphology

To quantify the rate of change of the glacier's subaerial terminus, we used a terrestrial radar interferometer (TRI) in August 2016 and May 2017 and time-lapse imagery in September 2018. The instruments were all deployed on a ridge to the south of the terminus throughout each field campaign (August 2016 and May 2017: 415 m above sea level, 56.8286° N, 132.3418° W; September 2018: 63 m above sea level, 56.8314° N, 132.3595° W; Fig. 1a).

2.2.2.1 Terrestrial radar interferometry

We used a Gamma Remote-Sensing TRI to measure both the glacier velocity and terminus position in August 2016 and May 2017. The TRI is a Ku-band (λ = 1.74 cm) real aperture imaging radar with a maximum range of 16 km and an azimuth resolution of ~3 m in the near field (0.4 km) and ~21 m in the far field (3 km). The TRI conducted scans at ~3-minute intervals over a radar swath of 120 degrees. To enable terminus delineation, the radar backscatter images were projected into Cartesian space, georectified to UTM Zone 8N, and then gridded at 5 m (Sutherland and others, 2019). The terminus position was then manually digitized on the georectified radar backscatter images with a time separation of 2 hours. To reduce location uncertainty in the terminus position, this delineation process was repeated twice. All processing of TRI data was done with Gamma proprietary software and an associated Python module (https://bitbucket.org/luethim/gpritools).

2.2.2.2 Time-Lapse imagery

In September 2018 we used time-lapse imagery from a camera (18 mm Canon Rebel housed within a Harbortronics Time-Lapse package) with a 30-second photo interval deployed

on a ridge to the south of the glacier's terminus to observe the evolution of the terminus at the waterline. The waterline position was outlined in ArcGIS for photos taken every 30 minutes and projected into map coordinates (UTM Zone 8N) using a camera model (Kienholz and others, 2019). The root-mean-square error was calculated between the delineated waterline positions and closest drone-derived terminus position in time, finding uncertainty of 3 ± 2 m in the time-lapse image derived waterlines.

2.2.3 Ice velocity

Glacier velocities were derived from a terrestrial radar interferometer in August 2016 and May 2017 and drone imagery in September 2018. The average ice velocity from each field campaign was extracted along the corresponding transect used for the multibeam point cloud projection and gridding (Fig. 1b; Fig. S1). To account for differences in ice velocity between the reference transect and the terminus due to strain of the ice, we additionally extract a transect of ice velocity as close to the terminus as possible and include this difference in our melt rate uncertainty estimates.

2.2.3.1 Terrestrial radar interferometry

The ice flow direction near the terminus was nearly perpendicular to the radar line-of-sight, precluding us from using interferometry to calculate near-terminus ice velocities. We instead gridded the georectified radar backscatter images at 10 m resolution and then applied normalized cross-correlation from the Python openPIV module (Bouguet, 2000) with a correlation window size of 16 x 16 pixels (160 x 160 m) and 50% overlap to calculate ice speed

(as described in Sutherland and others, 2019). The resulting velocity fields were then stacked and averaged for each field campaign.

2.2.3.2 Drone imagery

To obtain glacier velocities in September 2018, we flew 12 campaigns with a DJI Phantom IV Pro Quadcopter over the lower 130 m of the glacier. We created digital elevation models (DEMs) over the lower glacier for each campaign using Structure from Motion photogrammetric processing in Agisoft PhotoScan (as described in Jackson and others, 2022), with ground control points on both sides of the terminus. Glacier velocity fields were generated using feature tracking in openPIV (Bouguet, 2000) of shaded relief DEMs separated by ~24 hours.

2.2.4 Glacier change in time

To investigate the impact of environmental forcings on glacier geometry, we calculated frontal ablation (F_A) of both the subaerial terminus, using the TRI and time-lapse imagery, and the submarine terminus using the multibeam sonar data (Eqn. 2.1). We differenced all multibeam point clouds within a field season that had a time separation of more than 0.5 days (equivalent to 5-10 m of ice advection) to obtain the rate of change in terminus position ($\frac{dL}{dt}$). We then subtracted the terminus position change ($\frac{dL}{dt}$) from the ice velocities (U_{ice}) derived from the TRI in August 2016 and May 2017 and the drone imagery in September 2018 to give us a rate of frontal ablation (F_A), where

$$F_A(y,z,t) = U_{ice}(y,t) - \frac{dL\,(y,z,t)}{dt} = C(y,z,t) + \dot{m}(y,z,t) \quad (2.1)$$

Frontal ablation was then separated into its two components, iceberg calving (C) and submarine melting ($\dot{m}$). Our calculation of submarine melt rate follows the methodology from Sutherland and others (2019), with a slightly modified approach to account for iceberg calving events that extend beneath the waterline. When calculating melt rates from multibeam sonar at LeConte Glacier in August 2016 and May 2017, Sutherland and others (2019) excluded regions of the submarine terminus where subaerial iceberg calving events were recorded with the TRI between multibeam scans. This can potentially exclude submarine melt rates from portions of the submarine terminus where subaerial calving events did not extend beneath the waterline.

Instead, here we assume that the evolution of the subaerial terminus is largely dominated by iceberg calving events in order to determine a characteristic calving rate for each field campaign by differencing successive terminus positions. Then, to remove the signal of iceberg calving from frontal ablation of the submarine terminus, we exclude grid cells where the frontal ablation rate exceeds our characteristic calving rate (10 m d^{-1} in May 2017 and September 2018, 20 m d^{-1} in August 2016; Fig. S2) to calculate a melt rate for each multibeam pair comparison. This has the effect of giving conservatively low estimated melt rates and allows us to evaluate melt rates across a broader range of the terminus than in Sutherland and others (2019). Using the vertical and horizontal slopes of the ice face, we converted these to an ice-perpendicular melt rate. Finally, all the multibeam pair comparisons were averaged to obtain a mean melt rate for each grid cell across the terminus for each field campaign.

2.2.5 Environmental forcing

2.2.5.1 Fjord water properties

We used near-terminus hydrography during each field campaign to quantify ambient ocean conditions. In August 2016 and May 2017, we collected conductivity-temperature-depth (CTD) profiles from a small vessel ~1.5 km from the glacier terminus (Sutherland and others, 2019; Jackson and others, 2022). In September 2018, our shipboard CTD observations were complemented by CTD casts collected from an autonomous kayak within 400 m of the glacier terminus (Jackson and others, 2020). To capture the ambient ocean conditions flowing towards the glacier terminus, we only look at the profiles of temperature and salinity below the approximate depth of the thermocline in the fjord (from 75 m to the grounding line depth; Fig. S3).

2.2.5.2 Subglacial discharge

Subglacial discharge was estimated using a Distributed Enhanced Temperature Index Model (Hock, 1999) coupled to an accumulation model and linear reservoir-based discharge routing model (Hock and Noetzli, 1997) as described in Amundson and others (2020). Inputs for this model include local meteorologic conditions recorded with a Campbell Scientific Weather Station located near the TRI and time-lapse cameras. These data were successfully correlated with observations from the nearby (~30 km) Petersburg Airport, which allowed for the creation of a continuous time series of precipitation and temperature throughout our observation period (Sutherland and others, 2019; Fig. S4).

To identify the location across glacier where the subglacial discharge plume would likely originate, we calculated the hydraulic pressure potential (P; Eqn. 2.2) and head (H; Eqn. 2.3) (Shreve, 1972):

$$P = \rho_i g(Z_I - Z_B) + \rho_w g Z_B \tag{2.2}$$

$$H = \frac{P}{\rho_w g} \tag{2.3}$$

where ρ_i and ρ_w are the densities of ice (917 kg m^{-3}) and fresh water (1000 kg m^{-3}), Z_I and Z_B are the elevations of the ice surface and bed relative to mean sea level, and g is the acceleration due to gravity. The ice surface elevation is from a WorldView-2 Digital Elevation Model from September 21, 2018. The bed topography was generated using a mass-conservation approach (Morlighem and others, 2011) and validated with a seismic transect collected 7 km from the glacier's terminus (Truffer and Motyka, pers. comm.). Both the ice and bed data sources are gridded to the same resolution (30 m) and smoothed using a 5x5 cell low-pass filter to remove the influence of surface crevasses.

We then used the ArcGIS hydrology toolset to calculate the expected flow direction and upstream contribution of each grid cell to determine the likely flow paths of subglacial streams. This output was projected into the same coordinate system as the gridded multibeam sonar data for comparison. Finally, the location of potential subglacial discharge outlets was taken to be where the highest upstream contribution values intersected with the location of the grounding line for all three field campaigns.

2.3 Results

2.3.1 Glacier morphology and change in time

In each field campaign, we observe terminus morphology that is distinctly three-dimensional and varies spatially across the subsurface terminus (see Supplemental Video). In August 2016, the submarine terminus is 150 m more advanced on the northern side (Fig. 2a – Line A) than on the southern side (Fig. 2a – Line B). The opposite is true in May 2017 and September 2018, where the submarine terminus protrudes 70 m and 90 m further into the fjord on the southern side of the terminus. In addition to these large-scale variations in terminus shape, there are smaller variations in the shape of the submarine ice face across the glacier. Although the resolution of our multibeam point clouds increases from 2016 to 2018, Fig. 2a indicates that across-glacier variations in shape appear on larger spatial scales in August 2016 than in either May 2017 or September 2018. For example, in September 2018, the shape of the terminus varies on spatial scales of 100 – 200 m (e.g., at x = 250-450 m across the terminus; Fig. 2a). In August 2016, we do not see these same small-scale undulations in the terminus shape. While our multibeam point clouds can only resolve features larger than ~10 m, there are certainly additional smaller scale features that occur at resolutions finer than our point clouds can resolve (i.e. scallops, dimples, and flutes observed on icebergs; Motyka and others, 2003; Bushuk and others, 2019)

The multibeam point clouds show that, in addition to across-glacier variations in terminus position, the terminus shape also varies with depth. In all three study periods, the shape of the terminus remains nearly vertical on the north side (Line A) of the terminus (Fig. 2b). However, the terminus morphology in August 2016 is characterized by a large undercut region (100 m wide) on the south side (Line B), whereas the terminus in May 2017 and September 2018

exhibits large swaths of overcut morphology (150 m and 100 m wide, respectively) in the same region (Fig. 2c). These overcut regions correspond with the location of a large ice ramp that protrudes 75 m into the fjord in May 2017 and 125 m in September 2018 (Fig. 2c).

Although the general morphology of the terminus remains similar within each field campaign, the multibeam point clouds show that the submarine terminus evolves within our individual field campaigns. The multibeam point clouds show that the terminus evolves gradually over an individual study period, however, we occasionally observe instances of abrupt terminus position change, likely due to iceberg calving events that are either purely submarine or are subaerial calving events that extend beneath the waterline. An example of a subaerial calving event that includes portions of the submarine terminus can be seen on the north side of the terminus in September 2018 between the multibeam scans taken at 4.04 and 4.21 days since the start of the field campaign (Fig. 2b, bottom panel). Between these multibeam scans (taken ~4 hours apart), the terminus retreats 30 m in the upper 75 m of the water column (light blue to dark blue line). In contrast, on the southern side of the terminus, we see the ice face slowly advance over the course of the field campaign in September 2018 (Fig. 2c, bottom panel). This pattern of advance and retreat varies across the terminus within each field campaign, with the northern side of the terminus ending in a more retreated position at the end of the field campaign and the southern side ending in a more advanced position (Fig. 2a). Despite these spatial variations, the general morphology of the terminus (whether undercut, overcut, or vertical) typically remains the same throughout an individual field campaign, with just the position of the terminus varying in time (Fig. 2; Fig. 3).

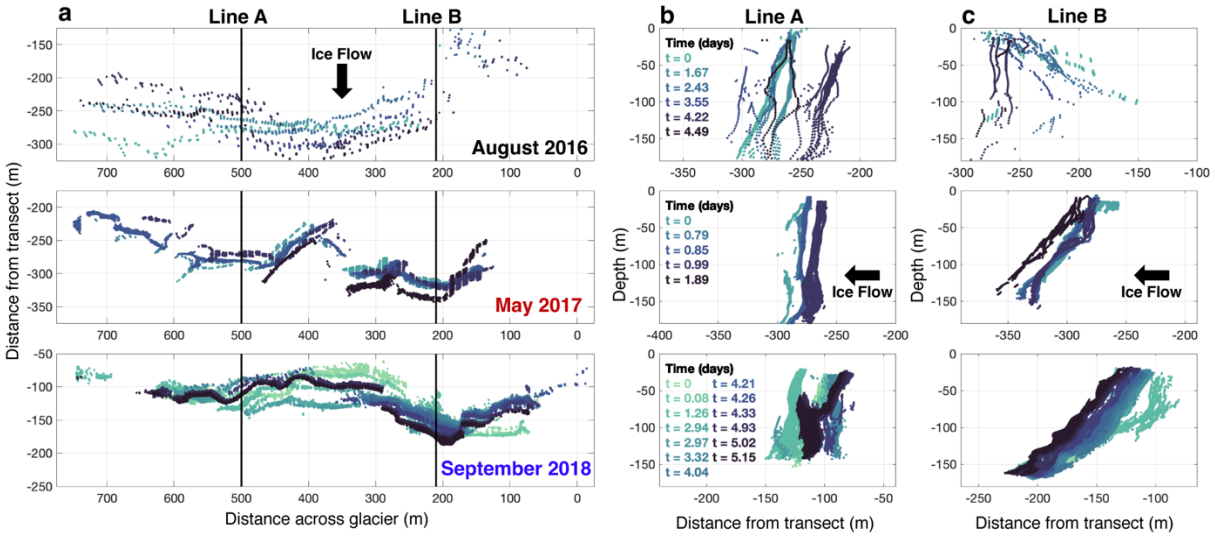

Figure 2.2. Short term changes in terminus morphology for August 2016 (top), May 2017 (middle), and September 2018 (bottom). (a) Across glacier cross-section taken from 100-110 m depth. Each color indicates a different multibeam scan. (b) Vertical cross-section taken at 490-510 m across-glacier (Line A, north side of terminus, Fig. 1b). (c) Vertical cross-section taken at 200-220 m across-glacier (Line B, south side of terminus, Fig. 1b). All vertical cross-sections are shown in a Supplementary Video.

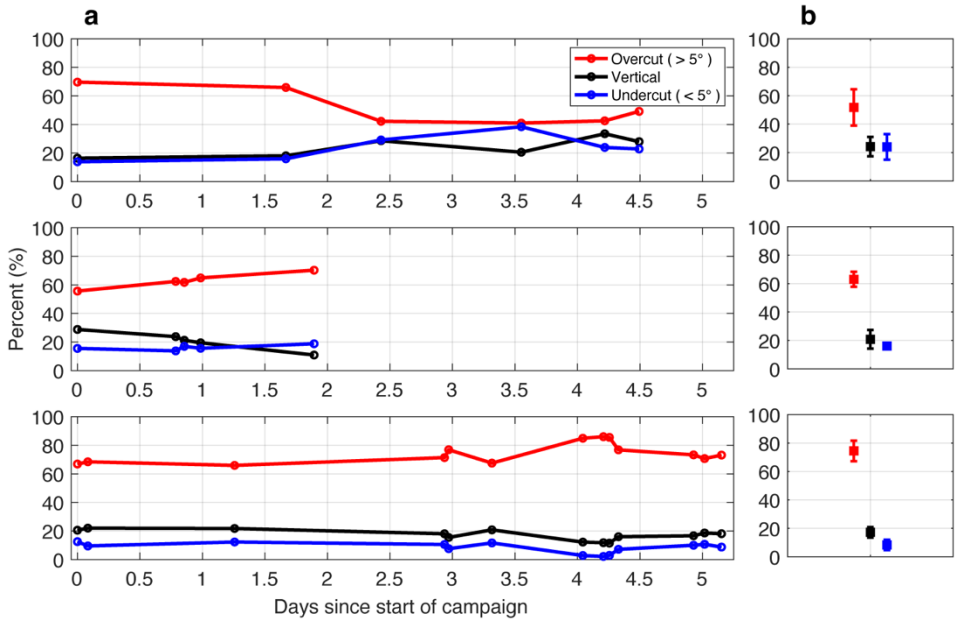

Figure 2.3. (a) Percentage of the terminus that is overcut (red line), vertical (black line), and undercut (blue line) over time in the field campaigns in August 2016 (top), May 2017 (middle), and September 2018 (bottom). Circle markers indicate the time at which multibeam data was collected. (b) The average percent overcut (red), vertical (black), and undercut (blue) over the duration of the field campaign with error bars indicating ± 1 standard deviation.

In all three periods of study, the multibeam scans of the glacier terminus show slopes in the vertical direction that are majority overcut (August 2016: 52 ± 13%, May 2017: 63 ± 5%, and September 2018: 74 ± 7% of all grid cells on average; Fig. 3). In August 2016, the terminus became less overcut over the duration of the field campaign, with the percentage overcut changing from 70% to 49% over the 4.5-day study period (Fig. 3a). In contrast, the terminus in May 2017 and September 2018 became more overcut over the course of their individual study periods, increasing from 56% to 70% over 1.9 days (Fig. 3b) and 67% to 73% over 5.1 days respectively (Fig. 3c).

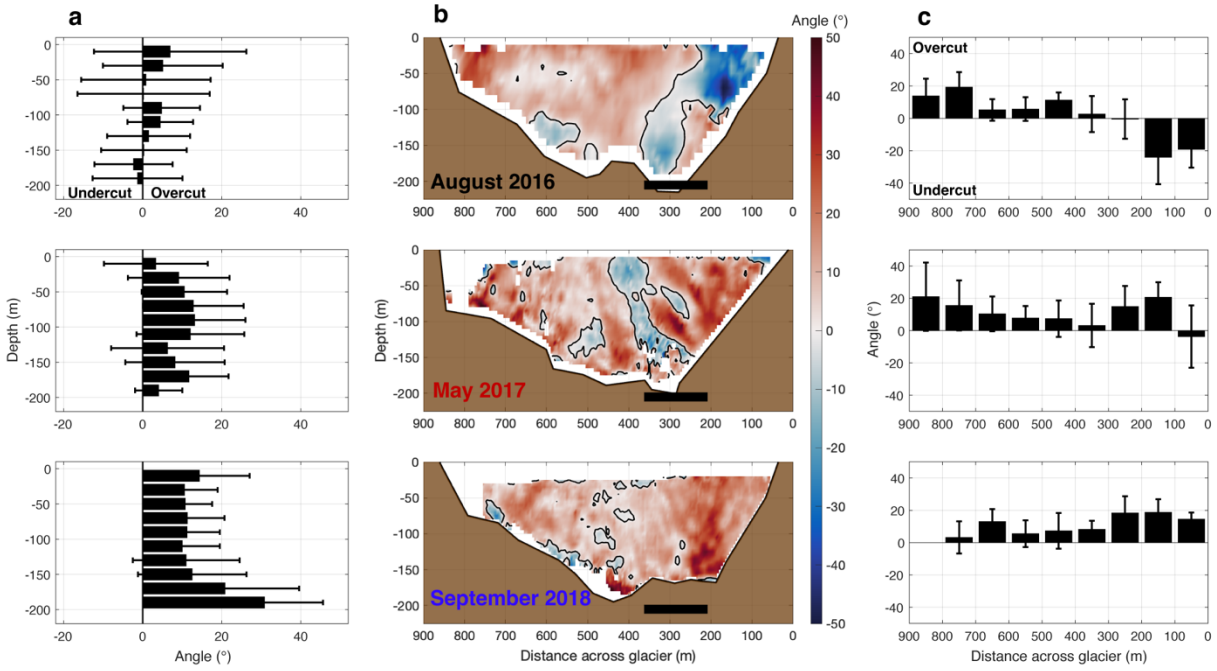

Figure 2.4 Average vertical terminus slope for August 2016 (top), May 2017 (middle), and September 2018 (bottom). (a) Variation in terminus slope with depth, error bars indicate ± 1 standard deviation. (b) Average terminus slope for each grid cell across the entire glacier terminus. (c) Variation in terminus slope across the width of the glacier. The brown shaded region indicates the bed along the grounding line of the glacier, and the black rectangle indicates the location of the likely subglacial discharge outlet, based on hydropotential analysis (Fig. 7). Angles < 0 (blue) are undercut, whereas angles > 0 (red) are overcut regions of the terminus.

In addition to variations in glacier shape, the slope of the glacier terminus varies with depth and across-glacier. In all three field campaigns, the submarine terminus is close to vertical or is overcut above a depth of 70 m when averaged along the glacier front (Fig. 4a). The most significant differences in terminus morphology between each field campaign occur at depths greater than 130 m. In August 2016, we observe undercut regions at depth, with the average slope beneath 130 m depth varying between -2° and 0° from vertical across the glacier's entire width (Fig. 4a). Below this same depth in May 2017 and September 2018, however, the submarine terminus exhibits overcut slopes varying between 6° to 11° and 10° to 30° respectively (Fig. 4a). The slope of the submarine terminus also varies across the width of the glacier (Fig. 4b). In August 2016, the south side of the terminus is severely undercut, with an average slope of -20° and a maximum undercut slope of -40° (Fig. 4c). The north side of the terminus, however, is overcut with an average slope of 15°. In contrast, almost all of the terminus is overcut in May 2017 and September 2018, reaching an average slope on the south side of 20° in May 2017 and September 2018.

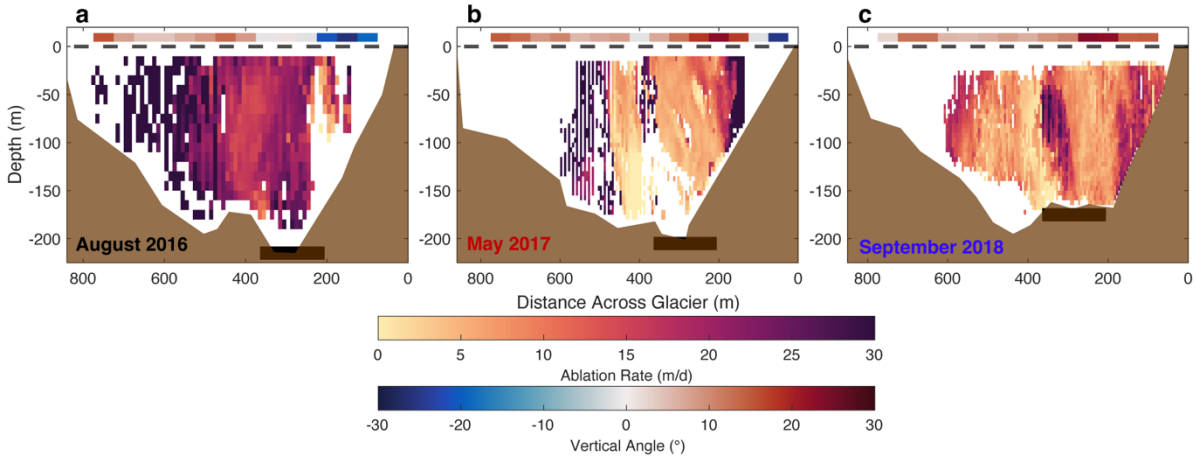

Figure 2.5 Plan view of average frontal ablation rates across the glacier terminus in (a) August 2016, (b) May 2017, and (c) September 2018. The brown shaded region indicates the bed along the grounding line of the glacier, and the black rectangle indicates the location of the likely

subglacial discharge outlet, based on hydropotential analysis (Fig. 7). The average vertical angle is shown in red-blue color scale above the average frontal ablation rates, where angles < 0 (blue) are undercut, whereas angles > 0 (red) are overcut regions of the terminus.

Patterns of glacier frontal ablation (F_A) and submarine melt ($\dot{m}$) correspond with the spatiotemporal variations in glacier morphology described above. In August 2016, maximum values of frontal ablation (>20 m d^{-1}) occur directly above the deep undercut swath on the south side of the terminus (at 250 – 350 m across glacier; Fig. 5a). In May 2017 and September 2018, however, frontal ablation peaks just to the north of the protruding ice ramp (at 300 – 400 m across glacier; Fig. 5b; 5c). In addition to these regions of maximum frontal ablation on the south side of the terminus, the glacier experiences high localized frontal ablation in several other locations across the glacier terminus (i.e., in Fig. 5 at x > 500 m in August 2016, x < 200 m in May 2017, and x < 150 m and x > 550 m across glacier in September 2018).

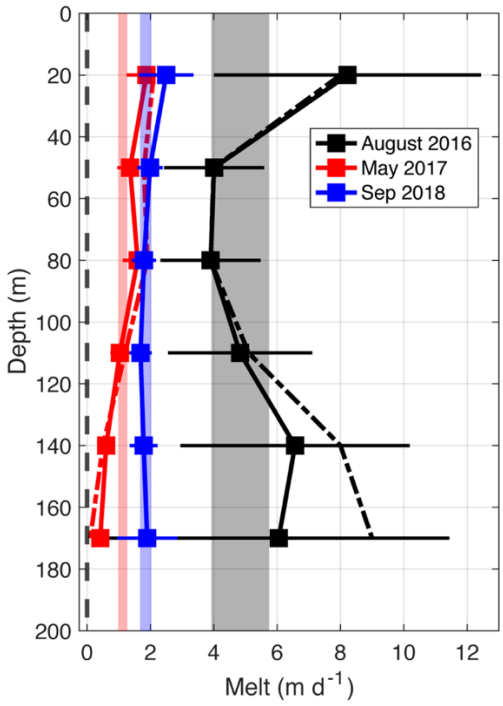

Figure 2.6 Average submarine melt rate with depth. Error bars indicate ± 1 standard deviation. Comparison to Sutherland and others (2019) is shown in dashed lines. The vertical shaded region shows the terminus area average value for each field campaign.

After separating frontal ablation (F_A) into iceberg calving (C) and submarine melting ($\dot{m}$), we find that the terminus in August 2016 experiences average rates of submarine melting that are ~4x those in May 2017 and September 2018 (August 2016: 4.84 ± 0.91 m d^{-1}; May 2017: 1.13 ± 0.14 m d^{-1}; September 2018: 1.85 ± 0.18 m d^{-1}; Fig. 6). In addition, the submarine melt profile with depth shows a different spatial pattern in August 2016 than during the other two field campaigns. In all three field campaigns, the glacier experiences maximum submarine melt rates at the surface of the water column, but the terminus in August 2016 experiences a secondary maximum in submarine melt rates below a depth of 130 m.

2.3.2 Environmental forcings

We observe significantly different environmental conditions within each individual field season (Fig. 7). The ocean temperatures below 75 m depth in the proglacial fjord are similar in August 2016 and September 2018, with an average of 7.4 ± 0.2°C and 7.6 ± 0.2°C respectively (Fig. 7a). The ocean is considerably cooler in May 2017, with an average temperature of 3.9 ± 0.4°C. In contrast, the average ocean salinity is highest in May 2017 (31.1 ± 0.1 g/kg) and lowest in August 2016 (26.8 ± 0.5 g/kg; Fig. S3). A strong halocline is present at ~40 m depth in August 2016 and September 2018 but is observed at the surface in May 2017 (Fig. S3). When viewed in temperature-salinity space, these seasonal differences in temperature and salinity of the ocean show that the stratification in the fjord is most similar in August 2016 and September 2018 when compared to May 2017 (Fig. S3). These three field surveys encompass a large portion of the full yearly range of typical ocean temperatures observed within LeConte Bay as inferred from long term mooring deployments (Hager and others, 2022).

Subglacial discharge is highest in August 2016, with a flux of 208 ± 42 m^3 s^{-1} (Fig. 7b). May 2017 and September 2018 exhibit much lower ranges of subglacial discharge, with fluxes of 51 ± 16 m^3 s^{-1} and 104 ± 33 m^3 s^{-1} respectively. These patterns align with the observed patterns in precipitation and air temperature, with the warmest and wettest conditions occurring in August 2016, and cooler temperatures occurring in both May 2017 and September 2018 (Fig. S4)

The hydropotential analysis suggests that the main subglacial discharge channel travels down the trunk of the glacier, intersecting with the southern side of the glacier's terminus at 210 m to 360 m across glacier (indicated by 1 in Fig. 7c). In addition to this likely pathway of subglacial water, there is a second potential subglacial discharge outlet (though it is substantially less likely, with just 5% of the main channel magnitude) that is present on the northern side of the terminus at about 650 m across its width (indicated by 2 in Fig. 7c). By comparing to near-terminus ocean measurements from September 2018, we see that the highest ocean velocities were flowing away from the terminus between 250-400 m across glacier (Jackson and others, 2020), which is just north of the ice ramp protruding into the fjord.

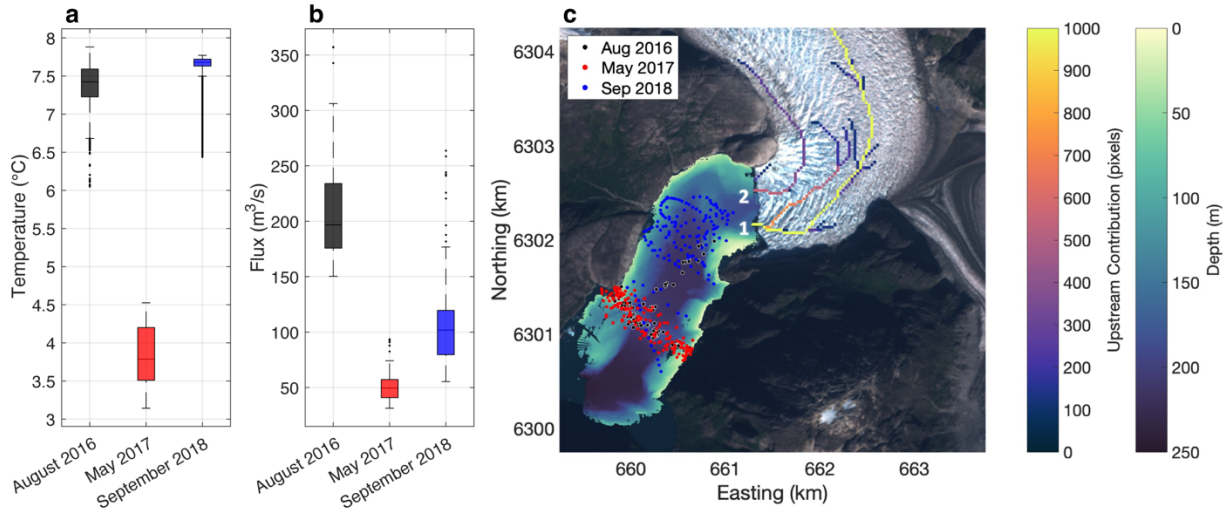

Figure 2.7 Overview of environmental forcings. (a) Summary of ocean temperature beneath 75m depth for August 2016, May 2017, and September 2018. (b) Summary of subglacial discharge

for 2016, 2017, and 2018. (c) Likely subglacial discharge channels as predicted by the hydropotential analysis (red-yellow color scale) and location of CTD casts taken in the proglacial fjord overlaid on top of our study area map. Channels marked by 1 and 2 indicate the discharge outlets with the highest and second highest upstream flow contribution respectively.

2.4 Discussion

By conducting repeat multibeam sonar surveys of the submarine terminus at LeConte Glacier, we show that the glacier terminus is persistently overcut across three seasons and that its morphology does not change drastically within a single study period (i.e., on the timescale of a week). We find that the glacier terminus sustains large overcut geometries, such as a submarine ice ramp, in the vicinity of a subglacial discharge outlet, and discuss below the possible formation mechanisms of this terminus shape. Finally, we compare our multibeam-derived melt rates to previous observations at LeConte Glacier and explore the implications for plume-melt theory when a glacier terminus is overcut.

2.4.1 Persistent overcutting across the glacier terminus

Despite the large seasonal variations in glacier morphology and submarine melt rates observed at LeConte Glacier, the majority of the submarine terminus remains overcut through time. This is particularly notable in August 2016, when 52% of the terminus is overcut even though subglacial discharge is high (208 $m^3 s^{-1}$) compared to the May and September surveys (Fig. 3, Fig. 7). The three field campaigns presented here encompass a wide range of the environmental conditions observed interannually at LeConte Glacier, with average subglacial discharge ranging from 51 to 208 $m^3 s^{-1}$ (annual cycle of ~20-350 $m^3 s^{-1}$; Amundson and others, 2020) and ambient ocean temperatures between 3.9 and 7.6 °C (annual cycle of ~3-8 °C; Hager

and others, 2022). We observe a terminus morphology that is primarily overcut despite these large variations in subglacial discharge and fjord conditions.

These observations of persistent overcutting are contrary to previously published measurements of submarine glacier morphology (Rignot and others, 2015; Fried and others, 2019). Prior observations of terminus morphology come from marine terminating outlet glaciers around the Greenland Ice Sheet, which typically have glacier termini that are much wider (several kilometers) and grounded deeper (100-1000 m) than LeConte Glacier (e.g., Slater and others, 2022). At these larger marine terminating outlet glaciers, multibeam sonar-derived observations of terminus morphology revealed that the termini were largely undercut, especially in the vicinity of subglacial discharge outlets. While only 26-48% of LeConte Glacier's submarine terminus is undercut on average, undercutting was observed across 77% of the terminus at Kangerlussup Sermia (Fried and others, 2019), 76% of the terminus at Kangilernata Sermia (Rignot and others, 2015), 73% of the terminus at Store Gletscher (Rignot and others, 2015), and almost the entirety of the submarine terminus at Rink Isbræ (Rignot and others, 2015).

Due to the prevalence of undercutting previously observed at marine terminating glaciers, models of submarine melting and iceberg calving have primarily used idealized terminus geometries that are either purely undercut or vertical (e.g., Slater and others, 2017; Schulz and others, 2022; Holmes and others, in review). Our results, however, show that despite high melt rates observed across the glacier terminus, LeConte Glacier is largely overcut. On the northern side of the terminus, we see slight overcutting, with an average terminus slope of ~12° in all three field campaigns. The southern side of the terminus is more dramatically overcut, reaching slopes of up to ~30° from vertical (Fig. 4c). While the multibeam scans do show that the shape of

the submarine terminus varies through time, the average morphology of the terminus remains nearly constant within each field campaign (with the percentage overcut varying by 13% in August 2016, 5% in May 2017, and 7% in September 2018; Fig. 3) apart from iceberg calving events that involve the submarine terminus (Fig. 2). This suggests that, on the scale of features that we can observe (> 10 m), the average morphology of the terminus varies much more between seasons than over shorter time scales.

2.4.2 Seasonal overcutting in the vicinity of a subglacial discharge outlet

Previous observations of submarine glacier termini from multibeam sonar have focused on the undercut regions adjacent to subglacial discharge outlets. However, Wagner and others (2019) observed a terminus morphology that was primarily overcut away from the influence of the subglacial discharge plume. At Saqqarliup Glacier, Greenland, the submarine portion of the terminus protruded ~20 m into the proglacial fjord in regions of ambient melting. This is similar to what we observe away from the subglacial discharge plume on the northern side of the terminus at LeConte Glacier (Fig. 2b). The time-varying aspect of our observations, however, show that even in the vicinity of a subglacial discharge outlet, the glacier terminus can support substantial overcut morphology through time, despite high overall melt rates (Fig. 2c).

While the majority of LeConte Glacier's terminus is overcut, there are large variations in terminus morphology between field campaigns in the vicinity of the main predicted subglacial discharge outlet. We find that periods of high subglacial discharge lead to the creation of undercut subglacial discharge outlets, and periods of lower subglacial discharge show no significant undercutting, regardless of the ocean temperature at depth (Fig. 6). This is particularly evident on the southern side of the glacier terminus, where a 100 m undercut subglacial

discharge outlet existed in August 2016 at the same location where an ice ramp protruded 125 m into the fjord during periods of low subglacial discharge in May 2017 and September 2018 (Fig 2c; Fig. 7). While the velocity field from near-glacier kayak surveying suggests that the plume rises just north of the protruding ice ramp in September 2018 (Jackson and others, 2020), we do not see evidence of an undercut subglacial discharge outlet at this location (Fig. 2b).

Although plume-melt theory would predict undercutting in the vicinity of an upwelling subglacial discharge plume due to high water velocities and ocean temperatures at the grounding line, ice ramps of similar sizes have previously been observed near subglacial discharge outlets. At Kangerlussup Sermia, multibeam sonar revealed the presence of undercut glacier morphology near the location of subglacial discharge outlets as predicted by hydropotential gradient (Fried and others, 2015, 2019). Adjacent to one of these undercut outlets, however, was a large protrusion in the terminus of a similar aspect ratio to the ice ramp observed at LeConte Glacier (grounding line depth/overcut length $\simeq$ 1.6).

Evidence exists for ice ramps at several marine terminating glaciers, but these underwater protrusions have largely been ignored in models of iceberg calving and submarine melting due to the overwhelming percentage of undercutting previously observed at Greenlandic tidewater glacier termini, as well as the inability for plume-melt theory to predict submarine melt rates over an overcut ice face (as described further below). We show, however, that even during periods of high submarine melting, the submarine terminus of a tidewater glacier can be mostly overcut, and in particular, large submarine ice ramps can persist through the summer melt season.

2.4.3 An example of extreme overcutting: submarine ice ramps

Our observations clearly show that marine terminating glaciers can support protruding ice ramps for substantial periods of time (Fig. 2c). Prior work has shown that ice ramps develop in models under periods of low melt (Mercenier and others, 2019, 2020), and these ice ramps have previously been observed at several grounded lake-terminating glaciers in New Zealand (Dykes and others, 2011; Robertson and others, 2012; Purdie and others, 2016) and Patagonia (Warren and others, 2001; Sugiyama and others, 2019), as well as at grounded marine terminating glaciers in Alaska (Hunter and Powell, 1998) and Greenland (Chauché and others, 2014; Rignot and others, 2015). The occurrence of large submarine calving events previously at LeConte Glacier (Motyka, 1997; Motyka and others, 1998) suggests that these ice ramps could extend 200-300 m into the proglacial fjord and be a regular occurrence at this tidewater glacier, despite the high melt rates.

While investigating the formation of these ice ramps is beyond the scope of this study, several lines of observational evidence suggest potential mechanisms for their formation and persistence. The depth-varying profile of submarine melting at LeConte Glacier presented here, and in Sutherland and others (2019), show elevated submarine melt rates at the surface in May 2017 and September 2018 (Fig. 6). If you start with a vertical terminus, a difference in melt rate between the surface and grounding line of 1.5 m d^{-1} could form an ice ramp of the size observed (150 m) in 100 days purely from submarine melting. With the addition of subaerial calving events that extend beneath the waterline and sediment insulating the ice near the grounding line (e.g., Hunter and Powell, 1998), this ice ramp could form even quicker. Between May 2017 and September 2018, Eidam and others (2020) observed the formation of a sediment mound ~40 m thick that advanced with the glacier at the location of the protruding ice ramp. It is possible that

the ice ramp extended beneath the surface of this sediment mound, making it larger than appears in our multibeam point clouds of the ice face. This additional sediment could have insulated the lower portion of the ice ramp and counteracted buoyancy forces, allowing it to persist, and even grow, despite having just gone through a summer melt season.

In addition to insulation from sediment, melt rates are likely enhanced towards the surface of the water column by a more energetic velocity field in the upper ocean, as suggested by near-terminus ocean observations at LeConte Glacier. In addition to horizontal recirculations, or eddies, driven by the outflowing discharge plume (Slater and others, 2018; Kienholz and others, 2019), near-glacier moorings have revealed the presence of internal waves, excited by the upwelling subglacial discharge plume, that enhance velocities across the terminus (Cusack and others, in press). Both the near-glacier moorings (Cusack and others, in press) and surveying with kayaks (Fig. S7 in Jackson and others, 2020) shows that the kinetic energy of the along-ice flow increases towards the surface, which should lead to elevated submarine melt rates towards the surface and contribute to the formation of an ice ramp over time. Near surface enhancement of subaqueous melt has also been suggested at lake terminating glaciers, whereby atmospherically warmed surface waters cause enhanced melt rates at the top of the water column, resulting in the formation of ice terraces (Sugiyama and others, 2019). However, ice terraces are typically characterized by abrupt changes in slope beneath the surface warmed layer, in direct contrast with the gradual overcut slope observed at the ice ramp at LeConte Glacier (Fig. 2c).

These ice ramps are not currently represented in models of near-terminus glacier dynamics and change (e.g., Brinkerhoff and others, 2017; Cowton and others, 2019; Ma and Bassis, 2019; Slater and others, 2021). In addition, modeling of the ice-ocean interface typically

only includes terminus morphologies that are either purely vertical or are undercut (e.g., Slater and others, 2017, 2021). Together, this suggests that we are missing an important process in understanding the evolution of glacier termini. Recent modeling investigations into near terminus glacier dynamics have found that, depending on the profile of submarine melting and the resulting terminus morphology, iceberg calving fluxes can either be enhanced (resulting in a "calving multiplier") or suppressed due to nonlinear relationships between the morphology and ice flow (O'Leary and Christoffersen, 2013; Wagner and others, 2016; Ma and Bassis, 2019). Therefore, having realistic constraints on the shape of glacier termini beneath the waterline to input into these models is essential for understanding the glacier evolution through time.

2.4.4 Further evidence for elevated submarine melt rates

While our results are only the second instance of direct melt rate estimates from repeat multibeam sonar imaging, the elevated melt rates described in this study are in line with other recently published estimates from LeConte Glacier (Sutherland and others, 2019; Jackson and others, 2020, 2022). Sutherland and others (2019) calculated submarine melt rates for all portions of the terminus where the glacier did not calve subaerially between scans in August 2016 and May 2017. Our thresholding method allowed us to estimate melt rates for portions of the terminus that experienced subaerial iceberg calving that did not extend beneath the waterline. Despite these different methodologies, the melt rates described here closely match those described in Sutherland and others (2019; Fig. 6). In September 2018, our estimated melt rates are 1-2 m d^{-1} lower than those determined by near-terminus hydrographic observations (Jackson and others 2020). For all three field campaigns, the meltwater volume flux derived from the flux-gate method results in submarine melt rates of 5-18 m d^{-1} (Jackson and others, 2022). While the

submarine melt rates derived from ocean observations are larger than those estimated from multibeam sonar, Jackson and others (2022) note that the multibeam-derived melt rates are likely biased low due to incomplete coverage of the terminus, particularly in the vicinity of the upwelling of the subglacial discharge plume, where turbid, fast flowing water makes acoustic mapping difficult. In addition, the flux-gate method is likely biased high if melt from icebergs contributes to the meltwater flux between the ocean transect and glacier terminus. Regardless, the vast discrepancy between the submarine melt rates derived from observations at LeConte Glacier and those derived by plume-melt theory suggest that modifications to standard parameterizations are needed (Jackson and others, 2022).

In addition to the magnitude of submarine melt, our observations support other recent results from LeConte Glacier showing that submarine melt is much more sensitive to the amount of subglacial discharge and resulting near-glacier ocean currents than it is to ocean temperature (Jackson and others, 2020, 2022). In August 2016 the glacier experienced average submarine melt rates that were 2.6 times higher than those in September 2018, despite similar ocean temperatures at the time of data collection (Fig. 6, 7a). Instead, the glacier in September 2018 had comparable melt rates to May 2017, when the ocean temperature was 2 times lower (Fig. 6, 7a), suggesting that ocean thermal forcing is not the main control on the rate of ice melt. Instead, the flux of subglacial discharge in August 2016 was 2 times higher than September 2018 and 4 times higher than in May 2017 (Fig. 7b), supporting the recent findings that subglacial discharge plays a much larger role than ambient ocean temperature in controlling the submarine melt rates of glacier termini.

Our results suggest two potential reasons for the discrepancy between plume-melt theory and observed melt rates: secondary circulation in the fjord and the persistent overcutting of the

submarine terminus. The influence of subglacial discharge may currently be underestimated by plume-melt theory because the upwelling of plumes not only influences the vertical velocity of the water column but can also induce secondary circulation in the fjord due to internal waves (Cusack and others, in press) and horizontal circulation (Slater and others, 2018; Kienholz and others, 2019). By including horizontal water velocities in plume-melt theory at LeConte Glacier, Jackson and others (2020) found that melt rates were two orders of magnitude greater than standard theory predicts and more closely matched observations. This could explain why even away from the upwelling discharge plume, we observe elevated submarine melt rates (described above; Sutherland and others, 2019). Furthermore, the discrepancy between theory and observations could be affected by the overcutting of the glacier itself, as discussed below.

2.4.5 Implications of overcut terminus morphology on plume-melt theory

Our observations of seasonal variations in terminus morphology and submarine frontal ablation suggest that feedbacks between glacier shape and its rate of change might exist. The highest frontal ablation rates in August 2016 occur directly above the location of the subglacial discharge outlet on the southern side of the terminus (Fig. 5a), suggesting the plume upwells along the undercut ice face. During periods of low subglacial discharge, however, frontal ablation rates reach a maximum on either side of the protruding ice ramp (Fig. 5b, 5c). Near terminus ocean measurements (Jackson and others, 2020) support our observations that the upwelling discharge plume was shifted to the north of the ice ramp, suggesting that the shape of the submarine terminus can alter the path of the glacial plume as it upwells along the face of the glacier and cause spatial variations in the submarine melt rate.

The interaction between upwelling plumes, the ice-ocean boundary layer, and overcut terminus morphology are currently unexplored. Previous work examining plume and boundary layer dynamics have been exclusively focused on the parameter space from no slope (i.e., beneath sea ice or an ice shelf; Jenkins, 1991) to vertical slope (i.e., idealized tidewater glacier termini; Kerr and McConnochie, 2015). Within this parameter space of zero to vertical slope, studies have found that the slope can affect the entrainment in subglacial discharge plumes and associated melt rates (Jenkins, 2011; Slater and others, 2017). In addition, the slope of the ice-ocean boundary layer has been shown to influence the distance over which the transition from laminar to turbulent flow occurs (Malyarenko and others, 2020). However, it is currently unknown how overcut terminus morphologies interact with the ice-ocean boundary layer and upwelling plumes.

An overcut terminus might pose several challenges to the theoretical underpinnings of plume-melt theory. First, plume-melt theory couples buoyant plume theory with the 3-equation melt parameterization, under the assumption that the plume stays attached to the wall (due to the Coanda effect) and thus plume velocities control boundary layer transports (Jenkins, 1991; Jenkins 2011). If the terminus slope is moderately overcut, it is possible that the Coanda effect would continue to take place, drawing the upwelling plume towards the ice face (Kimura and others, 2014). However, if the ice face is sufficiently overcut, buoyant plumes could detach from the glacier terminus as they upwell, uncoupling the plume from the boundary layer. Second, the 3-equation melt parameterization assumes that shear instabilities – as opposed to convective instabilities – control fluxes of heat and salt across the inner boundary layer (Holland and Jenkins, 1999; Malyarenko and others, 2020). While the validity of this assumption has been explored for vertical ice fronts (e.g., McConnochie and Kerr, 2017), it might be even more

problematic at overcut ice. Thus, both the boundary layer dynamics and the representation of the outer velocity field could be significantly misrepresented if standard plume-melt theory is applied to overcut ice.

The detachment of plumes from the ice front would not only affect the melt rates but also the evolution of the plumes themselves. In this regime, the upwelling melt plume would act more like a classical buoyant plume rising with entrainment on all sides. Unbounded by a glacier face, the rising plume would have approximately twice the surface area and entrainment (e.g., Ezhova and others, 2018), increasing its volume flux and reaching its depth of neutral buoyancy more rapidly.

We speculate that overcutting, with plumes detaching from the ice face, might lead to more efficient export of meltwater from the boundary layer. This would weaken the insulating buffer of cold, fresh water that accumulates near the ice-ocean interface, potentially enhancing heat and salt transfer across the boundary layer and elevating rates of submarine melt. More detailed observations of the ice-ocean boundary layer and near-terminus ocean currents are needed to better understand how the overcutting of glacier termini might affect the boundary layer dynamics and evolution of the upwelling plumes.

2.5 Conclusions

Reconciling the drivers of ocean-induced glacier change has remained elusive due to the difficulty of observing terminus geometry beneath the waterline. This work provides the first observations of time-varying terminus morphology and uses concurrent measurements of environmental forcings to show that, despite high subglacial discharge and ocean temperatures, the majority of the terminus at LeConte glacier is overcut. In addition, we show that the location

of and flux from subglacial discharge outlets acts as a key control on submarine terminus change, with the southern side of the terminus sustaining a large ice ramp in periods of low discharge, despite its proximity to the discharge outlet. Our results show that submarine melt rates were relatively high in summer (August 2016) when subglacial discharge was at a maximum, and lowest in late spring (May 2017) when the discharge was low, in line with theoretical predictions that submarine melt rates highly depend on the magnitude of subglacial discharge emerging at the grounding line.

While our results support the dependence of submarine melt on subglacial discharge, the submarine melt rates we find confirm recent ocean and acoustic observations that suggest overall submarine melt rates are up to two orders of magnitude higher than standard plume-melt theory predicts at LeConte Glacier. The persistent overcutting of LeConte Glacier's submarine terminus provides challenges for current implementations of plume-melt theory to estimate submarine melt rates, as the understanding of buoyant plume and ice-ocean boundary layer dynamics in a regime of overcut ice slopes is largely unexplored.

The dynamic nature of the submarine terminus has implications for the path of near-terminus ocean currents, glacier stresses, and potentially calving dynamics. Our findings challenge the assumption that the terminus is either purely vertical or undercut across its width. More long-term observations of submarine terminus morphology, grounding line bathymetry, and near-terminus ocean conditions are necessary to obtain a process-based understanding of the mechanisms that control the evolution of the submarine terminus and the timescales of these changes. In the future, combining this with measurements of the subaerial terminus will allow further investigation of the feedbacks between submarine melting and glacier morphology,

resulting in a better understanding of the influence that submarine glacier change plays in near-terminus glacier dynamics.

2.6 Bridge

In Chapter II, I use direct observations of the morphology of a submarine glacier terminus across three years to show that the glacier is predominately overcut despite high melt rates and localized subglacial discharge. This directly contradicts current theory that predicts submarine melt rates and terminus morphology as being primarily dependent on proximity to subglacial discharge outlets, suggesting that other processes occurring in the water column are missing in these commonly used parametrizations. In Chapter III, I investigate one particular understudied modification of the water column – the input of meltwater from ice mélange – and discuss its implications for submarine melt rates.

CHAPTER III

ICE MÉLANGE MELT DRIVES CHANGES IN OBSERVED WATER COLUMN STRATIFICATION AT A TIDEWATER GLACIER IN GREENLAND

This chapter has been published in a pre-print server and is under review as:
Abib, N., Sutherland, D. A., Peterson, R., Catania, G., Nash, J. D., Shroyer, E. L., Stearns, L. A., and Bartholomaus, T. C. (2024). Ice mélange melt drives changes in observed water column stratification at a tidewater glacier in Greenland, The Cryosphere Discussions, doi: https://doi.org/10.5194/egusphere-2024-504

Author Contributions: Nicole Abib, David A. Sutherland, and Rachel Peterson conceived the study. Nicole Abib conducted the analysis and wrote the original manuscript. David A. Sutherland, Rachel Peterson, Ginny Catania, Emily L. Shroyer, and Timothy C. Bartholomaus supported the interpretation of the results and contributed to the preparation of the manuscript. David A. Sutherland, Ginny Catania, Jonathan D. Nash, Emily L. Shroyer, Leigh A. Stearns, and Timothy C. Bartholomaus developed the original ideas to conduct fieldwork and obtained the observations presented here.

3.1 Introduction

Ongoing observations have documented the rapid breakup of Greenland's ice tongues (e.g., Wilson et al., 2017; Millan et al., 2023) and the associated dynamic thinning and retreat of its marine terminating outlet glaciers (King et al., 2020; Greene et al., 2024). The rapid retreat of these glaciers can be attributed to environmental forcings occurring at the ice-ocean boundary

(Nick et al., 2009; Murray et al., 2010; Carnahan et al., 2022). One key forcing is proposed to be a reduction in the persistence of rigid ice mélange, a (semi-)permanent conglomeration of icebergs, brash ice, and sea ice at glacier termini that persists for weeks to years (Joughin et al., 2008; Amundson et al., 2010). Although several studies have suggested that meltwater from icebergs can alter the ocean forcing near tidewater glaciers (Davison et al., 2020, 2022; Kajanto et al., 2023; Hager et al., 2023), the influence of ice mélange meltwater and its temporal variability have been neglected. By volume, ice mélange primarily consists of deep-keeled icebergs, suggesting previous studies estimating subsurface iceberg melt are relevant to understanding how icebergs modify glacier-adjacent fjord waters (e.g., Enderlin et al., 2016; FitzMaurice et al., 2016; Moon et al., 2018; Cenedese and Straneo, 2023). However, many of these studies are either model-dependent or rely on indirect measurements or parameterizations of iceberg melt rates (Moon et al., 2018; Jackson et al., 2020). Nevertheless, the processes by which a dense and rigid conglomeration of icebergs, such as ice mélange, influence both glacier dynamics through providing physical resistance to glacier flow and ocean stratification by providing a sustained source of cool and fresh water within fjords remains largely unexplored.

Ice mélange can influence the freshwater export from of Greenland's glacial fjords by releasing meltwater over a range of depths in the water column, often below the main pycnocline. Changes in the freshwater flux exiting these glacial fjords can enhance exchange with warm ocean shelf waters by influencing fjord stratification and subsequently the depth and velocity at which the subglacial discharge plume exits the fjord (Straneo et al., 2012; Cowton et al., 2016; Carroll et al., 2017; Slater et al., 2022). This enhanced exchange can in turn influence the behavior of Greenland's outlet glaciers by increasing submarine melting of glaciers and ice mélange, thereby creating a complex feedback loop between the ocean, glacier, and ice mélange

itself (Amundson et al., 2010; Howat et al., 2010; Davison et al., 2020; Wood et al., 2021). At present, potential feedbacks due to ice mélange presence are commonly neglected in ocean-glacier models at the fjord and coarser scales (Carroll et al., 2015, 2017; Krug et al., 2015; Xu et al., 2013; Slater et al., 2017a, b; Kimura et al., 2014; Slater et al., 2016; Bao and Moffat, 2024). However, a recent model study found that including iceberg meltwater increased the net up-fjord heat flux in Sermilik Fjord by ~10% (Davison et al., 2020). Therefore, understanding the relationship between ice mélange meltwater and buoyancy-driven circulation forced by subglacial discharge has important ramifications for long term glacier stability.

Here we use an opportunistic hydrographic dataset collected before and after the melt, breakup, and down-fjord transport of an ephemeral ice mélange to investigate the extent to which ice mélange meltwater can modify the near-glacier water column. We show that the ice mélange adds cool and fresh submarine iceberg meltwater that enhances the stratification down to the depth of the outflowing subglacial discharge plume. We then compare these observations to those of an adjacent fjord, where ice mélange seldom forms in the summertime, to show that ice mélange meltwater creates fundamental differences in their upper layer hydrography despite their proximity and shared source of offshore ocean waters. We suggest that in addition to the current scientific focus on long-lived ice mélange events in front of large outlet glaciers like Sermeq Kujalleq and Helheim Glacier, the changes in stratification of the water column induced by even a four-day ephemeral ice mélange event show that more work should be done to quantify the frequency, duration, and oceanographic implications of these short-lived events in proglacial fjords.

3.1.1 Physical setting

Kangilliup Sermia (also known as Rink Isbræ: 'RNK') is a deeply grounded (~1,000 m; Morlighem et al., 2017, 2022) and fast flowing glacier in the Uummannaq District of Central West Greenland (Fig. 1), with an average ice velocity of 4,200 m yr^{-1} (Bartholomaus et al., 2016) with a corresponding ice flux of 11.6 Gt yr^{-1} (Wood et al., 2021). Kangilliup Sermia terminates in Karrats Isfjord, which branches off from Uummannaq Bay ~70 km from the glacier's terminus. The neighboring Kangerlussuup Sermia ('KAS') is a much smaller outlet glacier, with a maximum grounding line depth of 330 m (Morlighem et al., 2017, 2022) and average velocity of 1,800 m yr^{-1} (Bartholomaus et al., 2016). Several sills are present in the proglacial fjord of Kangilliup Sermia, the shallowest being at a depth of ~400 m at distance of 50 km from the glacier's terminus (~1,000 m; Morlighem et al., 2017, 2022). Although it is a shallower fjord overall, Kangerlussuup Sermia also has a ~400 m deep sill near the fjord's mouth, which is deeper than the grounding line depth of the glacier (Morlighem et al., 2017, 2022). While both fjords share the same offshore ocean conditions, the difference in grounding line depth between the two results in the subglacial discharge plume at Kangilliup Sermia equilibrating at a neutral buoyancy depth of ~120-220 m, while the plume reaches the surface of the fjord at Kangerlussuup Sermia (Chauché et al., 2014; Carroll et al., 2016; Jackson et al., 2017; Slater et al., 2022).

The two neighbouring fjords exhibit contrasting ice mélange seasonality and characteristics. Kangilliup Sermia typically has ice mélange present from January to June (Fried et al., 2018). After the breakup of winter ice mélange, ephemeral ice mélange forms episodically after large, full-thickness calving events during the summer months until the reformation of the more persistent winter ice mélange. When ice mélange is present, the icebergs within it have

average keel depths of up to 300 m (Sulak et al., 2017). Kangerlussuup Sermia similarly has ice mélange present only between January to June, with no summertime mélange observed (Fried et al., 2018). When present, the icebergs from Kangerlussuup Sermia are much smaller, with average keel depths of up to 190 m (Sulak et al., 2017). One reason for this contrast in ephemeral ice mélange occurrence is likely the difference in calving style between the two glaciers, with calving at Kangerlussuup Sermia restricted to smaller serac collapse-style events that cannot produce sufficient concentrations of icebergs to coalesce into an ice mélange, whereas calving at Kangilliup Sermia often consists of capsizing slab-style, full thickness events that fill the fjord with a mixture of tabular icebergs and bergy bits (Fried et al., 2018).

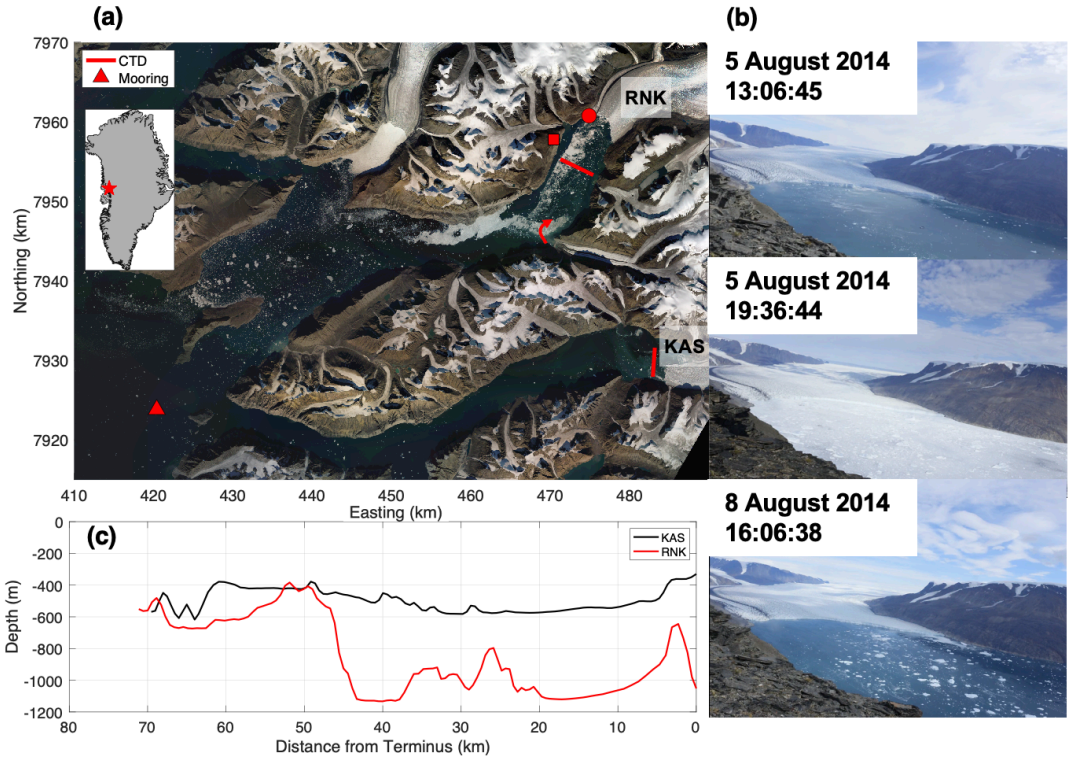

Figure 3.1: (a) True color Landsat 8 image from 07 August 2014, showing the proglacial fjords of Kangilliup Sermia (RNK) and Kangerlussuup Sermia (KAS) overlaid by the location of repeat CTD transects (red line), mooring deployed outside of sill (red triangle), meteorological station (red circle), and time-lapse camera (red square). Red arrow shows direction of riverine sediment plume deflection and inset shows location of image in Greenland. (b) Imagery from a time-lapse

camera (full video in supplement) shows how the ice mélange forms over the course of 6 hours in front of Kangilliup Sermia following an iceberg calving event on 05 August 2014. (c) Thalweg bathymetry of Kangilliup Sermia and Kangerlussuup Sermia extracted from BedMachine v5 (Morlighem et al., 2017, 2022).

3.2 Materials and methods

3.2.1 Ship-based observations

To quantify changes to the water column induced by ice mélange melt, profiles of temperature (T) and salinity (S) with depth were collected from the proglacial fjords of Kangilliup Sermia and Kangerlussuup Sermia in the summer of 2014 (Fig. 1). A cross-fjord transect was repeated within 5 km of the glacier termini using an RBR XR-620 conductivity-temperature-depth (CTD) sensor (Fig. 1; as described in Bartholomaus et al., 2016; Carroll et al., 2018). The two transects bounding the ephemeral ice mélange event here were collected in front of Kangilliup Sermia, on August 4, 2014, approximately one day before the ice mélange formed, and August 11, 2014, two days after icebergs from the ice mélange cleared the fjord. To characterize the ambient water conditions entering these two fjords, T and S outside of each sill where the fjords branch were recorded with co-located CTD casts and a mooring deployed at a depth of 535 m between September 2013-July 2015 (Fig. 1a). Hydrographic measurements were converted to potential temperature and absolute salinities following the Thermodynamic Equation of Seawater 2010 (TEOS-10; McDougall and Barker, 2011). Transects captured water column properties from 2 m to a depth of 800 m. To quantify changes in water column stratification, we use the square of the Brunt Vaisala frequency, N^2, defined as follows:

$$N^2 = -\frac{g}{\rho_o}\frac{\partial \rho}{\partial z} \tag{3.1}$$

where ρ is seawater density, ρ_o is the average density of the water column, g is the gravitational constant, and z is depth. This gives us a measure of the stability of a parcel of fluid to vertical

displacement and is a measure of how stratified the water column is, with higher frequencies indicating a larger gradient in density with depth.

We use *T*-*S* diagrams to analyze whether any observed freshening and cooling of the water column (Fig. 2) was due to the input of meltwater, as opposed to subglacial discharge and/or ambient ocean waters (Gade, 1979; Jenkins, 1999; Straneo and Cenedese, 2015). The calculation of change in exact meltwater fraction due to ice mélange melt was precluded, as typical water mass decomposition methods are under-constrained in Greenland's glacial fjords where only two conservative tracers (in this case potential temperature and absolute salinity) are recorded (Beaird et al., 2015). Therefore, we compare only relative changes in meltwater content due to ice mélange melting.

To assess the general circulation pattern in the fjord, ocean velocity data were collected via two downward-looking 300 kHz RDI Workhorse Acoustic Doppler Current Profilers (ADCP). One ADCP was ship-mounted (SADCP) and typically observed velocities ~150 m depth, while the other ADCP was set-up in a lowered ADCP (LADCP) mode connected to the CTD cage. The LADCP collected velocity profiles coincident with each CTD cast, which allowed us to obtain velocity data much deeper in the water column. We combine the two velocity records here by interpolating them onto a grid with 250 m horizontal, 5 m vertical spacing, and rotated into an along and across-fjord coordinate system.

3.2.2 Subglacial plume model

To predict the depth of neutral buoyancy of the upwelling subglacial discharge plume from Kangilliup Sermia, we use a buoyant plume model (Slater et al., 2016) with a line plume

geometry (Jackson et al., 2017). We initialize our plume model with a 250 m wide line plume and vary its width between 100-500 m for sensitivity testing (Slater et al., 2022). The initial stratification for the plume model comes from transect-averaged hydrographic profiles from the post-ice mélange CTD casts. Subglacial discharge values for the plume model come from Carroll et al. (2016), who integrated the daily surface runoff from the 1 km downscaled Regional Atmospheric Climate Model (Noël et al., 2015), and assumes that all surface runoff drains immediately to the glacier bed through a probability-based hydrologic catchment (see Sect 2.4 in Carroll et al., 2016). Using these initial inputs, we calculate the neutral buoyancy depth of the plume (where it equilibrates into the fjord) by finding the depth at which the density of the waters in the plume is equal to that of the ambient stratification.

3.2.3 Ice mélange melt rate

To determine whether the change in our hydrographic observations could realistically be explained by ice mélange melt in the proglacial fjord of Kangilliup Sermia, we estimate iceberg melt rates using common parameterizations most recently compiled by Moon et al. (2018). The parameterized iceberg melt rate results in a depth-varying melt rate that includes wave driven melt, convection driven melt both above and below the waterline, solar radiation driven melt above the waterline, and turbulence driven melt beneath the waterline. As inputs to these parameterizations, we use the average air temperature and wind speed just prior to the ice mélange event taken from a meteorologic station on the north side of the fjord (Fig. 1a). For the initial ocean conditions, we utilize the T and S profiles collected before the ice mélange event and consider the fjord to be 80% covered by sea ice, icebergs, and bergy bits between the transect and glacier terminus as seen in Landsat 8 imagery from August 5, 2014. In the model

higher fjord ice concentrations lead to less melting through wave driven erosion but increase the influence of turbulent subsurface melting due to the relative difference between the water column velocity and iceberg motion, akin to an ice mélange (Moon et al., 2018). We vary the keel depth of the modeled icebergs between 50 m and 400 m to account for variation in iceberg size within the ice mélange. Finally, we average the melt rate over the depth of the iceberg keel to obtain a depth-averaged melt rate for each iceberg depth class.

Using the depth-averaged iceberg melt rate in combination with an assumption of conservation of volume (Eq. 3.2) and salt (Eq. 3.3), we calculate the volume of ice melt (V_{melt}; Eq. 3.4) in the fjord needed to produce the observed salinity changes.

$$V_{ocean_1} + V_{melt} = V_{ocean_2} \tag{3.2}$$

$$V_{ocean_1} S_1 + V_{ocean_2} S_2 = 0 \tag{3.3}$$

$$V_{melt} = \left(\frac{\Delta S}{S_1}\right) V_{ocean_1} \tag{3.4}$$

Here, subscripts 1 and 2 indicate times 1 and 2 of each transect, V_{ocean} is the ocean volume considered, S is the salinity averaged over that volume, and $\Delta S = S_2 - S_1$. We consider the volume of ocean water between the ocean transect and the glacier terminus between a depth of 5-200 m, where the observed *T* and *S* changes occurred above the depth of the outflowing discharge plume. We vary the depth range considered between 100-300 m to test the sensitivity of this control volume on our calculation. We neglect the influence of freshwater runoff from terrestrial and subglacial sources into the control volume, as they do not substantially change over the duration of the ephemeral ice mélange event described here. We then calculate the percentage of the initial calving event volume (V_{calv}) that melted (V_{melt}):

$$\%\, Ice\ Melted = {}^{V_{melt}}/_{V_{calv}} \tag{3.5}$$

Finally, we calculate the length of time (t) needed to melt this volume of ice:

$$t = {V_{melt}}/{(A_{ice} * \dot{m})} \quad (3.6)$$

where A_{ice} is the area of the fjord covered by ice mélange, and $\dot{m}$ is the estimated iceberg melt rate. The variables V_{ocean}, V_{calv}, and A_{ice} were determined by manually digitizing the area between the ocean transect and the glacier, the area of the terminus that changed after the iceberg calving event, and the area of the fjord occupied by ice mélange, respectively using Landsat 8 optical imagery captured on August 5, 2014, and August 7, 2014. These calculations allow us to see if the ephemeral ice mélange event investigated here could have produced the volume of melt necessary to explain the observed freshening of the water column within a duration of time that is similar to the spacing between our hydrographic observations.

3.3 Results

An ephemeral ice mélange formed in the proglacial fjord of Kangilliup Sermia on August 5, 2014, following an iceberg calving event that took place ~2.3 km from the southern edge of the glacier's terminus at ~14:00 GMT. A volume of 3.9 x 10^8 m^3 of ice (assuming full-thickness calving) calved into the fjord and froze into place over the course of 30 minutes (Fig. 1; Supplementary Video). This ice mélange remained frozen in place for ~12 hours, until August 6, 2014, at ~02:00 GMT, at which point it began to break up and move down-fjord. The majority of the ice mélange was transported out-fjord along the north side wall, but a recirculation in the surface current was seen to transport portions of the ice mélange back towards the terminus along the south side of the fjord. All icebergs from the original calving event were cleared from

the fjord after August 9, 2014, and post-event hydrographic observations were collected on August 11, 2014.

Following the formation, breakup, and down-fjord transport of this ephemeral ice mélange event, we observe a freshening and cooling of the water column. Hydrographic measurements taken after this ice mélange event show that the average water column *T* and *S* decreased by 0.19 °C and 0.18 g kg^{-1} respectively (Figs. 2a, b, S1; from 2.35 ± 0.44 to 2.15 ± 0.48 °C and 34.42 ± 0.32 to 34.25 ± 0.48 g kg^{-1} between a depth of 5-800 m). The most significant changes to the water column occurred above a depth of 200 m, where the average *T* cooled by 0.18°C (from 1.75 ± 0.31 to 1.57 ± 0.31 °C) and *S* decreased 0.25 g kg^{-1} (from 33.95 ± 0.23 to 33.70 ± 0.50 g kg^{-1}). These hydrographic changes coincided with increased stratification to a depth of 100 m, with the most significant departure from pre-mélange conditions at depths <60 m (Fig. 2c).

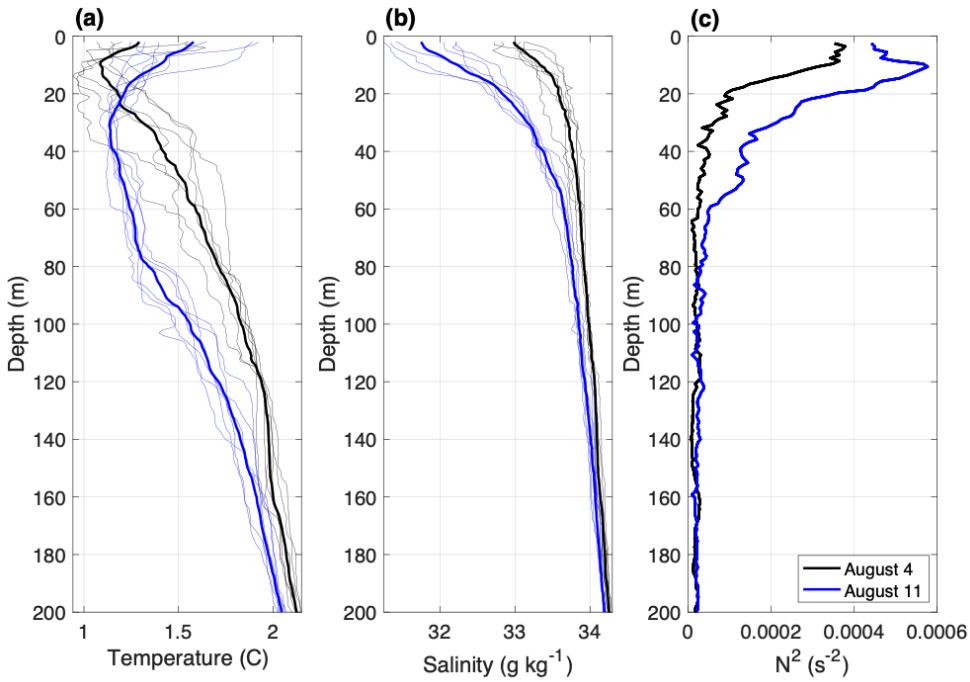

Figure 3.2: Changes in T (a), S (b), and N^2 (c) pre- (black line; August 4) and post-event (blue line; August 11; full profiles shown in Fig. S1). Thin lines indicate individual CTD casts across the width of the glacial fjord, while thick lines indicate the average. In (c), N^2 has been smoothed with a 10 m moving average.

Below 400 m, there is no significant change between the pre- and post-ice mélange CTD casts (dS = -0.04 g kg^{-1} and dT = -0.07 °C; Figs. 3a, S1). Between a depth of 280-320 m (Fig. 3a label I), the water properties move towards the runoff mixing line in both the pre- and post-ice mélange event CTD casts, indicating the location where the discharge plume enters the water column horizontally. Above this depth, between 20-280 m (Fig. 3a label II), the water column properties then nearly parallel the meltwater mixing line. In particular, between a depth of 50-100 m, where the largest changes in stratification occur, the post-event water column properties plot further down the meltwater mixing line (Figs. 3b and S2a), indicating the addition of meltwater in the water column. Starting at a depth of 10 m and 30 m in the pre- and post-ice mélange event CTD casts, respectively, the water column becomes warmer again and shifts back

towards the runoff mixing line, suggesting the mixing of the ice mélange melt-modified waters with freshwater input at the fjord surface (Figs. 3a label III, 3b, and S2).

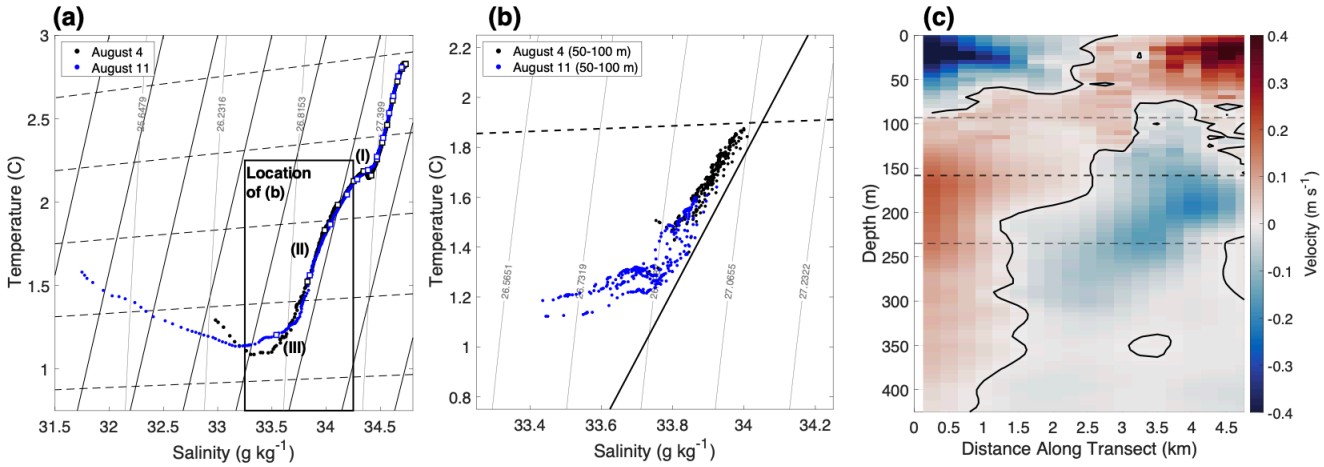

Figure 3.3: (a) Average water column properties pre- (black dots) and post-event (blue dots) overlaid on isopycnal contours (density in kg m^{-3} –1000). Mixing lines between freshwater discharge (dashed lines) and submarine melting of ice (solid lines) with ambient ocean water are included, and a white square marker indicates the depth at 50 m intervals between 0-800 m. Roman numerals correspond with locations described in text. (b) Zoom-in on (a) with data only shown between depths of 50-100 m. (c) Gridded ADCP-derived along-fjord velocity on August 11, 2014, with positive values indicating flow toward the glacier and a black contour at 0 m s^{-1}. Distance across fjord increases from southward. The location of the predicted minimum (93 m), maximum (235 m), and mean (158 m) depth of neutral buoyancy of the subglacial discharge plume is shown (black dashed lines).

A transect of water column velocities from August 11, 2014, across the fjord shows a recirculation gyre present at the surface, with water flowing out-fjord along the northern side at a rate of 0.142 ± 0.063 m s^{-1} and in-fjord on the southern side at 0.154 ± 0.049 m s^{-1} at depths <60 m (Figs. 3c and S3a; additional ADCP transects shown in Fig. S4). The fjord-wide average flow direction is towards the glacier at the surface and out-fjord between a depth of ~160-315 m at rates of 0.013 ± 0.012 m s^{-1} and 0.017 ± 0.011 m s^{-1} respectively. Beneath a depth of 450 m, the average flow direction is towards the glacier at 0.016 ± 0.009 m s^{-1} (Fig. S3a). In the across-fjord transect, we see a signature of the outflowing plume at a depth of 100-325 m, which corroborates

the shift towards the runoff mixing line at a depth of ~320 m in *T*-*S* space (Figs. 3a, c, and S3a). Further, buoyant plume theory suggests that the plume reaches neutral buoyancy depth at 158 m when initialized with the post-ice mélange hydrographic observations, a line plume width of 250 m, and average subglacial discharge of 103 m^3 s^{-1} (Fig. 3c). Sensitivity tests indicate the subglacial discharge plume always reaches neutral buoyancy subsurface (Fig. 3c) over a large range of line plume widths (100-500 m) and subglacial discharge magnitudes (25-450 m^3 s^{-1}).

Modeled iceberg melt rates vary between 0.08-1.40 m d^{-1} (Fig. S3) using the fjord velocity profiles averaged over the northern half, southern half, and entire fjord, as well as the average air temperature and wind speed just prior to the ice mélange event (Fig. S5). Iceberg melt rates are highest at the surface (0.78 ± 0.51 m d^{-1} above 25 m), reaching a secondary maximum at 200 m depth (0.29 ± 0.10 m d^{-1}). We further evaluate these predicted melt rates for an iceberg with a modeled keel depth of 200 m to investigate the same depth range over which we observe changes to the water column properties following the ephemeral ice mélange event. For an iceberg with a keel depth of 200 m, we find depth-average modeled iceberg melt rates of 0.18-0.36 m d^{-1}, with the highest melt rates coinciding with the velocity profile taken from the southern half of the fjord.

Using the pre- and post-ice mélange salinities (S_1 = 33.95 g kg^{-1} and S_2 = 33.70 g kg^{-1}) as inputs to Eq. (4), we find V_{melt} = 5.47 x 10^7 m^3. This volume of ice melt is equivalent to 14% of the initial calving event volume that triggered this ephemeral ice mélange (Eq. 5). At the melt rate estimated ($\dot{m}$ = 0.18-0.36 m d^{-1}), this volume of ice would have taken 5.1-10.5 days to melt completely (Eq. 6). Changing the depth range considered for the conservation of salt calculation only has minor effects, shortening the time to 4.3-8.8 days if we only considered changes above 100 m, and increasing it to 5.7-11.7 days for the upper 300 m. While these time spans for

complete melting of the ice mélange are longer than the 4-day window that the ice mélange persisted in the proglacial fjord, we note that not all icebergs from the mélange melted completely and many were exported out of the glacial fjord.

3.4 Discussion

We use an opportunistic dataset of near-terminus fjord hydrography observations bookending an ephemeral ice mélange event in the proglacial fjord of Kangilliup Sermia to show that the addition of meltwater from ice mélange over the course of one week causes cooling and freshening of the water column that leads to enhanced stratification. We investigate other mechanisms that could explain these changes, including 1) water mass advection, 2) vertical or horizontal mixing of the water column, and/or 3) enhanced freshwater input from subglacial discharge or surface runoff. Yet, we demonstrate below that none of these processes explain the observed hydrographic changes. This implies that even short-lived ice mélange events can alter the surface water column stratification, and this can help explain the large-scale differences in water properties between glacial fjords around Greenland and other locations where iceberg concentrations are high (e.g., Carroll et al., 2018). We discuss these implications with a case study of comparing neighbouring fjords with different stratification profiles, Kangilliup Sermia and Kangerlussuup Sermia, and provide the first observational evidence of the complex feedbacks between ice mélange characteristics, discharge plume-driven circulation, and melt rates at the glacier front.

3.4.1 Alternative water column transformation mechanisms do not explain stratification change

First, we find that neither vertical nor horizontal advection is likely to explain the observed water column transformation. To discern whether the enhanced meltwater presence between a depth of 50-100 m could be attributed to any vertical movement of the density field (i.e., shoaling or deepening isopycnals), we compared the water column properties at this depth range after the ice mélange event to the water column both above and below this depth prior to the additional meltwater input (Fig. S2a). We find that while the shallow water column properties (20-50 m) share some overlap with the post-mélange properties in *T*-*S* space, the water column after the ice mélange event is closer to the meltwater mixing line. This suggests that while deepening of the isopycnals from above could have contributed to the changes observed here, enhanced meltwater input from icebergs also plays a key role in altering the water column properties in this depth range. In addition, we see no evidence that these changes to the water column post-ice mélange event were caused by shoaling of the deeper water column (Fig. S2a). The time series of *T* recorded at the offshore mooring varies by only ~0.25°C, with no significant changes before and after the ice mélange event (Fig. S6). Furthermore, prior work has shown that Kangilliup Sermia's proglacial fjord is hydraulically controlled in summer months, so that little offshore water is being transported over the sill into the fjord (Carroll et al., 2018).

Second, we see no substantial evidence that local mixing of water masses led to the observed freshening and cooling of the water column. To estimate the impact of horizontal mixing on the water column, we compare the across-fjord *T* and *S* gradients to the average temporal change between the two hydrographic transects. The mean temporal change post-event is ~2x larger than any across-fjord variation (Table S1).

Finally, we find that additional freshwater input from subglacial discharge and surface runoff cannot explain the observed cooling and freshening either. A time series of subglacial discharge from Kangilliup Sermia shows a slight peak in magnitude (increase by 17 ± 4.7%) between our two hydrographic surveys (Fig. S7). However, prior work in this fjord has shown that the addition of subglacial discharge results in a warm temperature anomaly, opposite to the cooling signal observed here (Carroll et al., 2016). Furthermore, both the hydrographic observations and buoyant plume modeling presented here (Figs. 3c and S8) and previously (Carroll et al., 2016; Slater et al., 2022) suggest that the subglacial discharge plume reaches a neutral buoyancy deeper than the observed cooling and freshening signal.

The magnitude of surface runoff (Mankoff et al., 2020) is only 1-2% of the subglacial discharge (Fig. S9). Due to the strength of the stratification we observe, this magnitude of surface freshwater input is unlikely to cause a cooling of the water column down to the depth observed here (~200 m). It is possible, however, that this surface freshwater could cause the warm, fresh anomaly seen in the upper 20 m of the water column, which is also subject to variable atmospheric heat fluxes (Figs. 2a, b, and S2b). While not responsible for the observed cooling and freshening observed here, the addition of subglacial discharge and surface water to the fjord might play an indirect role by controlling both the net outflow away from the glacier, as well as any recirculation and residence time of icebergs in the fjord (Fig. 3c; further discussed in Sect. 4.2.1).

3.4.2 Short-term ice mélange events as a driver of water column change

Despite the short-lived nature (4 days) of the ice mélange event, our hydrographic observations show a clear cooling (0.18 °C) and freshening (0.25 g kg^{-1}) of the upper 200 m of

the water column following the addition of 3.9 x 10^8 m^3 of calved ice into the fjord (Figs. 2a and b). These changes to the water column led to increased stratification down to a depth of 100 m (Fig. 2c) and *T-S* analysis suggests that this observed freshening and cooling of surface waters can be explained by the submarine melting of icebergs within the ice mélange matrix (Fig. 3b). Prior remote sensing studies in this fjord confirm that typical iceberg keels extend to depths of up to 300 m on average (Sulak et al., 2017), which is the range over which we see water column modification. While iceberg melt itself is responsible for the freshening and cooling signal observed here, it is the sea ice matrix holding the icebergs in place in the proglacial fjord that supports this meltwater injection into the fjord over the course of several days. In this regard, it is the presence of a rigid ice mélange, rather than free floating icebergs, that leads to the observed water column stratification changes. The combination of hydrographic observations, plume modeling, and remote sensing of iceberg keel depths, all point to ice mélange melt being the primary driver for the observed stratification change above the depth of the outflowing subglacial discharge plume.

While we lack prior observational studies investigating the influence of ice mélange melt on the water column, several recent modeling studies have used general circulation models to address this unknown (Davison et al., 2020, 2022; Kajanto et al., 2023; Hager et al., 2023). In both Sermilik Fjord and Ilulissat Icefjord, where ice mélange remains present year-round, numerical simulations (Davison et al., 2020; Kajanto et al., 2023) show that the inclusion of icebergs invigorated the overall fjord circulation, in addition to causing significant cooling (~5°C in Sermilik Fjord and ~4°C in Ilulissat Icefjord) and freshening (0.7 PSU in both fjords) of surface waters. Both studies also found that the inclusion of icebergs was needed to reproduce the in situ hydrographic observations within the fjords. More recent idealized studies have found

that for fjords where iceberg keel depths extend deeper than the entrance sill, the net cooling and freshening effect is larger with increasing iceberg concentrations within the ice mélange (Davison et al., 2022; Hager et al., 2023). Although the ice mélange event reported here is episodic and shows a smaller signal of water column modification than these modeling studies of persistent ice mélange, our observational results generally align. Furthermore, our observations provide constraints for future modeling efforts on understanding the influence of ice mélange melt on fjord stratification. The changes to water column stratification induced by this additional source of freshwater can have implications for the neutral buoyancy depth of subglacial discharge plumes, overall circulation in proglacial fjords, and the subsequent heat transport towards glacier termini.

3.4.2.1 Enhanced residence time of meltwater due to fjord circulation

While the addition of ice mélange meltwater is the primary contributor to the freshening and cooling signal observed in the proglacial fjord of Kangilliup Sermia, a recirculation gyre set up by subglacial discharge and surface water input is likely responsible for the prolonged signature of the short-term ice mélange event observed here. In situ water column velocity measurements show a cyclonic recirculation gyre to a depth of ~60 m in the fjord, with water flowing 0.142 ± 0.063 m s^{-1} out of the fjord on the northern side, and at 0.154 ± 0.049 m s^{-1} into the fjord on the southern side (Fig. 3c). This recirculation pattern can also be seen with optical imagery: as sediment-laden freshwater riverine plumes enter the fjord at the surface, they are deflected to the right (Fig. 1a; Supplementary Video). These in situ observations provide support for prior modeling studies of fjords of this type, which suggested recirculation patterns such as those observed could be explained by either internal Kelvin waves (Carroll et al., 2017) or

standing eddies (Zhao et al., 2023). While we cannot distinguish the source of the observed recirculation pattern here with our limited snapshots of near-glacier water velocities, the mechanism that forms this surface recirculation does not influence our findings that icebergs have an enhanced residence time in this fjord due to surface recirculations (Fig. S4). Together, our observations of water velocities along with previous fjord-modeling results (Carroll et al., 2017; Zhao et al., 2023) show that while these ephemeral ice mélange events are short-lived, the overall circulation pattern in fjords such as Kangilliup Sermia can cause icebergs to continuously recirculate near the glacier terminus. This recirculation extends the overall time scale over which icebergs within the ice mélange can impart meltwater into the upper waters of the proglacial fjord.

3.4.3 Implications for fjords with summertime ice mélange

Previous studies across Greenland have noted that adjacent glaciers exhibit asynchronous dynamic behavior despite similar ocean forcings (Bartholomaus et al., 2016; Carroll et al., 2018; Fried et al., 2018; Catania et al., 2018; Carnahan et al., 2022; King et al., 2018; Cowton et al., 2018; Fahrner et al., 2021). We argue that one missing discussion piece from these studies is the role that ice mélange melt may play in altering near-glacier ocean conditions, and how this influence varies between fjords. The observed freshening and cooling of the upper 200 m of water in front of Kangilliup Sermia illustrates that ice mélange presence can significantly alter water properties at least down to the depth of the outflowing discharge plume, and likely deeper to the depth of the iceberg keels (Fig. 3; Carroll et al., 2016; Slater et al., 2022). We assess the impact of different ice mélange regimes on near-glacier hydrographic properties by comparing observations from Kangilliup Sermia to those of the neighboring Kangerlussup Sermia, as well

as the ambient ocean water beyond the sill in *T*-*S* space (Fig. 4). While both fjords have persistent wintertime ice mélange, summertime ice mélange is only present at Kangilliup Sermia, allowing us to investigate the influence that the addition of ice mélange meltwater has on the surface water column stratification in two fjords that share the same ambient water source.

Water column properties in Kangerlussuup Sermia match those offshore to a depth of ~60 m, where the fjord water properties are slightly cooled, indicating the presence of outflowing glacially modified water at the fjord surface (Fig. 4; Carroll et al., 2016, 2018; Jackson et al., 2017). The water column properties in front of Kangilliup Sermia, however, deviate from the ambient ocean water at ~280-320 m depth due to the outflowing subglacial discharge plume (Figs. 3c and 4c; Carroll et al., 2016; Slater et al., 2022). Above this depth, we see the water column properties follow the meltwater mixing line once again, indicating the presence of iceberg melt. This additional iceberg melt results in surface waters in the proglacial fjord of Kangilliup Sermia that are cooler and fresher than both the waters outside of the sill and the neighboring fjord, Kangerlussuup Sermia. Thus, at Kangilliup Sermia, the injection of cold, fresh water beneath the depth of the sill has the effect of progressively cooling the upper layer of the fjord over the course of the summer, aligning with previous modeling results (Davison et al., 2022; Hager et al., 2023).

To quantify the impact that multiple ephemeral ice mélange events may have on fjord hydrography, we determine the number of events needed to explain the change in *S* between the near-glacier waters and those offshore. Using Eq. (3.4), we find that the volume of meltwater needed to freshen the upper 200 m of the water column compared to the offshore water properties ($S_{offshore} - S_{fjord}$ = 0.09 g kg^{-1}) is 1.42 x 10^8 m^3. Using the calculated meltwater volume from the ice mélange event discussed above (5.47 x 10^7 m^3, described in Sect. 3.3), we estimate

that the equivalent of ~2.6 events similar in magnitude to the one on August 5, 2014, are needed to match the observed differences in *S*. Manual inspection of cloud-free satellite imagery from Landsat 8 and Sentinel 2 during the summer of 2014 shows that ephemeral ice mélange events occurred at least ~4 times over the course of the melt season, suggesting that the meltwater input from these ice mélange events is a reasonable explanation for how the upper layer fjord waters are modified compared to offshore. The implication is that even short-lived ice mélange events have the potential to cause lasting changes to water column stratification.

By instigating cooling throughout the entire water column for prolonged periods of time, the addition of ice mélange meltwater to the proglacial fjord has the potential to reduce submarine melt rates at the glacier terminus in the summer months when iceberg keel depth exceeds the depth of the sill (Davison et al., 2022; Hager et al., 2023). Overall, understanding how submarine melting of icebergs can alter fjord circulation and subsequent heat exchange with the shelf is an important piece for modeling the sensitivity of marine terminating glaciers to near-glacier fjord conditions, particularly for glaciers with ice mélange conditions similar to those at Kangilliup Sermia. Prior work understanding ice mélange-ocean feedbacks has primarily focused on tidewater glaciers with permanent ice mélange in their proglacial fjord, like Sermeq Kujalleq and Helheim Glacier. Our observations show that even short-lived ice mélange events have the potential to cause lasting changes on water column stratification in glacier-adjacent waters, suggesting that more work should be done to understand the dynamics and feedbacks of ice mélange in systems with seasonal and ephemeral ice mélange presence. Ultimately, more hydrographic measurements bookending ice mélange events are needed to constrain the exact extent to which meltwater alters fjord stratification and the duration for which this altered stratification persists.

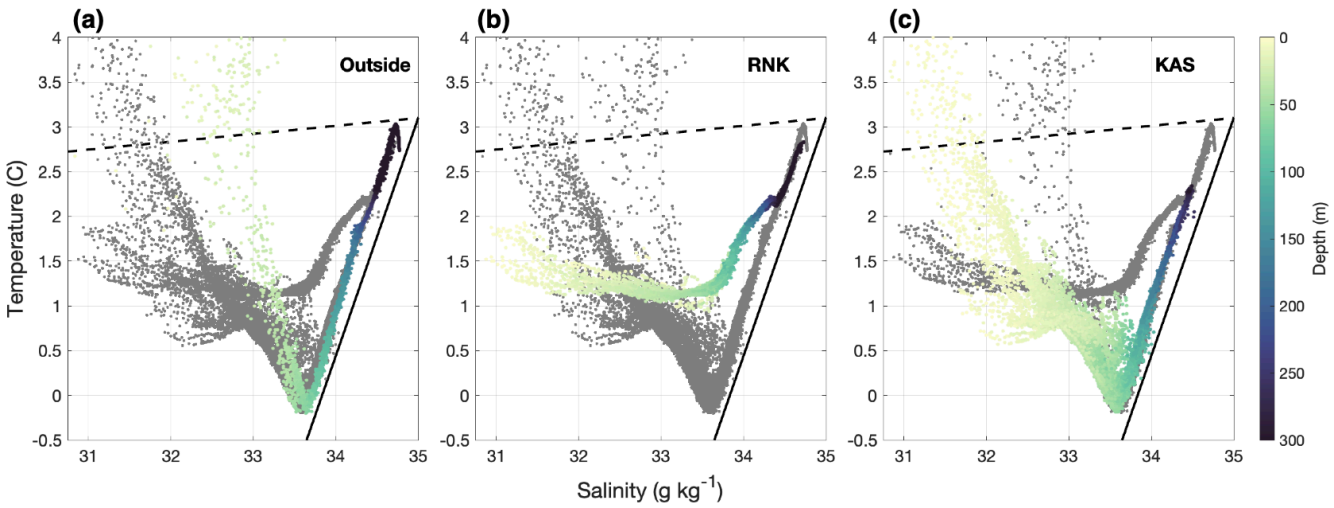

Figure 3.4 Full-depth water column properties outside of the sill (a) and near the termini of Kangilliup Sermia (b) and Kangerlussuup Sermia (c) in T-S space, with water column properties colored by depth in the water column. Mixing lines with freshwater runoff (dashed line) and submarine meltwater (solid line) are superimposed.

3.5 Conclusions

Through examining the first direct observations of hydrographic change induced by an ephemeral ice mélange event, we have shown that the meltwater released from even a short-lived ice mélange can alter the water column stratification by releasing fresh and cool water at depth in the fjord. In particular, we show that the integrated effect of several ephemeral ice mélange events over the summer melt season can explain the observed differences in hydrographic properties between the offshore ocean water and waters glacier-ward of the fjord mouth. We discount other mechanisms that could explain the observed water column changes, such as advection and mixing of the water column, as well as enhanced freshwater input from non-iceberg sources. This enhanced meltwater input can particularly influence ice-ocean systems with deep grounding lines and shallow sills, where the subglacial discharge plume exits the fjord at a depth beneath the extent of ice mélange and the iceberg melt-modified waters can be

recirculated. In addition, glaciers with deeper grounding lines, like Kangilliup Sermia, are often close to flotation and calve via buoyant flexure, which can lead to large episodic calving events that are more likely to produce ephemeral ice mélange and the oceanographic changes observed here. On the other hand, fjords with shallow grounding lines, where the subglacial discharge plume exits the fjord at the surface and iceberg calving events tend to be smaller and more frequent, are less likely to be influenced by ice mélange melt either by its absence overall or by the fast export of any ice mélange meltwater with the outflowing plume. This work stresses the need for more high-temporal resolution coincident observations of both ice mélange characteristics (i.e., keel depth and concentration of icebergs within the sea ice matrix) and fjord hydrography to fully capture the processes by which ice mélange meltwater can contribute to heterogeneous fjord characteristics around the Greenland Ice Sheet.

3.6 Bridge

In Chapter III, I use direct observations of water column hydrography to show that the meltwater input from ice mélange can cause substantial cooling and freshening of the upper fjord layers of a large outlet glacier in Central West Greenland. In Chapter IV, I expand on this study by characterizing ice mélange in a varied suite of glacial fjords to investigate controls on ice mélange presence. I find that ice mélange breakup date is highly correlated with subglacial discharge plume evolution, which suggests that interannual variations in ocean stratification and magnitude of subglacial discharge will alter the length of time that ice mélange can supply buttressing force to the glacier terminus and input meltwater in the upper layers of the water column.

CHAPTER IV

SUBGLACIAL DISCHARGE DRIVES ICE MÉLANGE BREAKUP AT DEEPLY GROUNDED GLACIERS

This chapter is formatted for submission to Journal of Glaciology, where it will be co-authored with David A. Sutherland, Jason M. Amundson, Michalea King, and Ian Joughin.

Author Contributions:

Nicole Abib, David A. Sutherland, and Jason M. Amundson conceived the study. Nicole Abib conducted the analysis and wrote the original manuscript. Michalea King and Ian Joughin processed the Sentinel 1 imagery to obtain ice mélange rigidity. All coauthors supported the interpretation of results and contributed to the preparation of the manuscript.

4.1 Introduction

In recent decades, mass loss of the marine terminating outlet glaciers around the Greenland Ice Sheet has been accelerating, a large part of which is due to an increase in frontal ablation (Wood and others, 2018; Kochtitzky and others, 2022; Greene and others, 2024). The rate of frontal ablation, or the combination of iceberg calving and submarine melting, is influenced by both glacier dynamics and processes occurring at the ice-ocean interface (Nick and others, 2009; Murray and others, 2010; Straneo and Heimbach, 2013; Carnahan and others, 2022). A key component of the ice-ocean boundary that has gained attention for its potential impact on glacier mass loss is the presence of ice mélange, a (semi-) permanent conglomeration of icebergs, sea ice and brash ice in the proglacial fjord (Joughin and others, 2008; Amundson

and others, 2010; Burton and others, 2018). Recent work has postulated that the presence of rigid ice mélange can buttress the termini of glaciers, therefore reducing the rate of iceberg calving and allowing the glacier to stabilize or even advance in winter months (Todd and Christoffersen, 2014; Joughin and others, 2020; Chudley and others, 2023). This process of building up mass at the terminus during winter months has been suggested to buffer the long-term retreat at marine terminating outlet glaciers.

Ice mélange can also influence marine terminating glaciers indirectly by modifying the underlying fjord water on which it floats. As ice mélange persists in the proglacial fjord, it slowly releases cool and fresh water throughout the upper layers of the water column. This injection of iceberg meltwater over a range of upper layer depths can modify fjord stratification and has the potential to alter the depth at which upwelling subglacial discharge plumes reach neutral buoyancy (Straneo and others, 2012; Cowton and others, 2016; Enderlin and others, 2016; Carroll and others, 2017; Slater and others, 2022; Abib and others, 2024). Ice mélange also acts as a physical barrier to flow, imparting drag upon the outflowing glacially modified water (Jenkins, 2011; Hughes, 2022). Together, these changes in water column density and flow path can alter heat exchange with the ambient ocean water beyond the glacier's subaqueous sill, thereby altering the water temperature near terminus that partly controls submarine melt rates (Amundson and others, 2010; Howat and others, 2010; Davison and others, 2020, 2022; Wood and others, 2021; Hager and others, 2024). The presence of ice mélange, therefore, cannot be ignored, as the "glacier-ocean-mélange system" (Amundson and others, 2020) influences tidewater glaciers by both slowing their mechanical deterioration by calving, as well as altering the rate at which the submarine terminus is melted.

Despite the emerging importance of ice mélange, detailed studies have only occurred at a few select large outlet glaciers around the Greenland Ice Sheet: Store Glacier (Walter and others, 2012; Todd and Christoffersen, 2014), Helheim Glacier (Enderlin and others, 2016, 2018; Davison and others, 2020), and Sermeq Kujalleq (Joughin and others, 2008, 2020; Amundson and others, 2010; Cassotto and others, 2015; Enderlin and others, 2016; Khazendar and others, 2019; Kajanto and others, 2023). Both observational and modeling studies at these systems have found evidence for the feedbacks within the glacier-mélange-ocean system discussed above. For example, Joughin and others (2020) found that sustained cool ocean temperatures at depth in Disko Bay led to a prolonged rigid ice mélange at the terminus of Sermeq Kujalleq. The timing of this extended ice mélange correlated with a slowdown in the glacier's velocity, an increase in its thickness at the terminus, and a resulting advance in its terminus position, providing evidence that glacier terminus retreat can be linked to interannual ocean dynamics through its influence on ice mélange persistence and rigidity.

Furthermore, several recent studies have used ocean circulation models with both idealized and glacier-specific geometries to explore the feedbacks between fjord geometry, ice mélange characteristics such as iceberg concentration and keel depths, and water column modification (Davison and others, 2020, 2022; Kajanto and others, 2023; Abib and others, 2024; Hager and others, 2024). For glacial fjords in which the sill is shallower than the keel depth of icebergs within the ice mélange, iceberg meltwater is recirculated at the sill throughout the summer and leads to a net cooling compared to fjords without ice mélange or with sills deeper than the iceberg keel depth (Davison and others, 2022; Hager and others, 2024). This net cooling leads to reduced submarine melt rates at the glacier's terminus throughout the summer season. However, for fjords in Greenland with icebergs that do not extend beneath the sill depth, these

studies have suggested complex patterns of warming and cooling, whereby the surface waters are substantially cooled and contribute to decreased rates of submarine melt, meanwhile the deeper water column is warmed from upwelling Atlantic Water (Davison and others, 2022). In addition, a glacier-specific study found that the release of freshwater form ice mélange melt increased the up-fjord heat flux in Sermilik Fjord by 10% (Davison and others, 2020). These contrasting effects show that the impact of ice mélange on its underlying fjord waters is dependent on both the glacier and fjord geometry, as well as the initial water column stratification.

Despite the progress made on understanding the glacier-mélange-ocean system, we still lack a comprehensive inventory of the spatiotemporal pattern of mélange presence in Greenland. Here we utilize a remote sensing approach to characterize ice mélange across a varied set of proglacial fjords in Greenland to investigate feedbacks between its presence and physical characteristics within the water column. We use satellite imagery to quantify the formation, duration, and breakup of ice mélange in nine different fjords in the Uummannaq District of Central West Greenland between 2013-2021. For each of these fjords, when ice mélange is present and data are available, we determine the variations in the iceberg size distributions present within the ice mélange. Finally, we use available in situ, modeling, and reanalysis data to investigate the environmental, geometric, and dynamic forcings that lead to fjord-by-fjord variations in ice mélange. Using this novel database of ice mélange characteristics and local forcings, we highlight an example in which interactions between ambient ocean temperature, fjord geometry, and iceberg keel depth led to a change in ice mélange characteristics over the course of several years.

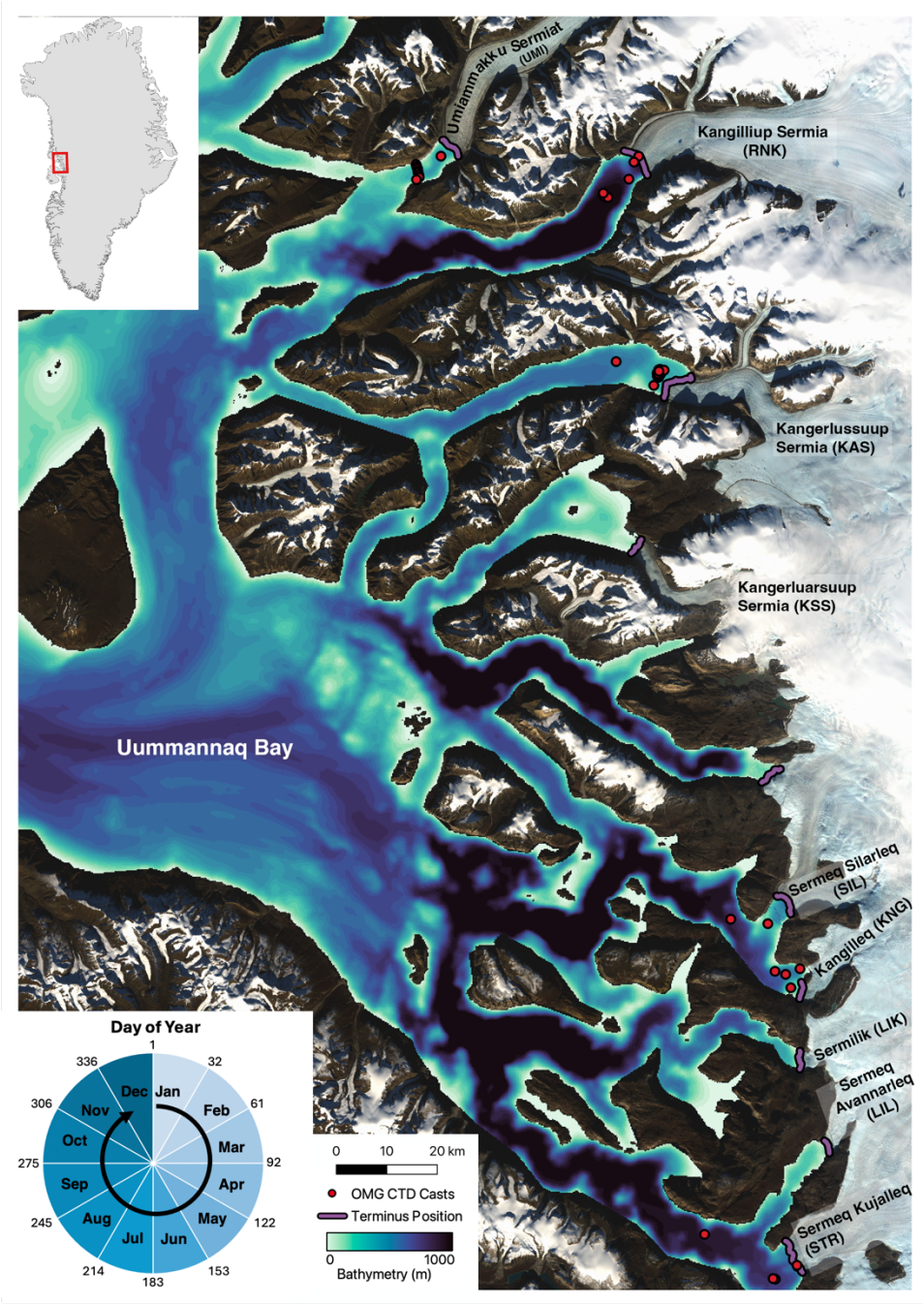

Figure 4.1 Study area map of the Uummannaq region with the inset showing the location relative to Greenland. Background imagery is from a composite of two Landsat-8 images taken on September 19 and 21, 2018. Bathymetry from BedMachine v5 is shown in the blue-green colormap. The terminus position in 2017 is shown as a purple line, and the hydrographic casts used in the plume model are shown as red dots. A day of year to month conversion calendar is shown in inset for reference

4.1.1 Physical Setting

The fjords entering Uummannaq Bay span a wide range of glacier and fjord geometries, calving styles, seasonal patterns in ice mélange presence, and fjord water conditions (Bartholomaus and others, 2016; Carroll and others, 2018; Fried and others, 2018; Catania and others, 2018; Carnahan and others, 2022), creating a natural laboratory to examine feedbacks within the glacier-mélange-ocean system (Figure 1, Table 1). Average grounding line depths and ice fluxes in our study area range from 57–528 m and 0.2–12.7 Gt/a respectively, with the largest being Kangilliup Sermia (also known as Rink Isbræ: 'RNK') with a maximum grounding line depth of 1,033 m and flux of 12.7 Gt/a, and the smallest being Sermilik ('LIK'), with a maximum grounding line depth of 88 m and flux of 0.6 Gt/a (Morlighem and others, 2017, 2022; Mankoff and others, 2020). All fjords included in this study end in Uummannaq Bay (Fig. 1), which connects to the coastal ocean waters of Baffin Bay through the ~800 m deep and ~60 km wide Uummannaq Trough (Morlighem and others, 2017, 2022). Although fed by the same trough from offshore, the water properties that reach each glacier in this region are modulated by the size and presence of local sills within their respective proglacial fjord (Figure 1).

The glaciers investigated here also exhibit a range in subglacial discharge magnitude and the neutral buoyancy depth at which the upwelling subglacial discharge plume equilibrates. Prior work in this region has shown that the more shallowly grounded glaciers have subglacial discharge plumes that equilibrate at the surface, whereas glaciers with deep grounding lines have subglacial discharge plumes that equilibrate at an intermediate depth (Carroll and others, 2016; Slater and others, 2022). When combined with prior observations of iceberg keel depths (Sulak and others, 2017) and seasonal ice mélange presence (Fried and others, 2018; Abib and others, 2024), these two regimes in plume neutral buoyancy depth correspond with differences in their

iceberg size distributions. For example, the more shallowly grounded KAS has smaller icebergs within the ice mélange (28 – 190 m on average; Sulak and others, 2017), no summertime ice mélange formation (Abib and others, 2024), and a subglacial discharge plume that equilibrates at the surface (Carroll and others, 2016; Jackson and others, 2017). Its neighboring glacier, RNK, has deeply keeled icebergs within the ice mélange (28 – 300 m; Sulak and others, 2017), often experiences short episodes of ice mélange in the summer months (Abib and others, 2024), and has a subglacial discharge plume that equilibrates at depth (120 – 220 m; Chauché and others, 2014; Carroll and others, 2016; Slater and others, 2022; Abib and others, 2024). These two different regimes of ice mélange presence, keel depth, and plume neutral buoyancy depth lead to substantially different water column stratification profiles, with more deeply grounded glaciers having cooler and fresher water at their surface (Abib and others, 2024). Detailed studies such as this, however, have only been completed at a few glaciers in the region, and are seldom validated with in situ observations due to hazardous field conditions within Greenland's ice choked fjords.

4.2 Methods

4.2.1 Ice Mélange Characteristics

4.2.1.1 Ice Mélange Presence and Absence

To create a time series of ice mélange presence and absence in our study fjords between 2013-2021, we used the Google Earth Engine Digitization Tool to visually inspect all freely available satellite imagery (GEEDiT; Lea, 2018). Between the months of February and October each year, we obtained all available cloud-free optical imagery from ASTER, Landsat 7, Landsat 8, and Sentinel 2 imagery to classify whether each fjord had either seasonal ice mélange or no ice mélange present. During the winter months, when darkness precluded the capture of optical

satellite imagery, we supplemented our time series with Synthetic Aperature Radar (SAR) backscatter products from Sentinel-1A and B to ensure we captured the formation date of seasonal ice mélange. Seasonal ice mélange was defined as present between the date that ice mélange formed in the proglacial fjord and remained attached to the terminus throughout the winter months to the date that the first cloud free image showed ice mélange detached from the glacier terminus. Using these time series, we identified the breakup and formation date of the seasonal ice mélange each year, as well as the duration of the seasonal ice mélange.

We verify our ice mélange time series by using a novel velocity processing chain most recently described in Joughin and others (2020) and Chudley and others (2023). Ice velocities over each proglacial fjord were derived every 12-days between 2015-2021 from imagery from Sentinel-1A and B. These velocities were calculated using speckle and feature tracking methods, which calculate the displacement of features in subsequent images by cross-correlating patches of the textured earth and ice surface. First, we trim the resulting ice mélange velocity mosaics to each fjord of interest and find the terminus position (Black and others, 2022) closest in time to the mosaic. We bisect our fjord mask with the relevant terminus position and select the area down-fjord from the glacier terminus as the region for potential ice mélange coverage. Ice mélange area is only defined for areas of rigid mélange, i.e., ice mélange that moves uniformly between two consecutive image pairs and can therefore be tracked with the velocity processing algorithm. We relied on both this velocity generated time series of rigid ice mélange as well as the visual analysis of ice mélange presence/absence described above to ensure we captured all instances of ice mélange in the fjord, even when not rigid.

For each of these time series, we calculate a time average as well as quantify yearly variations. This allows us to understand the typical ice mélange regime in each investigated

fjord, as well as deviations from the mean that may be caused by the varied environmental, dynamic, and geometric forcings discussed below.

4.2.1.1 Iceberg Size Distributions within the Ice Mélange

To determine the distribution of icebergs within the sea ice matrix for each study fjord, we use all available ArcticDEM strips that capture ice mélange in the Uummannaq region. Using these digital elevation models (DEMs), we calculate iceberg keel depths following the methodology from Shiggins and others (2023). In this method, the average elevation is sampled in a bounding box near the glacier terminus and is subtracted from the elevation of each pixel in the DEM to correct for local sea level variations. Then, to isolate individual icebergs, we set a threshold of 4 m and create a polygon around each iceberg. We sample the DEM within the geometry of each individual iceberg to obtain the average elevation of the iceberg, and then assume hydrostatic equilibrium to calculate the average keel depth of each iceberg. Due to our selection of 4 m as an elevation threshold, the minimum detected keel depth here will be 33 m (assuming an ice density of 917 kg/m^3 and ocean density 1028 kg/m^3). We then compile all DEM-derived data by fjord and calculate the average and maximum iceberg draft per fjord.

4.2.2 Environmental, Dynamic, and Geometric Forcings

4.2.2.1 Air Temperature

We quantify air temperature in each fjord using available single-level ERA5 daily re-analysis data between 2013-2021 (Hersbach and others, 2023). We calculate a mean air temperature for each fjord by averaging the 2-meter air temperature field over the entire surface of the fjord. We then determine a daily climatology of air temperature by compiling the values

for each calendar day throughout our time series and determining the average and standard deviation from this mean. Using these fjord-average daily temperatures, we further take the mean of all daily values in December, January, and February (DJF) in each fjord to represent the winter conditions under which seasonal ice mélange is in place.

4.2.2.2 Ocean Hydrography

To understand both the ambient ocean conditions and the near glacier fjord hydrography, we use all available Oceans Melting Greenland (OMG) shipboard CTD (conductivity-temperature-depth) and AXCTD (airborne-expendable-CTD) casts throughout the duration of our study period. We separate the casts into regions defined as the Uummannaq Trough (all available casts in the region: $-55.80° < \text{longitude} < -53.29°$, $70.58 < \text{latitude} < 71.59°$) and for each individual study fjord. Hydrographic measurements were converted to conservative temperature (CT) and absolute salinity (SA) following the Thermodynamic Equation of Seawater 2010 (TEOS-10; McDougall and Barker, 2011). We exclude data in the top 5 m of the water column, bin the data in 2 m depth intervals, and for shipboard CTD casts we isolate only the downcast. Salinity data were further de-spiked using a 5 point (10 m) median filter, and data beyond two standard deviations from the mean were removed as anomalous. To prepare ocean hydrography data for the subglacial discharge plume model, we follow the methods of Mouginot and others (2019). This involves truncating the CTD casts at the depth of the submarine sill if it is glacier-ward of the data collection site and extending the ocean conditions at the depth of the sill to the grounding line depth.

4.2.2.3 Subglacial Discharge and Ice Flux

We produce a daily time series of subglacial discharge and ice flux by identifying the flux gates and discharge outlets that correspond with our study glaciers from a pre-existing daily dataset produced for the entire Greenland Ice Sheet (Mankoff, Noël, and others, 2020; Mankoff, Solgaard, and others, 2020). We calculate a daily climatology of subglacial discharge and ice flux by taking the average and standard deviation for each calendar day throughout our study period to determine when anomalies occur in the time series. To represent the conditions under which ice mélange typically breaks up, we further took the average ice flux and subglacial discharge values for the months of June, July, and August (JJA).

4.2.2.4 Fjord Geometry

To investigate geometric forcings that could contribute to ice mélange characteristics, we quantify the grounding line depth and sill depth for each study fjord. We obtain a representative grounding line profile for each glacier by extracting BedMachine v5 at the location of the 2017 glacier terminus and forcing the ends of the profile to reach sea level (0 m). Sill depth was extracted from BedMachine v5 by manually tracing the thalweg (the deepest point in the fjord) from the terminus of each glacier to where it branches off from Uummannaq Bay. The local and absolute minimums were identified along the thalweg, and both the shallowest sill and sill closest to the terminus were identified.

4.2.3 Subglacial Plume Model

We estimate the neutral buoyancy depth of the upwelling subglacial discharge plume using a buoyant plume model (Slater and others, 2016) with a line plume geometry (Jackson and

others, 2017) for each fjord with available CTD casts in the basin. We initialize our plume model with both the yearly and overall average hydrographic profiles described above and a 250 m wide line plume (Slater and others, 2022). We run the buoyant plume model for the total range of subglacial discharge values observed in the Uummannaq region (0 – 1000 m^3/s) in 10 m^3/s increments. Using these inputs, we calculate the neutral buoyancy depth of the plume (the depth at which it equilibrates into the fjord) by finding the depth at which the density of the ambient stratification equals the density of the upwelling discharge plume. Using the observed subglacial discharge time series for each individual study fjord, we then calculate a time series of neutral buoyancy depth throughout our study period.

4.3 Results

4.3.1 Ice mélange in the Uummannaq region

4.3.1.1 Ice mélange persistence and change in time

All fjords in the Uummannaq region undergo seasonal formation and breakup of ice mélange (Table 1; Figures 2 and 3). On average, ice mélange forms on day 340 ± 36 of the year (mean ± 1 standard deviation), with the earliest formation occurring at LIL (day 316 ± 20) and the latest ice mélange formation occurring in front of RNK (day 363 ± 32). Ice mélange lasts for 201 ± 55 days in the region as a whole, with UMI having the longest seasonal duration of ice mélange (236 ± 36 days) and KNG having the shortest period of seasonal ice mélange (170 ± 33 days). Ice mélange breaks up earliest in KSS (day 152 ± 10) and latest in SIL (day 234 ± 57), with the entire region experiencing average ice mélange breakup on day 177 ± 33. We find good agreement between our optical time series and the rigidity-derived time series, with no periods of rigid ice mélange observed outside of the duration of seasonal ice mélange determined with

GEEDiT (Figure S-1). There is a transition from rigid mélange to non-rigid mélange before we see the icebergs cleared from the fjord, which corresponds with prior field observations at Sermeq Kujalleq (Cassotto and others, 2021), suggesting that the duration over which ice mélange impacts glacier dynamics directly through buttressing is shorter than the duration over which ice mélange imparts meltwater into the upper fjord layers.

There is larger variability in seasonal ice mélange breakup date than formation date across the region, with the average formation date varying 20-48 days over our record, and ice mélange breakup date varying between 8-57 days over our record on average. This suggests that interannual variations in seasonal ice mélange duration are controlled by yearly variations in the breakup date rather than the formation date, and that the date of ice mélange formation is more uniform throughout the course of our study period.

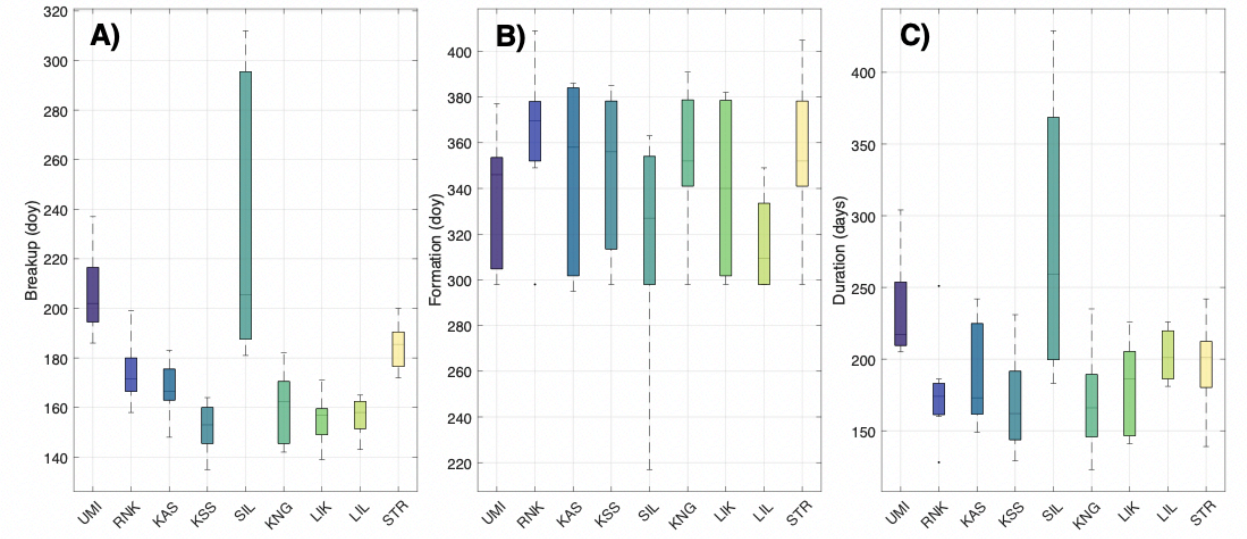

Figure 4.2 Seasonal ice mélange breakup day (A), formation day (B), and duration (C) for all study fjords. Formation date often spans across the new year, so 366 days were added to formation dates less than day 100 to enable easier interannual comparison. Boxes indicate the 25th to 75th percentile of the data, while whiskers show the full range of the data not considered outliers, which are indicated by black dots.

Throughout the time series, interannual variations in ice mélange persistence change similarly across the Uummannaq region. For example, between 2014 and 2015, all fjords exhibit a decrease in ice mélange duration from 246 ± 24 to 174 ± 26 days (Figure 3). Similarly, between 2015 and 2016 all fjords in the region experienced an increase in ice mélange duration. One glacier, SIL, is an exception as it underwent drastic change in ice mélange persistence throughout our study period. Between 2017 and 2018, SIL's seasonal ice mélange duration increased by 207 days. The average duration of seasonal ice mélange at SIL between 2013-2017 and 2018-2020 increased by 171 days (211 days to 382 days). This corresponded with a delay in average breakup date from day 190 of the year between 2013-2017 to day 278 of the year between 2018-2020 (88 days later in the year).

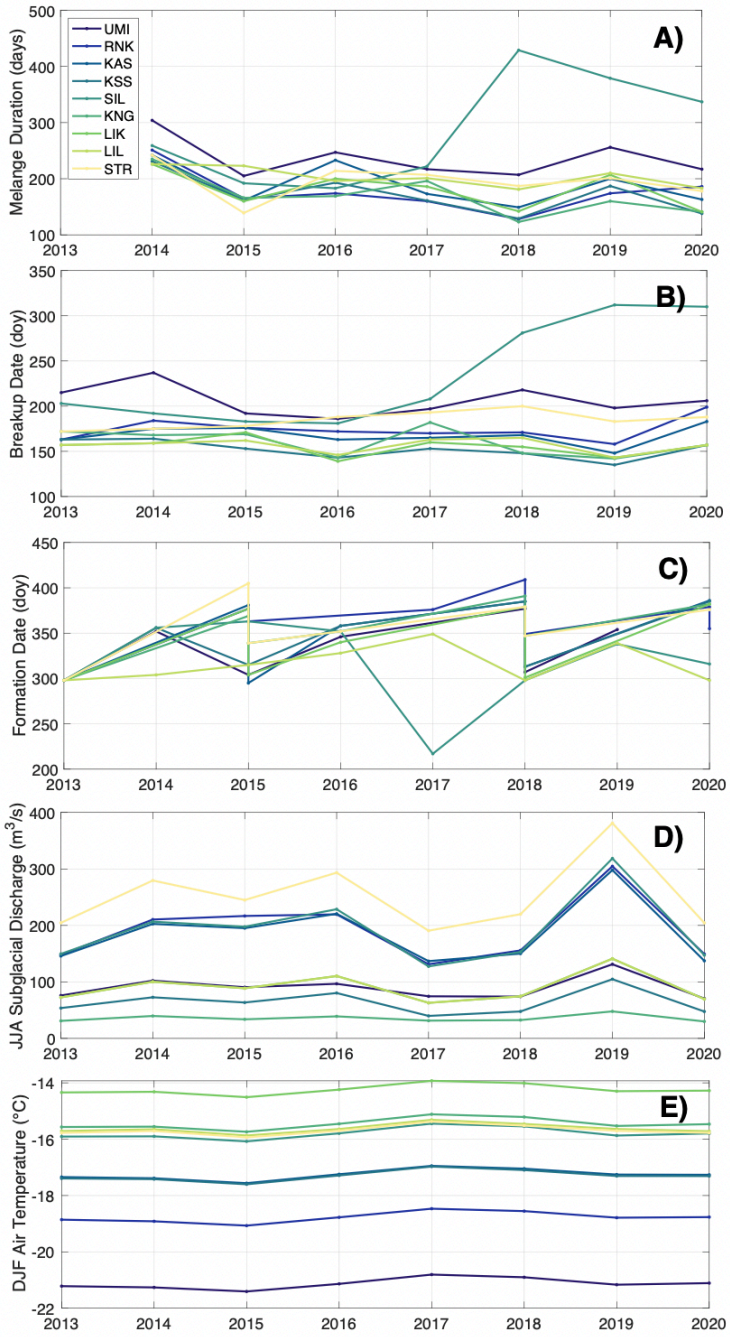

Figure 4.3 Ice mélange duration (A), breakup date (B), formation date (C), JJA average subglacial discharge (D), and DJF average air temperature (E) for each study glacier in the Uummannaq region. Formation date often spans across the new year, so 366 days were added to formation dates less than day 100 to enable easier interannual comparison. It is possible for ice mélange to undergo a seasonal cycle where it forms early in the year (doy < 100), breaks up in the summer melt season, and reforms before the start of the next year, which will appear as multiple formation dates for one calendar year in panel (C).

4.3.1.2 Ice mélange characteristics

ArcticDEM strips showing seasonal ice mélange were available and iceberg keel depths were calculated for all glaciers in the Uummannaq region except for KSS (Table 1, Figure 4). Icebergs within the ice mélange of the Uummannaq district range from 33 m (the minimum detectable depth) to 409 m, with an average keel depth of 39 ± 10 m. The largest icebergs within the sea ice matrix occur at RNK and STR, reaching depths of up to 409 m and 384 m, respectively. While these fjords have icebergs that extend several hundred of meters into the water column, 95% of the icebergs in these fjords reside in the upper 60 m of the water. Glaciers like UMI, KNG, LIK, and LIL have icebergs that only occupy the upper 150 m of the water column. Examining variations in iceberg size between each available DEM suggest that icebergs within the ice mélange tend to follow the same depth distribution year to year, with slight variations in the percentage of icebergs that occupy deeper keel depth bins.

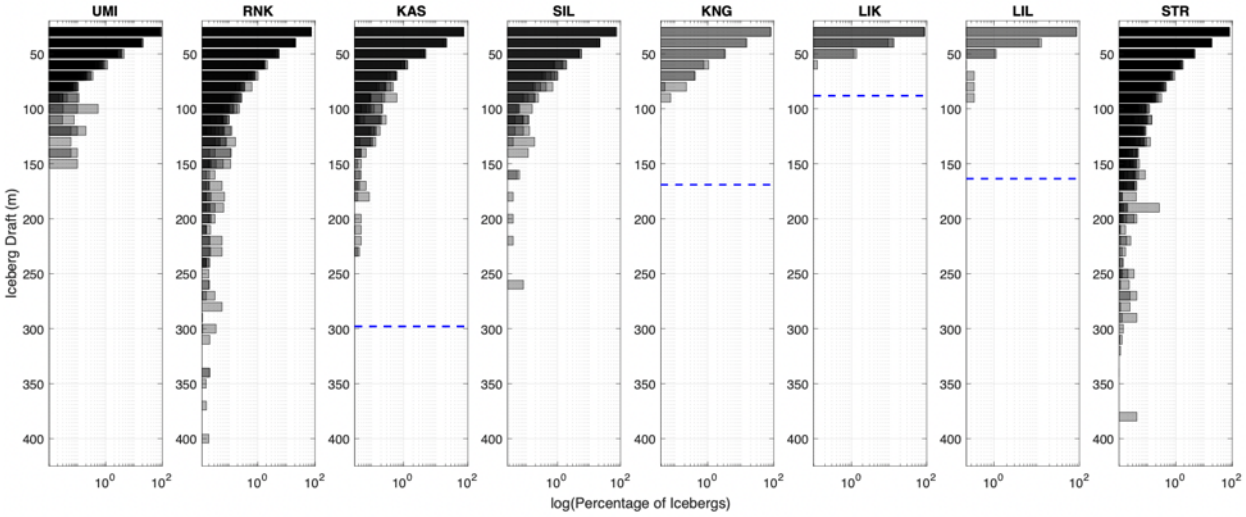

Figure 4.4. Iceberg drafts within the ice mélange for study glaciers with available ArcticDEM strips. Each grey bar indicates the distribution from one DEM, with darker shading suggesting a higher likelihood that icebergs occupy that depth bin. Blue dashed lines indicate the maximum depth of the grounding line, with the grounding line depths for UMI (496m), RNK (1,033 m), SIL (556 m), and STR (485 m) beyond the plot limits.

4.3.2 Environmental, Dynamic, and Geometric Forcings

4.3.2.1 Air Temperature

Average DJF air temperature in the Uummannaq region fjords is -17 ± 2 °C, with temperatures increasing from north (UMI: -21.1 ± 0.16 °C) to south (STR: -15.7 ± 0.15°C; Table 1, Figures 5 and S-2). Throughout the region, the air temperature rises above freezing on day 152 of the year, again following a pattern of later transition to above-freezing temperatures from the north (UMI: day 176 ± 17) to south (STR: day 143 ± 16). Two fjords are exceptions to this pattern, KNG and LIK, which both have colder average DJF temperatures (-14.3 ± 0.16 °C and -15.5 ± 0.17 °C respectively) and rise above freezing earlier in the year (day 137 ± 18 and day 134 ± 18 respectively) compared to their more southern neighbors, LIL and STR.

There is little interannual variability in mean DJF air temperature, with the biggest air temperature increase occurring between 2015 and 2017 by 0.6 °C. The lowest air temperature occurs in 2015, while all fjords reach their highest air temperature in 2017 before decreasing again until 2019 (Figure 3).

4.3.2.2 Subglacial Discharge

The magnitude of subglacial discharge in this region is more correlated with glacier flux than latitudinal location (Table 1, Figures 5 and S-3). The glaciers with the largest JJA average subglacial discharge are RNK (219 ± 70 m^3/s), KAS (209 ± 64 m^3/s), SIL (215 ± 71 m^3/s), and STR (283 ± 77 m^3/s), while KSS (74 ± 26 m^3/s) and KNG (39 ± 8 m^3/s) have relatively small average summer subglacial discharge. Despite these large differences in JJA subglacial discharge, all glaciers in this region start their subglacial discharge season (i.e., the date subglacial discharge surpasses 10% of the yearly maximum) within 17 days of each other. UMI

surpasses 10% of its annual maximum subglacial discharge value on day 152 ± 12 of the year, while KSS reaches this magnitude on day 169 ± 11 of the year.

There is high interannual variability in the JJA average subglacial discharge magnitude. For all glacial systems, subglacial discharge increases between 2013 and 2014 before stabilizing until 2016. Starting in 2016, the subglacial discharge decreases in magnitude by up to 65% for all fjords before slowly increasing again to a study maximum JJA average in 2019 (Figure 3).

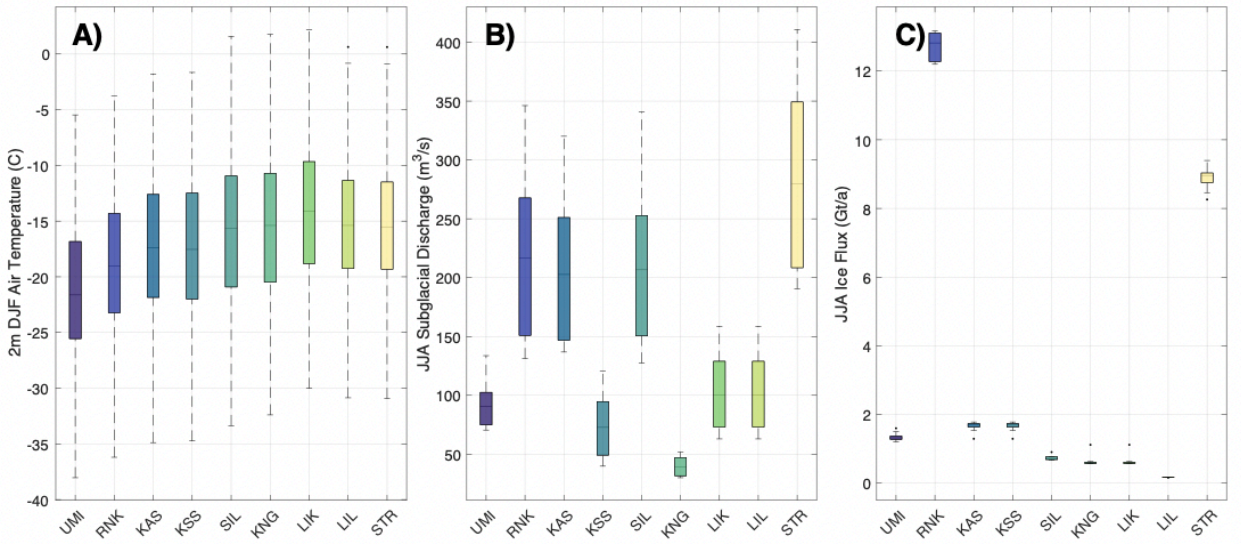

Figure 4.5. Overview of investigated environmental forcings between 2013-2021 for each study glacier: (A) DJF air temperature, (B) JJA subglacial discharge, and (C) JJA ice flux. Boxes indicate the 25th to 75th percentile of the data, while whiskers show the full range of the data not considered outliers, which are indicated by black dots.

4.3.2.3 Fjord Geometry and Ice Flux

There is large variation in grounding line depth and correspondingly ice flux throughout the Uummannaq region (Table 1, Figures 1, 5, and S-4). The largest glacier in the region is RNK, with a maximum grounding line depth of 1,033 m. RNK has an average JJA ice flux of 12.7 ± 0.4 Gt/a, which is 63 times larger than the ice flux at the smallest glacier in the region, LIL (maximum grounding line depth of 164 m). STR is the second largest outlet glacier in the region,

with an ice flux that is 30% smaller than RNK (8.9 ± 0.32 Gt/a) and maximum grounding line depth of 485 m. LIK and KNG are similar in size to LIL, each with an ice flux that is 3 times larger than at LIL (0.6 ± 0.16 Gt/a) and maximum grounding lines that are 88 m and 169 m deep respectively.

All glaciers in the region have sills present between their grounding line and Uummannaq Bay that prevent the direct advection of the warmest ambient ocean waters from reaching the glacier terminus (Table 1, Figure S-5). All sills in the region are shallower than 530 m, which is the depth of the sill at STR at a distance of 90 km from the glacier terminus. The shallowest sills are present in front of KSS and LIL, which are within 5 km of their glacier terminus and at depths shallower than 150 m. While RNK and SIL have grounding line depths that are deeper than STR, their sill depths are shallower, with a depth of 457 m and 289 m respectively at distances of 55 km and 4.4 km from the glacier termini.

4.3.2.4 Ocean Hydrography and Plume Modeling

Seven out of the nine fjords in our study region had hydrographic data available between their proglacial sill and the terminus (Table 1; Figures 6 and S-6). For these seven fjords, the average temperature at the grounding line depth was 1.7 °C, with the warmest waters reaching the grounding line depth of RNK (2.46 °C) and STR (2.07 °C). The coldest waters were present at LIL (0.88 °C) as expected given its shallower grounding line depth.

Plume neutral buoyancy is determined based on fjord stratification and magnitude of subglacial discharge. At KAS, KNG, and LIL, the plume reached neutral buoyancy within the upper 50 m of the water column at the average summer subglacial discharge value (Table 1;

Figures 6 and S-7). At UMI, RNK, SIL, and STR, the respective subglacial discharge plumes equilibrated beneath the surface of the fjord, at depths between 77 m (STR) and 122 m (RNK).

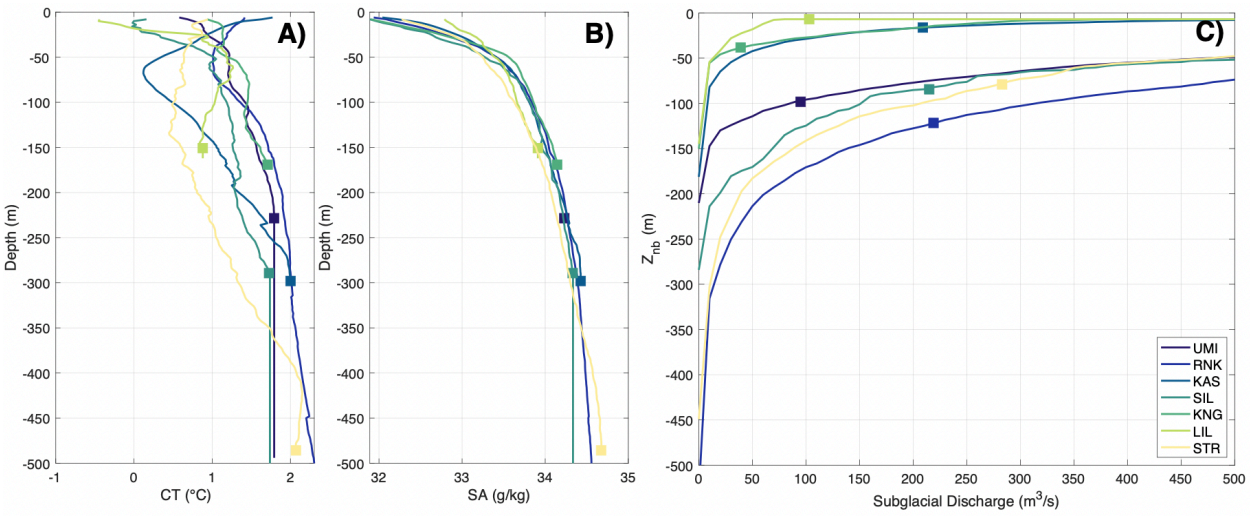

Figure 4.6. Overview of plume modeling inputs and outputs, with the conservative temperature (A) and absolute salinity (B) shown with the effective depth of the fjord indicated as a square marker. The effective depth for RNK is beyond the plot limit at 703 m. The derived plume neutral buoyancy depth (Znb) for tested values of subglacial discharge is shown (C) with the neural buoyancy depth that corresponds with the average JJA subglacial discharge value shown as a square marker.

Notably, the temperature of the ambient ocean waters entering Uummannaq Bay through Uummannaq Trough decreases over the study period (Figures 9 and S-8). In 2015, the average temperature at 300 m depth is 2.4 ± 0.29 °C. This temperature steadily decreases until 2019, when the average ocean temperature at depth is 1.1 ± 0.1 °C, before slightly increasing again to 1.8 ± 0.2 °C in 2020.

4.4 Discussion

The dataset produced here shows how ice mélange presence in Central West Greenland varies strongly over interannual time periods, depending on iceberg distributions, environmental

conditions, and glacier geometry. Below, we discuss these controls on ice mélange presence in turn, showing that the spatiotemporal patterns in ice mélange duration are largely driven by the processes that control ice mélange breakup, specifically subglacial discharge-driven modification of fjord waters. Finally, we discuss these implications with a case study at Sermeq Silarleq ('SIL'), where the combination of basin wide ocean cooling, decreased subglacial discharge, and a glacial sill led to enhanced ice mélange presence.

4.4.1 Iceberg keel depth varies with glacier geometry

The distribution of icebergs within the ice mélange matrix in the Uummannaq region varies with the geometry of the source glaciers. Glaciers within the Uummannaq region have previously been shown to vary in their calving style based on their size, with glaciers with shallower grounding lines such as UMI, KAS, KSS, KNG, LIK, and LIL calving via serac failure and larger glaciers like RNK, SIL, and STR exhibiting full thickness calving events (Fried and others, 2018). Icebergs that calve via serac failure will have shallower keel depths than icebergs that originate from full thickness calving events, which often remain mostly intact after being calved. While our results agree that icebergs calved via serac failure have shallower keel depths than those produced from full thickness calving events, we find that within the category of glaciers that calve via serac failure, there is additional variation in the iceberg keel depth.

Icebergs produced from the shallowest glaciers in the region (KNG, LIK, LIL) all have grounding lines < 200 m with keel depths <100 m in the water column (Table 1; Figure 4). While UMI and KAS calve via serac failure, they have deeper grounding lines (UMI: 496 m; KAS: 298 m) and icebergs that can extend up to 150 m and 250 m deep on average. The deepest glaciers, RNK, SIL, and STR all have icebergs that extend beyond 250 m in the water column. Our work

agrees with prior findings that while small icebergs account for an overwhelming majority of icebergs within the ice mélange matrix, attention must be paid to these deeply keeled icebergs as they account for most of the volume within the ice mélange and are more important for buttressing glacier termini and acting as freshwater sources in the water column (Enderlin and others, 2016, 2018; Sulak and others, 2017; Shiggins and others, 2023).

The variation in keel depths within the ice mélange matrix has implications for both glacier and fjord dynamics. The presence of thicker icebergs within the sea ice matrix results in a higher ability for the ice mélange to buttress and potentially stabilize the glacier terminus (Amundson and others, 2010), with recent numerical modeling work showing that a two-fold increase in ice mélange thickness will result in a quadrupling of backstress being applied to the terminus (Amundson and others, 2024). In addition to buttressing the glacier terminus, icebergs with keel depths that extend beneath their entrance sill have been shown to recirculate their cool and fresh meltwater throughout the summer season, resulting in a net cooling effect throughout the fjord (Davison and others, 2022; Hager and others, 2024). Understanding the distribution of keel depths within the ice mélange matrix therefore is key to better quantifying the potential for ice mélange to interact with glacier termini both directly through mechanically processes and indirectly through modification of the underlying fjord waters.

4.4.2 Ice mélange duration depends primarily on ice mélange breakup processes

All glaciers in the Uummannaq district undergo seasonal formation and breakup of ice mélange. Our results suggest that there is more variability in the date of ice mélange breakup rather than the date of formation, suggesting interannual changes in ice mélange duration are controlled by breakup processes (Table 1; Figure 3). We define two indices, the T2M Index and

the Runoff Index, to investigate breakup processes that would melt the ice mélange subaerially and subaqueously. The T2M Index is the difference in days between ice mélange breakup date and the date that the fjord average air temperature rises above 0 °C, with a negative T2M Index indicating that the air temperature rises above 0 °C before ice mélange breaks up. The Runoff Index is the difference in days between a glacier's subglacial discharge system turning on (reaching a value at least 10% of the annual maximum discharge) and the ice mélange breakup date, with negative values indicating subglacial discharge turns on before the seasonal ice mélange breakup date.

The seasonal ice mélange breakup does not occur until after its fjord average air temperature rises above 0 °C for all glaciers except KSS (i.e., all glaciers have a negative T2M Index except KSS; Figure 7). In contrast, there is a split in behavior as to whether ice mélange breaks up before or after subglacial discharge turns on in the glacial system (i.e., there is a mix of positive and negative Runoff Indices; Figure 7). On average, shallowly grounded glaciers (< 200 m) break up before the subglacial discharge in the system turns on (i.e., Positive Runoff Index, average of 8.5 days). This suggests that changes in the underlying fjord conditions have little impact on the seasonal breakup of ice mélange at shallowly grounded glaciers such as KSS, KNG, LIK, and LIL. Glaciers with deeper grounding lines, however, have seasonal ice mélange that does not break up until well after subglacial discharge begins (33 days on average for grounding lines deeper than 200 m), suggesting a possible dependence of seasonal ice mélange breakup on ocean currents and temperature at these larger outlet glaciers. At all glaciers in the Uummannaq district, seasonal ice mélange re-forms after the air temperature drops beneath 0 °C and subglacial discharge has become effectively 0 m^3/s.

Prior work in the Uummannaq region did not find ice mélange breakup date to be correlated with air temperature (Howat and others, 2010), although air temperature was indicated as an important factor for ice mélange breakup at LeConte Glacier (Amundson and others, 2020) and Sermeq Kujalleq (Cassotto and others, 2015). Howat and others (2010), however did find that ice mélange breakup date was highly correlated with May sea surface temperature in the Uummannaq region. Interannual variations in environmental forcings in this region show variations in ice mélange breakup date that vary with the magnitude of subglacial discharge (Figure 3). For example, there is an earlier breakup date of seasonal ice mélange in 2016 that corresponds with an increase in subglacial discharge that year. After 2016, however, the magnitude of subglacial discharge in all fjords begins to decrease, corresponding with a delay in ice mélange breakup date until 2019 when subglacial discharge increases again (Figure 3). Subglacial discharge influences ice mélange through both mechanical forcing on the underside of the icebergs (Amundson and others, 2020; Hughes, 2022), as well as providing a pathway for warm, glacially modified water to melt the icebergs from below (Davison and others, 2020). We further investigate oceanic controls on ice mélange breakup by examining the evolution of the subglacial discharge plume throughout the year in the following section.

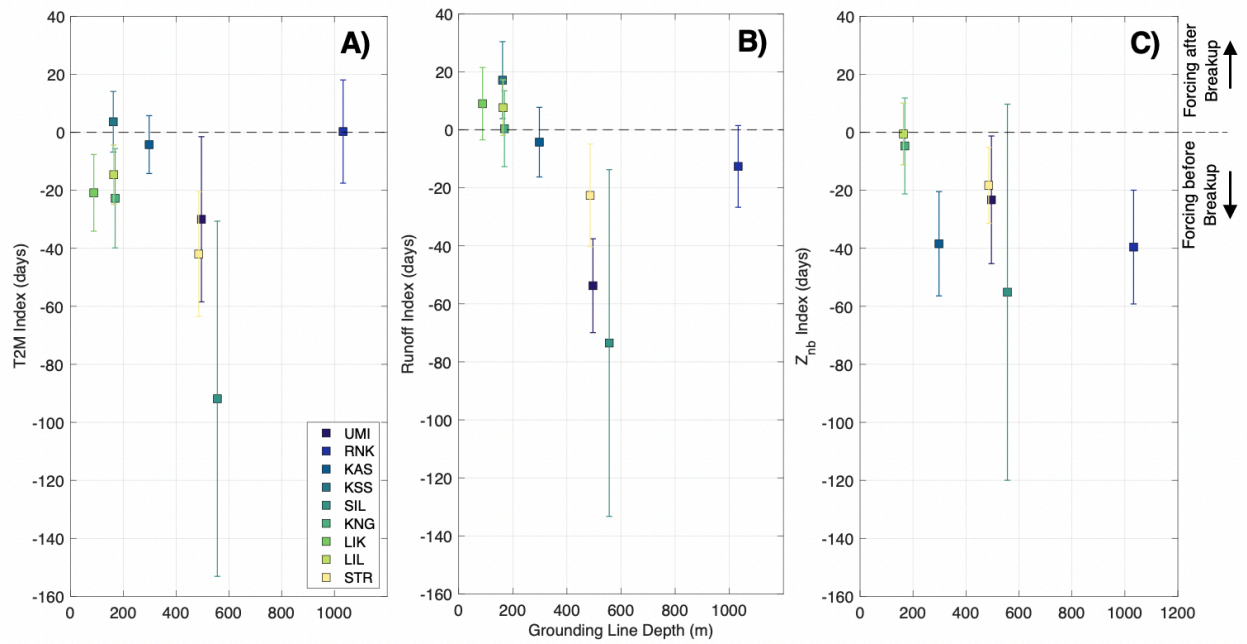

Figure 4.7. T2M (A), Runoff (B), and Neutral Buoyancy Depth (C) index for each fjord studied in the Uummannaq region against maximum grounding line depth, with square markers indicating the average over the study period and error bars indicating ± 1 standard deviation. T2M index (A) is the number of days between air temperatures rising above 0 °C and ice mélange breakup, while runoff index and Znb indices are the number of days between subglacial discharge start (B) or the plume reaching the mean iceberg keel depth (C) and ice mélange breakup. Z_{nb} was only calculated for the 7 glaciers with hydrographic data within their fjords.

4.4.3 Subglacial discharge drives ice mélange breakup at deeply grounded glaciers

Marine terminating outlet glaciers in the Uummannaq region with grounding line depths deeper than 200 m do not undergo seasonal ice mélange breakup until on average 33 days after subglacial discharge for the glacial system turns on (Figure 7). Iceberg keel depths are on average deeper for these fjords with deep grounding lines (Figure 4). This suggests that the breakup of seasonal ice mélange in fjords with deep grounding line depths and iceberg keel depths that extend further into the water column within the sea ice matrix is dependent on processes occurring in the underlying fjord waters.

One such process that modifies the water column upon which the seasonal ice mélange floats is the subglacial discharge-driven renewal of fjord waters. In addition to having icebergs that extend deeper in the water column at these glaciers with deeper grounding lines, the subglacial discharge plumes that originate at these grounding line depths also equilibrate to neutral buoyancy at an intermediate depth in the proglacial fjord (Figure 6). Plume modeling results show that the glaciers that on average undergo seasonal ice mélange breakup after subglacial discharge begins (i.e., UMI, RNK, SIL, and STR) have subglacial discharge plumes that equilibrate and outflow in the water column at a depth of 77 – 122 m during their mean summer subglacial discharge magnitude (Figures 6 and 7). These same fjords have 95% of the icebergs within the ice mélange matrix between keel depths of 33 – 60 m (Figure 4). By comparing our time series of plume neutral buoyancy depth to the keel depth of the majority of the icebergs, we see that ice mélange breakup date is typically correlated with the date at which the plume reaches a neutral buoyancy depth equivalent to the average iceberg keel depth (Figures 7 and 8).

We further define a Z_{nb} Index, which is the difference in days between the subglacial discharge plume first reaching the average iceberg keel depth and the date of seasonal ice mélange breakup, with negative values indicating ice mélange breakup does not occur until after the plume reaches the iceberg keel depth (Figure 7). We see that for the most shallowly grounded glaciers (KNG and LIL), ice mélange breakup date occurs equally as likely before or after the plume reaches the average iceberg keel depth (Figures 7 and 8). However, for the more deeply grounded glaciers, ice mélange does not break up until after the plume has reached a neutral buoyancy depth equivalent to the average iceberg keel depth (i.e., a negative Z_{nb} Index; Figure 7).

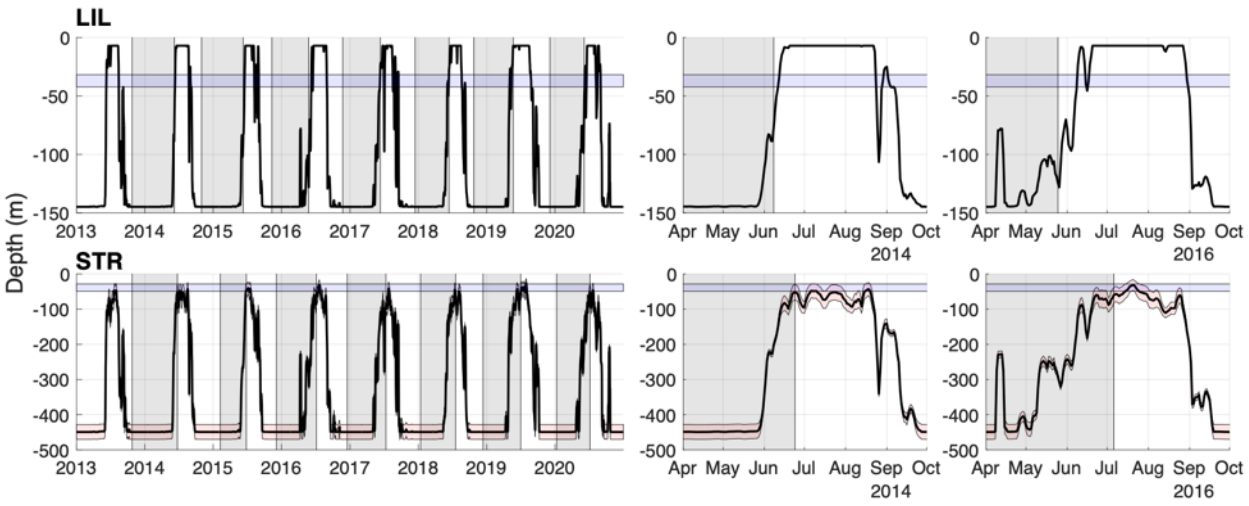

Figure 4.8. Example of time series of plume neutral buoyancy depth (black lines with red shading for +/- 1 standard deviation) for LIL (top) and STR (bottom) overlaid on seasonal ice mélange presence/absence data (grey shading, with grey indicating seasonal ice mélange is present) and the average iceberg keel depth within the ice mélange (blue shading) for the entire study period (left) and two annual subsections (middle and right). A figure with all glaciers represented is shown in the supplement (Figure S-9).

The depth at which the subglacial discharge plume reaches neutral buoyancy is determined by the stratification of the fjord water and the magnitude of subglacial discharge. Thus, in years with a more stratified water column or anomalously low subglacial discharge, the plumes could either equilibrate lower in the water column or take longer to reach the average keel depth of icebergs within the ice mélange. At the glaciers with deep grounding line depths such as UMI, RNK, SIL, and STR, such a delay would result in later ice mélange breakup dates and therefore a longer duration of seasonal ice mélange. The converse would also be true, whereby anomalously high magnitudes of subglacial discharge or a less stratified water column would lead to a subglacial discharge plume that equilibrates higher in the water column and correspond with an earlier date of seasonal ice mélange removal.

The correlation between seasonal ice mélange breakup date and subglacial discharge driven fjord removal has implications for the predicted future warming scenarios across the

Greenland ice Sheet. These scenarios expect higher rates of subglacial discharge to enter the glacial fjords due to enhanced atmospheric-driven surface ablation from a warming climate (Slater and others, 2020). These predicted larger magnitudes of subglacial discharge would result in a subglacial discharge plume that equilibrates higher in the water column and more quickly reaches iceberg keel depths, resulting in earlier breakup dates of the seasonal ice mélange. This earlier breakup date has broad implications throughout the glacier-mélange-ocean system. The earlier breakup of seasonal ice mélange would result in a shorter time over which buttressing stress could be applied to the glacier terminus, increasing the length of time that a glacier is prone to uninhibited calving activity and retreat. In addition, the reduction of residence time of icebergs in the fjord due to earlier disbursement of the seasonal ice mélange would reduce its impact on fjord stratification. This would lead to a less stratified water column, with warmer and more saline surface water properties, which would further alter the subglacial discharge plume evolution, resulting in a positive feedback loop.

4.4.4 Case Study: Basin wide ocean cooling leads to a change in ice mélange regime

To illustrate an example of the processes discussed above, we describe in detail the feedbacks within the glacier-mélange-ocean system at SIL, a deeply grounded glacier in the middle of the Uummannaq region (Figure 1). At the beginning of our data record, ice mélange forms and dissipates in this fjord around the same time each year (breakup on day 192 ± 10, formation on 339 ± 36, duration of 226 ± 47 days; Figure 9). Between 2016 and 2018, however, the duration of ice mélange increased from 183 to 429 days and remained above the 2016 average throughout our study period (Figure 3). The increase in duration is due to a delay in ice mélange breakup date from day 192 to day 258 on average between these two time periods

(Figures 3 and 9). This change in ice mélange regime corresponds with the cooling of ambient ocean waters entering Uummannaq Bay through Uummannaq trough, as well as a reduction in the magnitude of subglacial discharge (Figures 3 and 9). This cooling in ambient ocean temperature parallels the signal in Disko Bay (Khazendar and others, 2019; Joughin and others, 2020), which is fed by the same ocean currents as Uummannaq Bay (Carroll and others, 2018). These previous studies suggested that the reduction in ambient water temperature led to the prolonging of the rigid ice mélange in front of Sermeq Kujalleq, similar to the phenomenon observed here. The impact of decreased subglacial discharge, however, was not discussed in the case of Sermeq Kujalleq, where it similarly was reduced between 2016-2019.

The cooling of the ambient ocean waters entering Uummannaq Bay and the proglacial fjord of SIL when combined with a reduction in subglacial discharge entering the fjord at the grounding line would result in overall cooler glacier-adjacent water column properties and a subglacial discharge plume that takes longer to reach a neutral buoyancy depth that corresponds with the average iceberg keel depth. Overall, this transition in fjord conditions after 2016 would result in a longer residence time of seasonal ice mélange in the proglacial fjord of SIL.

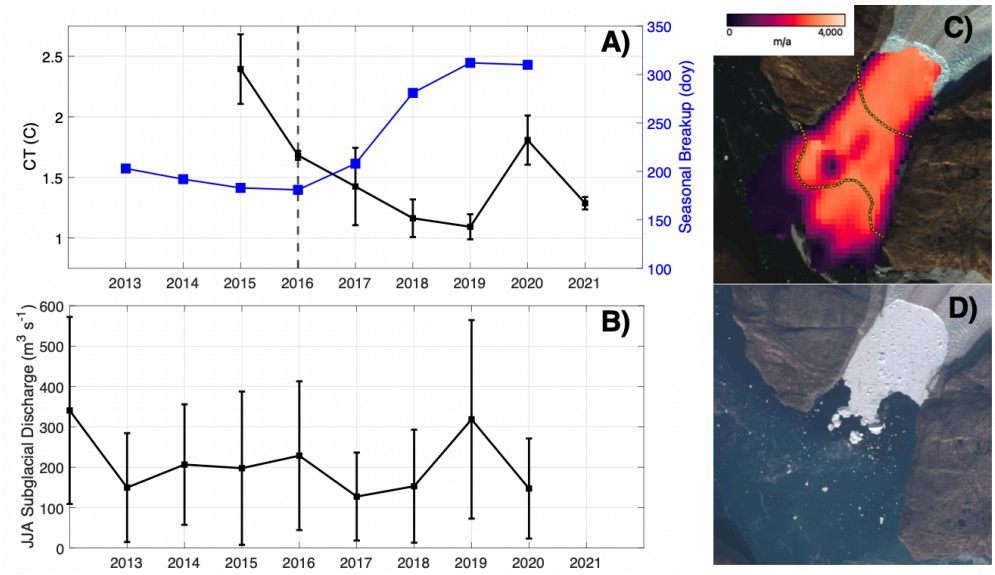

Figure 4.9. (A) Summer ocean temperature at 250 m in the Uummannaq trough with ± 1 standard deviation indicated superimposed with ice mélange breakup day at SIL. Summer temperature was determined as the average temperature between 240 – 260 m for all available OMG shipboard CTD and AXCTD casts in the trough. (B) Mean JJA subglacial discharge with ± 1 standard deviation indicated by error bars. (C) Ice mélange velocities from April 16, 2020 with lateral boundaries of the sill superimposed (yellow dotted line) as defined by a 500 m deep isobath. (D) Sentinel 2 image from August 25, 2019, showing compressive arches between mid-fjord grounded icebergs and fjord walls.

In addition to ocean-driven changes in ice mélange behavior after 2016, feedbacks between fjord geometry and ice mélange presence work together to extend the residence time of seasonal ice mélange in SIL's proglacial fjord. SIL has a submarine sill that is 289 m deep at a location 4.4 km from the glacier terminus (Figure S-5). Optical satellite imagery and available ArcticDEM strips show that deeply keeled icebergs often become grounded on the sill in front of SIL (Figure 9). Inspection of the ice mélange velocities in the proglacial fjord during these time periods of iceberg grounding show that individual icebergs within the ice mélange slow down at the location of the proglacial sill and that there is a resulting slowing of smaller icebergs surrounding these deeply grounded icebergs (Figure 9). This suggests that the sill-grounded icebergs act as additional temporary pinning points for ice mélange in the proglacial fjord,

stabilizing the surrounding icebergs and extending the duration of seasonal ice mélange. In fact, the presence of grounded icebergs on the shallow sill allows the extended ice mélange duration to persist beyond 2019, when subglacial discharge and ambient ocean temperatures began to increase again.

Overall, the combination of cool ambient ocean temperatures and low subglacial discharge likely led to cooler glacier-adjacent water properties with an outflowing glacially modified plume that equilibrates more deeply in the water column, promoting the formation of a more rigid and expansive ice mélange. As SIL is a glacier with a deep grounding line, the seasonal ice mélange at this glacier has deeply keeled icebergs within it, which often ground on the fjord entrance sill and act as additional pinning points in the fjord, further stabilizing the extended seasonal ice mélange in the fjord. Overall, this combination of interannual ocean change, low subglacial discharge, and shallow fjord geometry led to a change in the ice mélange regime in front of SIL. The increased residence time of the ice mélange in front of SIL would lead to a more pronounced impact of ice mélange melt on fjord water properties and presence on glacier terminus stresses. While this is only one example of feedbacks within the glacier-mélange-ocean system, it is possible that similar instances could take place at grounded glaciers elsewhere that undergo rapid retreat, leaving a shallow sill near their glacier terminus, or that retreat into a narrow fjord (such as in Chudley and others, 2023). In addition, the influence of subglacial discharge on ice mélange should be considered for the case of Sermeq Kujalleq, where similar decreases in magnitude were observed between 2016-2019 and coincided with the increase in ice mélange rigidity and terminus advance (Khazendar and others, 2019; Joughin and others, 2020).

4.5 Conclusions

Detailed studies of ice mélange have only been done at a few of the large outlet glaciers in Greenland with permanent ice mélange, although recent work has suggested that even short-lived ice mélange can have implications for the glacier-mélange-ocean system. Here we show that ice mélange physical characteristics correspond with the size of their source glacier, with deeply grounded glaciers producing ice mélange that extends deeper in the water column and having a higher potential for influencing glacier dynamics and fjord stratification. We find that while all glaciers in the Uummannaq region undergo seasonal ice mélange formation and breakup, only the ice mélange at glaciers with deep grounding lines are dependent on ocean processes to control this seasonal cycle. While all glaciers in the region undergo seasonal ice mélange breakup only after the air temperature rises above freezing, breakup does not occur at glaciers with deep grounding lines until after the subglacial discharge plume reaches a neutral buoyancy depth equivalent to the mean keel depth of the ice mélange matrix. This suggests that processes that control subglacial plume evolution, such as ambient ocean stratification and magnitude of subglacial discharge, can lead to changes in the duration of seasonal ice mélange at deeply grounded glaciers. We highlight this process with an example at Sermeq Silarleq ('SIL'), where a shift to cooler ocean temperatures entering the fjord combine with anomalously low subglacial discharge and fjord bathymetry promote extended ice mélange. While this example resulted in a more expansive ice mélange, we also discuss how long-term climatic trends that will lead to enhanced surface ablation of ice sheets could result in earlier dissolution of ice mélange at deeply grounded glaciers around Greenland. The feedbacks within the glacier-mélange-ocean system that lead to changes in seasonal ice mélange duration will have implications for the evolution of glacier termini through both changes to buttressing and

submarine melting. Therefore, obtaining a more detailed understanding of the physical processes that contribute to ice mélange duration at these glacial systems with deep grounding lines is essential for constraining the long-term change of the Greenland Ice Sheet and its freshwater export.

Table 4.1. Summary of environmental, geometric, and dynamic forcings presented in manuscript. The grounding line depth is taken at the location of the 2017 glacier terminus. Values for ice flux and subglacial discharge are the JJA average, while air temperature is the DJF average. Plume neutral buoyancy presented here is for the JJA average value of subglacial discharge.

Glacier	Mélange Formation /Breakup /Duration (day of year)	Avg. Iceberg Keel Depth [max] (m)	Grounding Line Depth [max] (m)	Sill Depth [Distance from Terminus] (m [km])	Ice Flux (Gt/a)	Subglacial Discharge [start date] (m^3/s [day of year])	Plume Neutral Buoyancy (m)	Ocean Temperature at Grounding Line (°C)	Air Temperature [start date] (°C [day of year])
UMI	334 ± 31 206 ± 17 236 ± 36	37 ± 5 [153]	197 ± 125 [496]	228 [11.9]	1.30 ± 0.1	95 ± 23 [152 ± 12]	97	1.79	-21.1 ± 0.16 [176 ± 17]
RNK	363 ± 32 174 ± 13 177 ± 37	39 ± 11 [409]	528 ± 326 [1033]	457 [55.3]	12.7 ± 0.4	219 ± 70 [161 ± 10]	122	2.46	-18.8 ± 0.16 [174 ± 15]
KAS	345 ± 42 168 ± 11 189 ± 37	39 ± 10 [233]	196 ± 95 [298]	382 [62.0]	1.70 ± 0.1	209 ± 64 [163 ± 11]	17	1.55	-17.3 ± 0.16 [163 ± 11]
KSS	344 ± 36 152 ± 10 172 ± 35	-	79 ± 43 [162]	86 [3.14]	1.70 ± 0.1	74 ± 26 [169 ± 11]	-	-	-17.3 ± 0.16 [156 ± 12]
SIL	317 ± 48 234 ± 57 286 ± 97	40 ± 10 [265]	358 ± 171 [556]	289 [4.41]	0.70 ± 0.1	215 ± 71 [160 ± 7]	82	1.74	-15.8 ± 0.17 [142 ± 11]
KNG	354 ± 31 160 ± 15 170 ± 37	38 ± 7 [143]	72 ± 60 [169]	503 [44.3]	0.60 ± 0.2	39 ± 8 [160 ± 18]	38	1.71	-15.5 ± 0.17 [137 ± 18]
LIK	340 ± 39 155 ± 10 180 ± 33	36 ± 4 [70]	57 ± 26 [88]	320 [6.65]	0.60 ± 0.2	103 ± 32 [164 ± 12]	-	-	-14.3 ± 0.16 [134 ± 18]
LIL	316 ± 20 157 ± 8 203 ± 18	37 ± 5 [95]	85 ± 61 [164]	151 [1.24]	0.20 ± 0.01	103 ± 32 [164 ± 12]	7	0.88	-15.6 ± 0.15 [142 ± 15]
STR	357 ± 34 185 ± 9 195 ± 32	39 ± 11 [384]	275 ± 133 [485]	629 [90.1]	8.90 ± 0.3	283 ± 77 [162 ± 14]	77	2.07	-15.7 ± 0.15 [143 ± 16]

CHAPTER V
CONCLUSIONS

Mass loss from tidewater glaciers and ice sheets has increased in recent decades, yet there still remains large uncertainty in the rate and magnitude of sea level rise that these systems will contribute in the future. A large portion of this uncertainty is due to unvalidated parameterizations at the ice-ocean interface where hazardous conditions prohibit easy field measurements. Currently, up to 50% of ice lost from the Greenland Ice Sheet and 100% from Antarctic Ice Sheets is due to frontal ablation at glacier termini, or the combination of iceberg calving and submarine melting. In this dissertation, I investigate the relationship between glacier frontal ablation, terminus morphology, and fjord-scale circulation in order to better understand the processes that impact tidewater glacier evolution. I use both field and remotely sensed observations to show that tidewater glaciers are capable of supporting significantly overcut terminus geometry, which directly contradicts current submarine melt parameterizations and suggests that essential feedbacks within the glacial fjord system are missing from our current theory of glacier change. I then examine a particularly understudied feedback in glacial fjords, the input of meltwater from ice mélange at the fjord surface, to show that this additional buoyancy source can modify the water column down to the depth of the outflowing subglacial plume and should be considered in coupled glacier-ocean models. Finally, I expand this analysis to a suite of several fjords to show that important feedbacks exist between ice mélange presence and subglacial discharge plume evolution that could impact ice mélange duration under future climate warmings scenarios.

In Chapter II, I use a novel concurrent dataset of tidewater glacier submarine morphology and environmental conditions to show that the glacier terminus is predominately overcut despite high rates of submarine melting. I show that while periods of high subglacial discharge lead to

localized undercutting near the subglacial discharge outlet as theory predicts, the glacier terminus overall maintains an overcut morphology. This directly challenges the assumption that tidewater glacier termini are largely undercut and shows that current submarine melt rate theory does not accurately predict tidewater glacier evolution.

In Chapter III, I transition from the glacier terminus to the glacial fjord in order to investigate one process that is currently poorly understood in fjord dynamics – the role that ice mélange meltwater plays on stratification of the water column and what this means for glacier submarine melting. I find that even short-lived ice mélange events can cause significant cooling and freshening of the water column, altering the stratification of the fjord down to the depth of the outflowing subglacial discharge plume. I compare these observations to an adjacent fjord, where ice mélange seldom forms, to show that the addition of meltwater into the upper layers of the fjord from ice mélange creates fundamental differences in the upper layer hydrography that should be considered when modeling glacier-ocean systems.

I expand upon Chapter III in Chapter IV by investigating ice mélange in a suite of 9 fjords in Central West Greenland to characterize the conditions that lead to ice mélange formation and dissolution and the resulting implications for tidewater glacier evolution. I find that while all tidewater glaciers in this region undergo seasonal formation and dissolution of ice mélange, the large glaciers with deep grounding lines have an ice mélange breakup date that corresponds with the evolution of the subglacial discharge plume. I use a case study from a large outlet glacier to discuss how interannual changes in the magnitude of subglacial discharge and ambient ocean temperature contribute to changes in the neutral buoyancy depth of the plume and lead to an increase in duration of seasonal ice mélange in this fjord while these conditions are present. I explore the implications of this under predicted future climate change, whereby

enhanced air temperatures will lead to increased magnitudes of subglacial discharge and therefore a shorter ice mélange season in fjords with deep grounding lines where ice mélange breakup is controlled by subglacial discharge plume dynamics.

Overall, this dissertation finds that current submarine melt theory does not accurately predict the evolution of the submarine terminus at tidewater glaciers and explores the role that ice mélange meltwater can play on modifying glacier adjacent water properties. We use observational data to show that the submarine terminus of a tidewater glacier is predominately overcut across several seasons, despite high submarine melt rates, which directly contradicts current melt rate theory. We then explore a currently misunderstood process in the glacial fjord system, ice mélange meltwater, to show that even short-lived ice mélange events can significantly alter the water column and cause changes to buoyancy-driven circulation the proglacial fjord. We finally expand this analysis to several glacial fjords in Central West Greenland to show that the duration of ice mélange presence is directly linked to interannual ocean and glacier change, with future atmospheric warming leading to a reduction in the duration of ice mélange present in proglacial fjords. A reduction in ice mélange duration will lead to less time over which the ice mélange can input cool and freshwater in the glacier-adjacent waters, thereby increasing the length of time that warm ambient water is available to melt the glacier terminus and contribute to frontal ablation.

APPENDIX A

CHAPTER II: ADDITIONAL INFORMATION ON ICE VELOCITY AND ENVIRONMENTAL CONDITIONS AT LECONTE GLACIER

A.1 Ice Velocity and Environmental Conditions

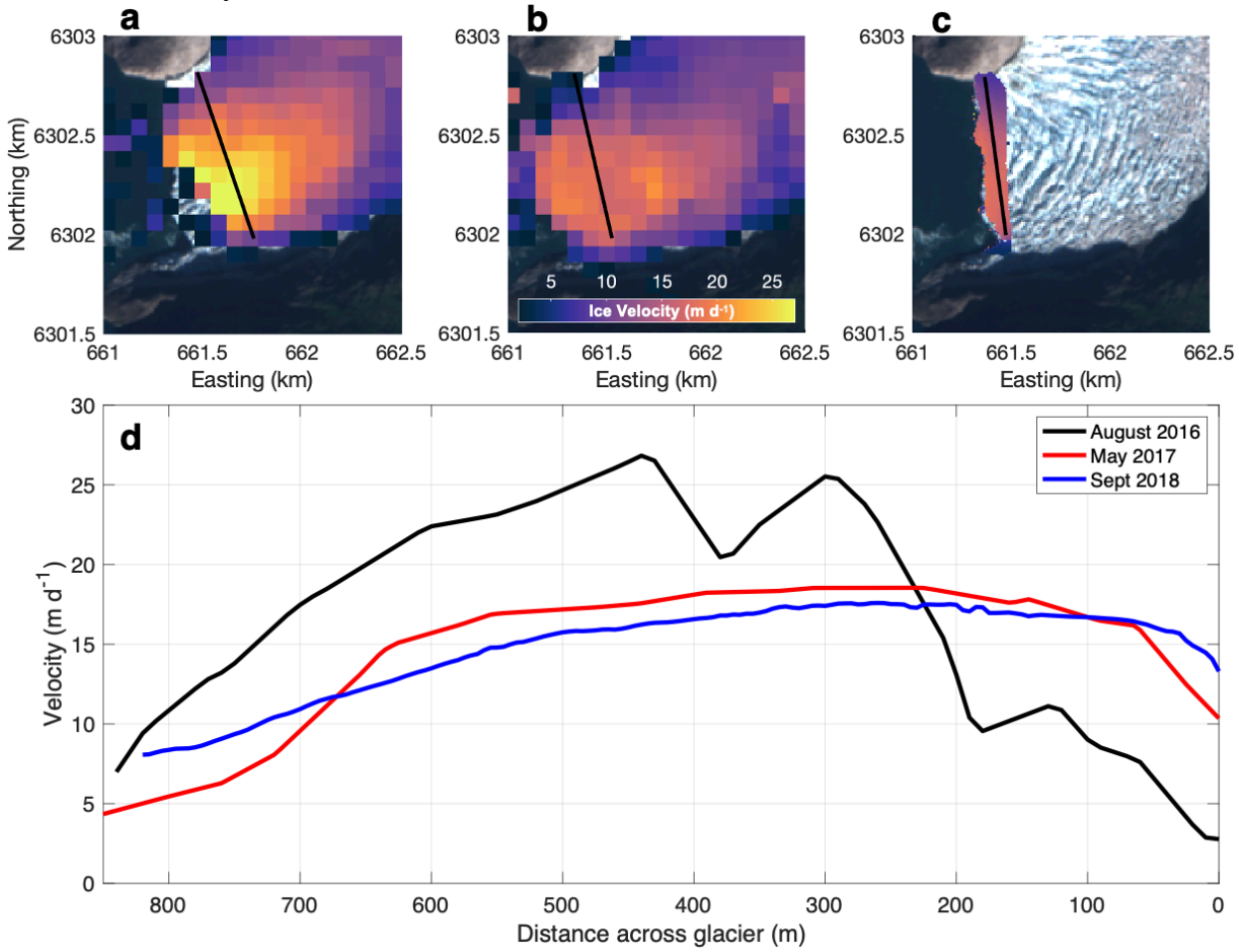

Figure A.1 Campaign averaged ice velocity fields derived using the Terrestrial Radar Interferometer in August 2016 (a) and May 2017 (b) and drone imagery in September 2018 (c) with the reference transect superimposed (black line). For frontal ablation calculations, ice velocities were extracted across a transect that was as close to the terminus as possible while still capturing a complete across-glacier profile (d).

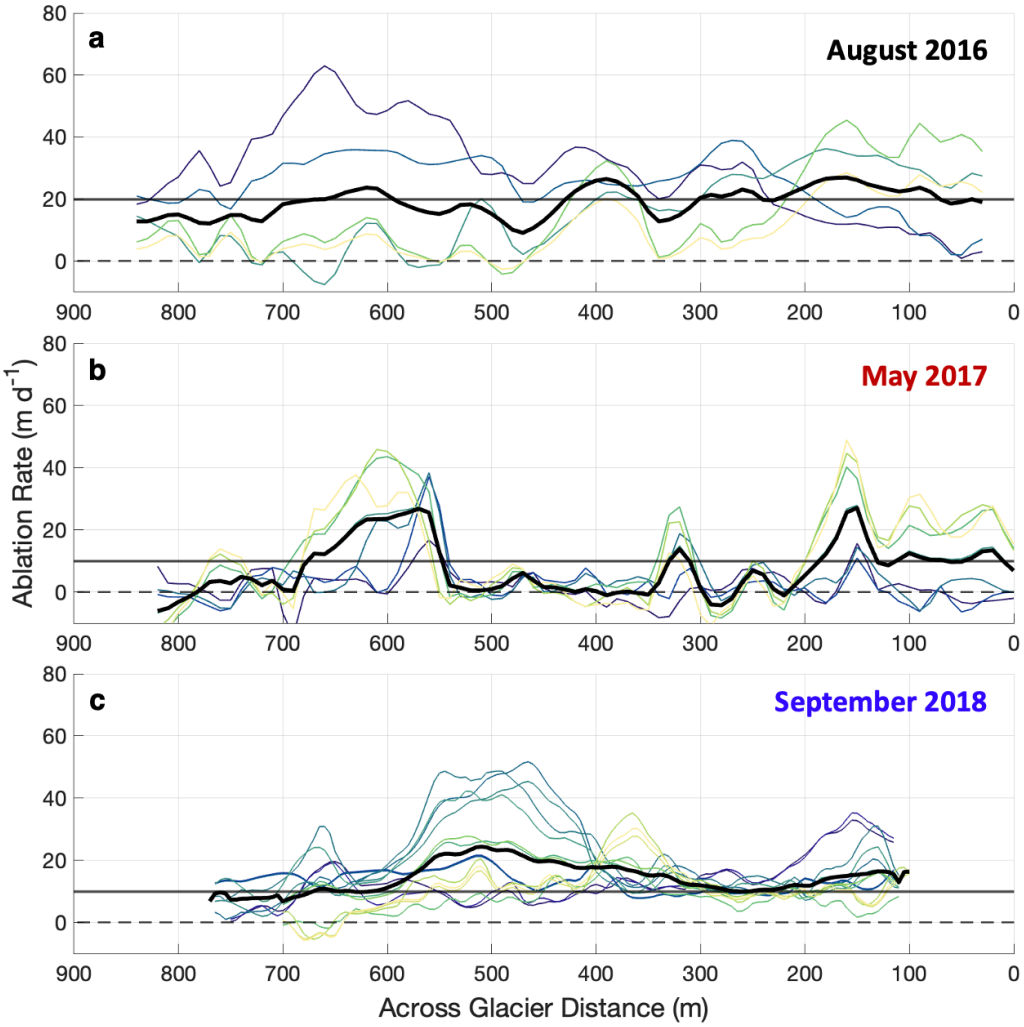

Figure A.2 Change in waterline position between each multibeam pass derived from TRI in August 2016 (a) and May 2017 (b), and time-lapse imagery in September 2018 (c). Thick black line indicates the average waterline ablation between all multibeam passes. Horizontal line at 20 m/d in August 2016 and 10 m/d in May 2017 and September 2018 show the threshold used for the characteristic calving rate in the separation of frontal ablation between iceberg calving and submarine melting.

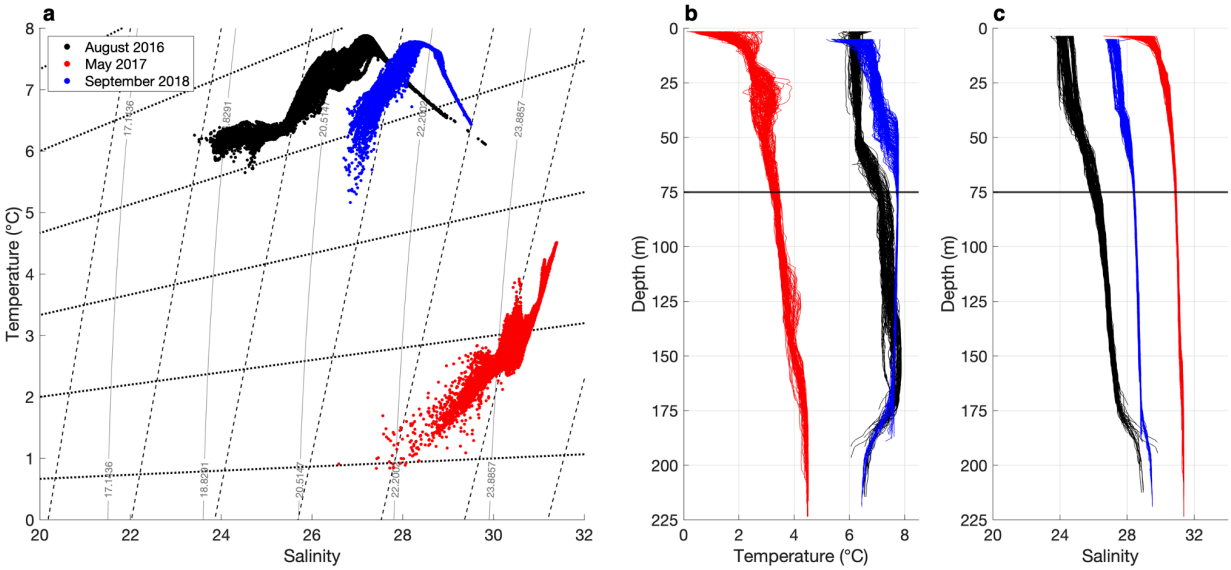

Figure A.3 (a) Hydrographic data collected by the CTD casts located in Fig. 7c shown in T-S space and overlaid with melt and runoff mixing lines. Profiles of temperature (b) and salinity (c) with depth from the same CTD casts. Ocean temperature and salinity data were averaged from 75m depth (horizontal black line) to the grounding line to remove the influence of the outflowing glacially modified plume.

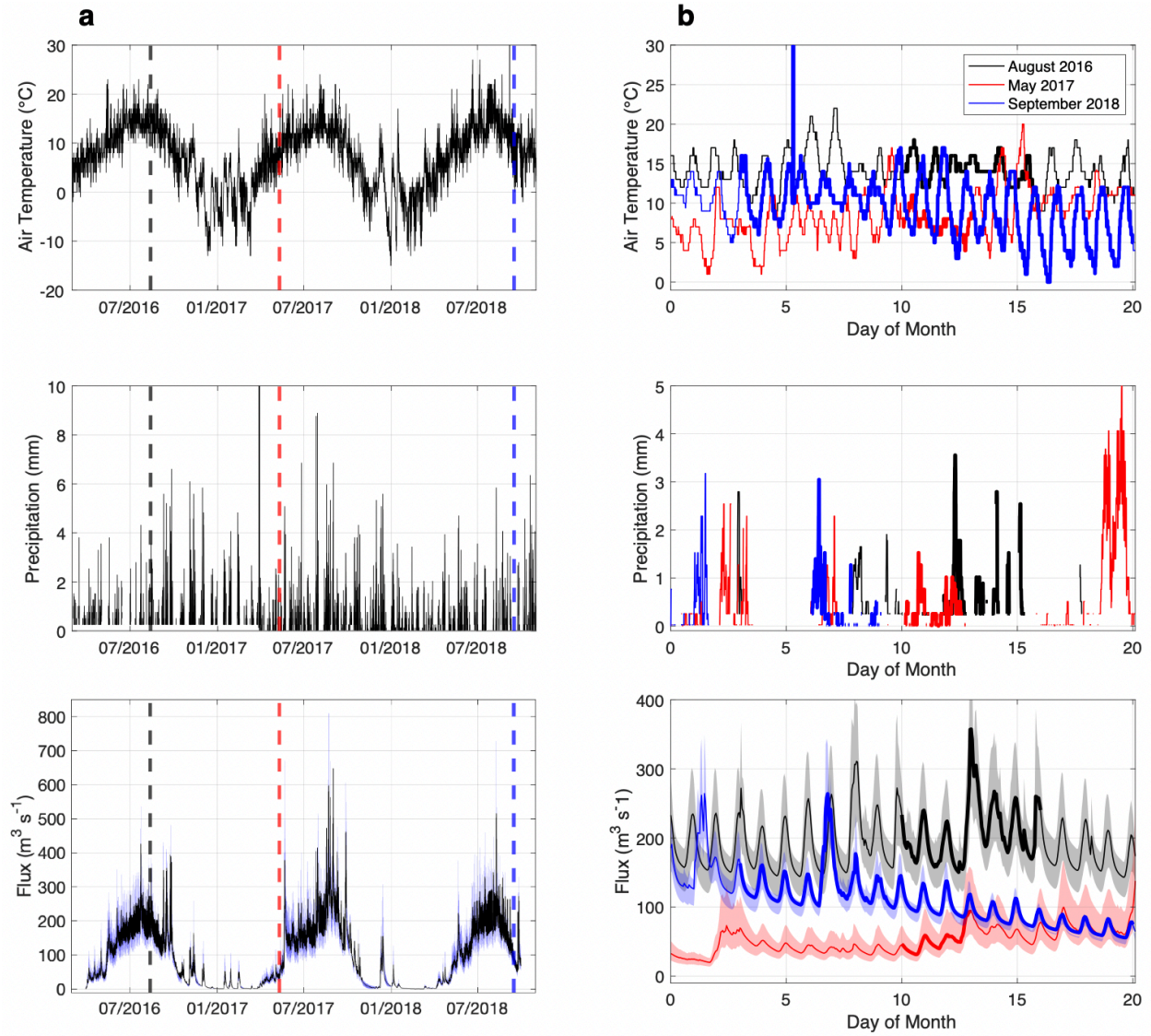

Figure A.4 (a) Time series of air temperature (top row) and precipitation (middle row) taken from Petersburg Airport used to force the subglacial discharge model (bottom row) over the course of all field campaigns (August 2016: black dashed line, May 2017: red dashed line, September 2018: blue dashed line). (b) The same time series zoomed into the dates of each field campaign, with the bolded lines indicating the time period of multibeam data collection.

A.2 Supplementary Movie Captions

Movie S1 shows short term changes in terminus morphology for August 2016 (top), May 2017 (middle), and September 2018 (bottom). (a) Across glacier cross-section taken at 100m depth. Each color indicates a different multibeam scan. (b) Vertical cross-section taken at the location of the moving vertical black line in (a).

APPENDIX B

CHAPTER III: ADDITIONAL INFORMATION ON OCEAN HYDROGRAPHY AND SUBGLACIAL DISCHARGE IN FRONT OF KANGILLIUP SERMIA

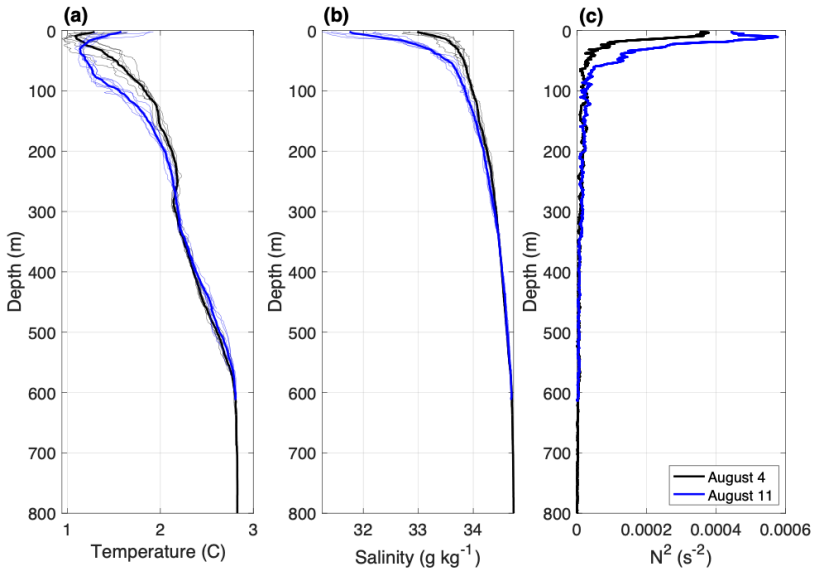

Figure B.1 Changes in T (a), S (b), and N2 (c) pre- (black line; August 4) and post-event (blue line; August 11; zoomed in profiles shown in Figure 2). Thin lines indicate individual CTD casts across the width of the glacial fjord, while thick lines indicate the average. In (c), N2 has been smoothed with a 10 m moving average.

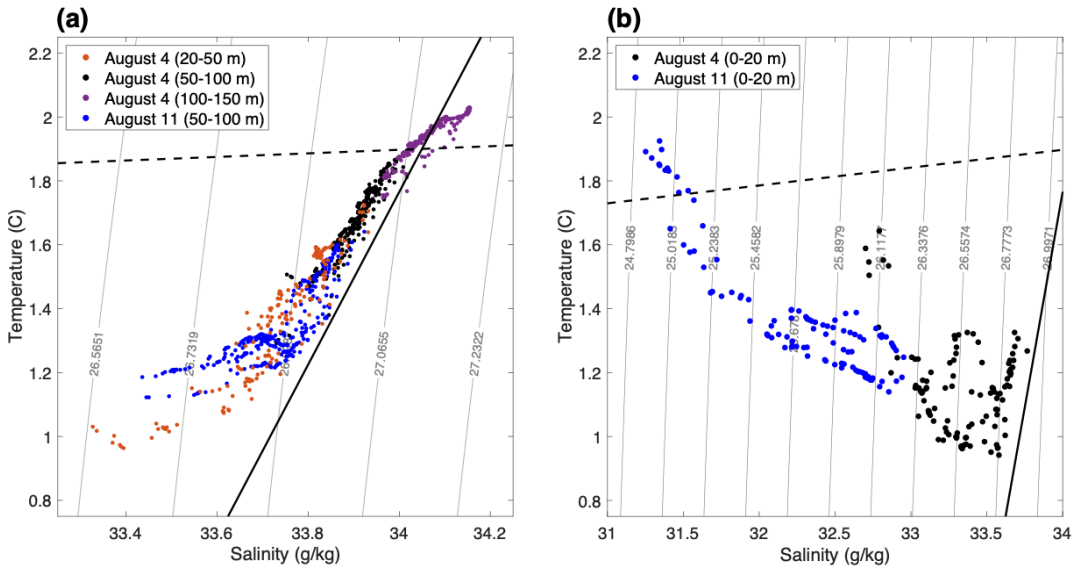

Figure B.2 Across-fjord averaged water column properties before (orange, black, and purple dots) and after (blue dots) the ephemeral ice mélange event in the (a) depth range of significant stratification change and (b) in the surface water column.

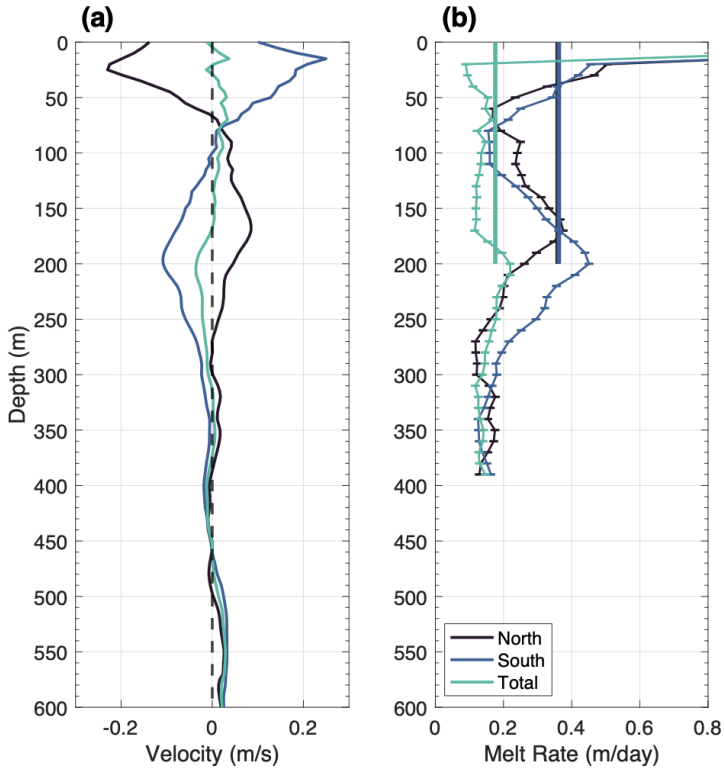

Figure B.3 (a) ADCP-derived ocean velocities averaged over the northern half, southern half, and total width of the fjord. (b) Modeled iceberg melt rates averaged across all depth classes for

each average ocean velocity profile with error bars indicating ± 1 standard deviation (thin lines) and keel-depth averaged iceberg melt rate for an iceberg that extends 200 m into the water column (thick lines).

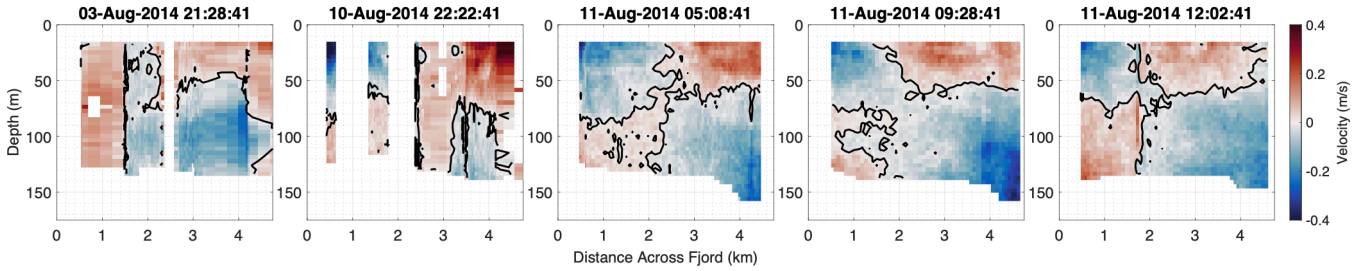

Figure B.4 Gridded SADCP-derived along-fjord velocities prior to the ice mélange event (August 3) and after the ice mélange event (August 10) taken at the hydrographic transect in Figure 1a. Positive values indicate glacierward flow, and a black contour is present at 0 m/s. The surface recirculation is strongest just after the ice mélange event but is present in all water column velocity transects.

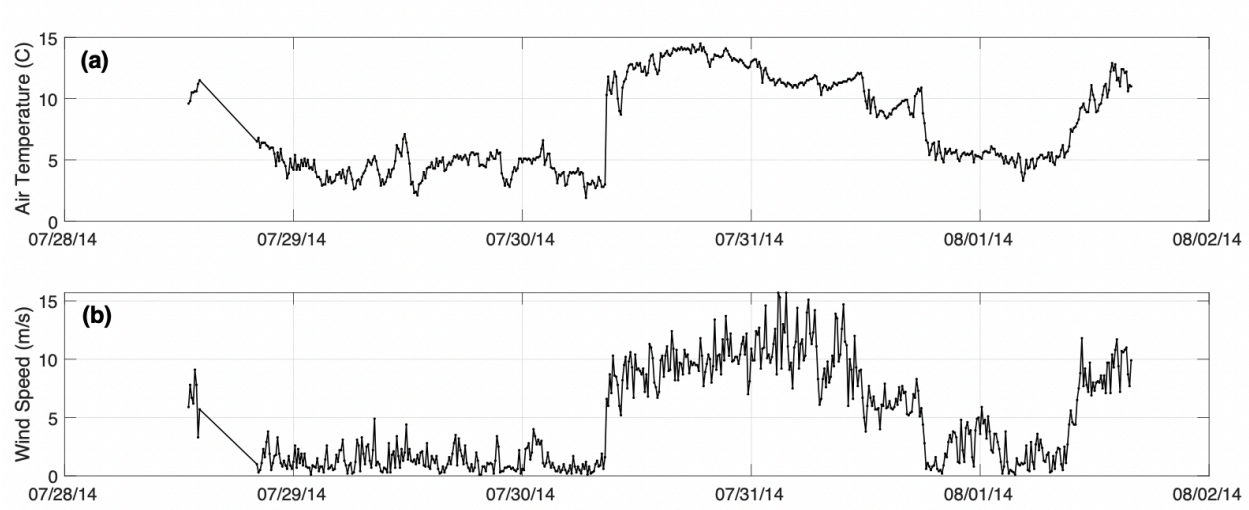

Figure B.5 Time series of (a) air temperature and (b) wind speed collected at a meteorological station on the north side of Kangilliup Sermia's terminus (Fig. 1a) and used as input to the iceberg melt model. Weather stations were recovered just before the observed ice mélange event, and we therefore use the average air temperature and wind speed during the final 5 days of the data record.

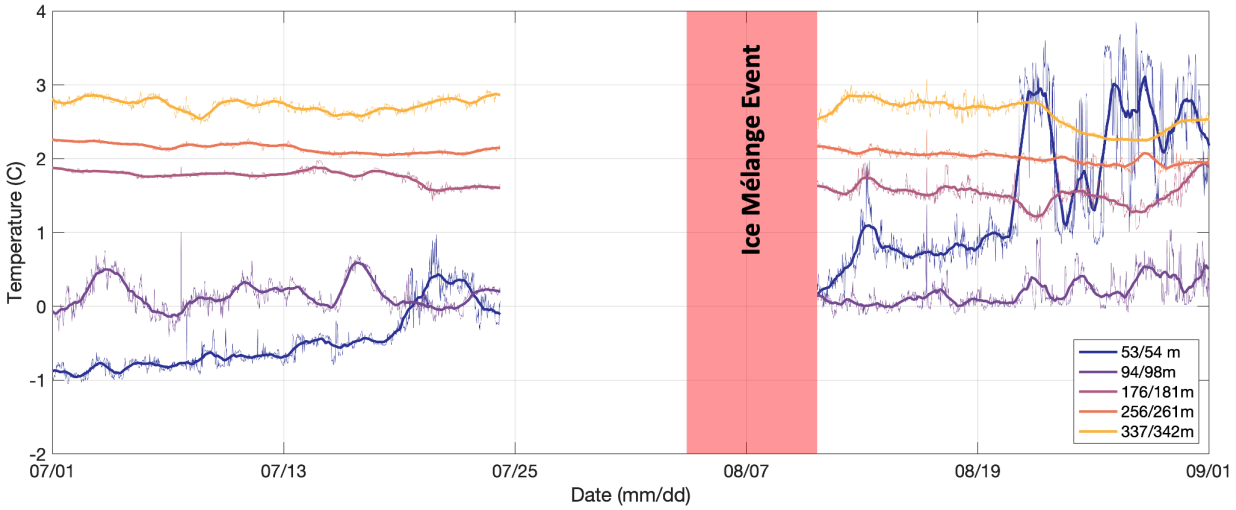

Figure B.6 Time series of ocean temperature taken at the depth of each instrument (legend) on a subsurface mooring located outside of the sills of Kangilliup Sermia and Kangerlussuup Sermia (Fig. 1a), with the timing of hydrographic observations that bound the investigated ephemeral ice mélange event indicated by the red shaded box. The thick lines indicate a 1-day moving average of ocean temperature taken at 15-minute intervals (thin lines). Hydrographic moorings were recovered, serviced, and redeployed between July 25 and August 11, leading to a gap in the hydrographic record and a slight change in deployment depths indicated in the figure legend.

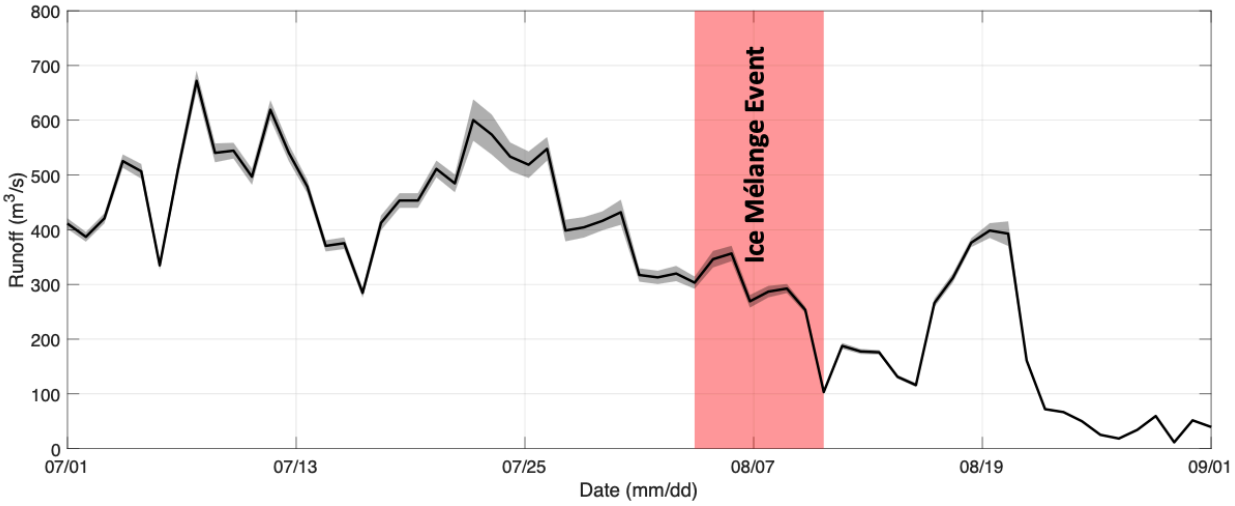

Figure B.7 Time series of subglacial discharge with grey shading indicating sensitivity of the model to high and low melt scenarios from Carroll et al. (2016). The red shaded box indicates the timing of hydrographic observations that bound the investigated ephemeral ice mélange event.

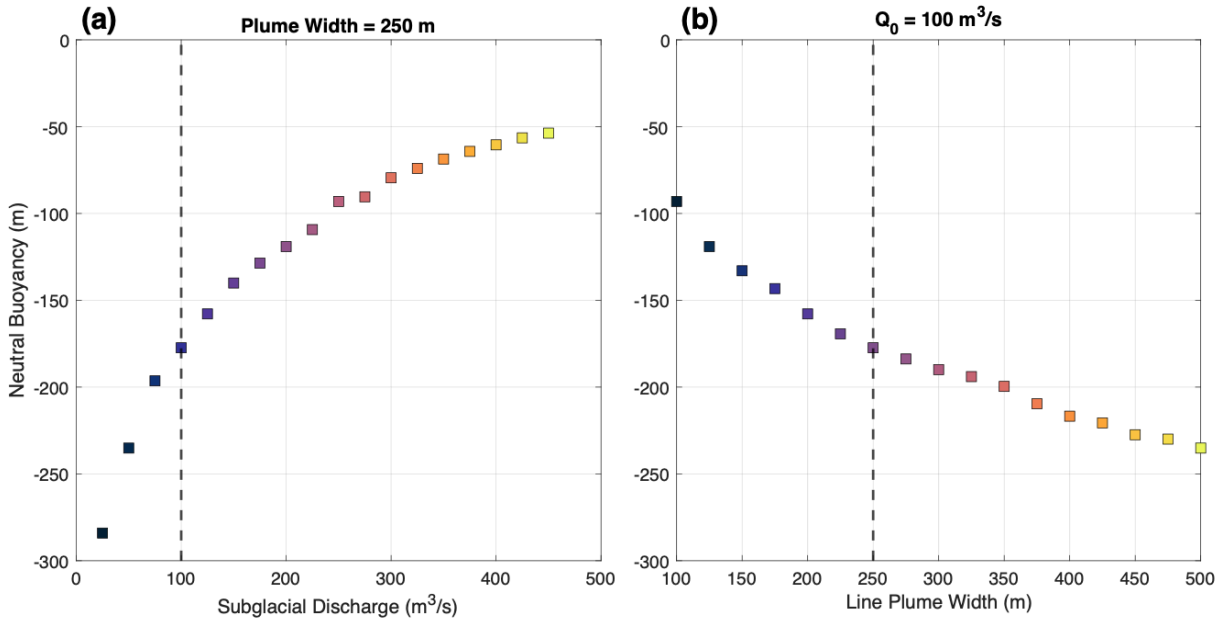

Figure B.8 Sensitivity of the height of neutral buoyancy calculation from buoyant plume theory to subglacial discharge magnitude (a) and prescribed line plume width (b). Dashed line indicates the parameters discussed in the main text.

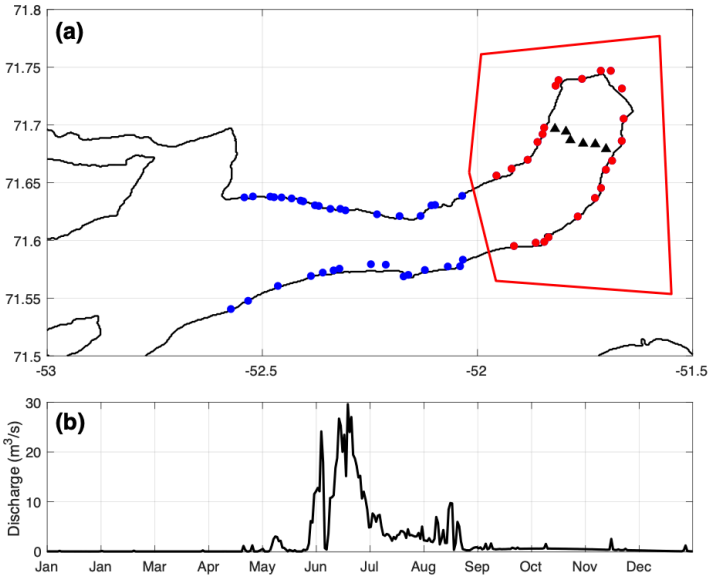

Figure B.9 (a) Riverine freshwater outlets (dots) entering the proglacial fjord of Kangilliup Sermia from Mankoff et al. (2020b), with bounding box used to isolate near-glacier freshwater outlets (red dots) for runoff calculation indicated by the red line. (b) Total freshwater discharge

into the proglacial fjord from near-glacier outlets in 2014 derived by adding together the discharge from all near-glacier riverine outlets highlighted in (a) by red dots.

Table B.1. Summary statistics of temperature and salinity from 5-200 m depth both before and after an ephemeral ice mélange event in front of Kangilliup Sermia. Statistics for the full water column are shown in parentheses.

	Temperature Variance	**Temperature Mean (°C)**	**Salinity Variance**	**Salinity Mean (g/kg)**
August 4	0.09 (0.19)	1.75 (2.35)	0.05 (0.10)	33.95 (34.42)
August 11	0.10 (0.23)	1.57 (2.15)	0.25 (0.24)	33.70 (34.25)
Difference	-	-0.18 (-0.19)	-	-0.25 (-0.18)

APPENDIX C

CHAPTER IV: ADDITIONAL INFORMATION ON ENVIRONMENTAL FORCINGS IN THE UUMMANNAQ REGION

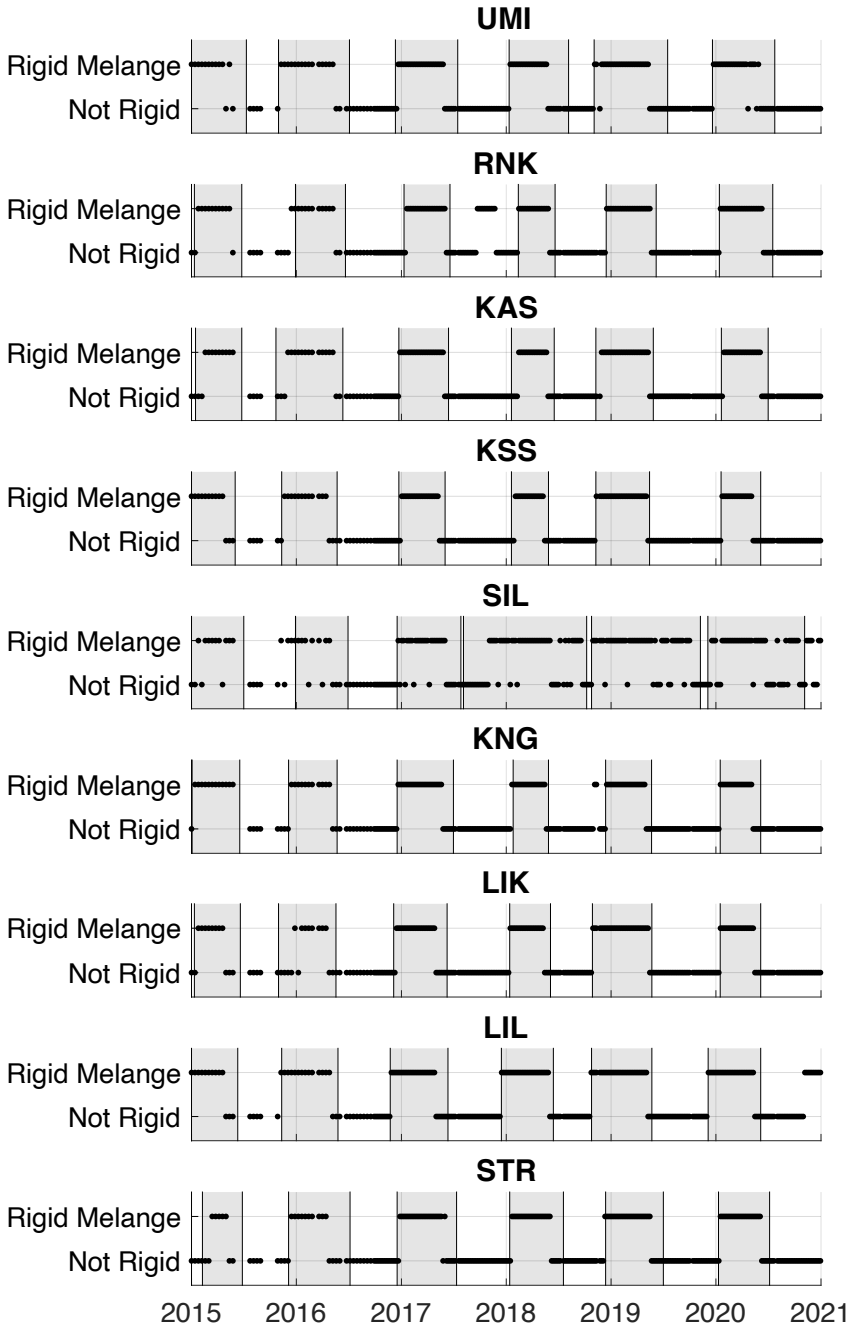

Figure C.1 Time series of ice mélange presence/absence data with the GEEDiT-derived optical time series shown as grey shading, with grey indicating seasonal ice mélange is present, and ice mélange rigidity shown as black dots.

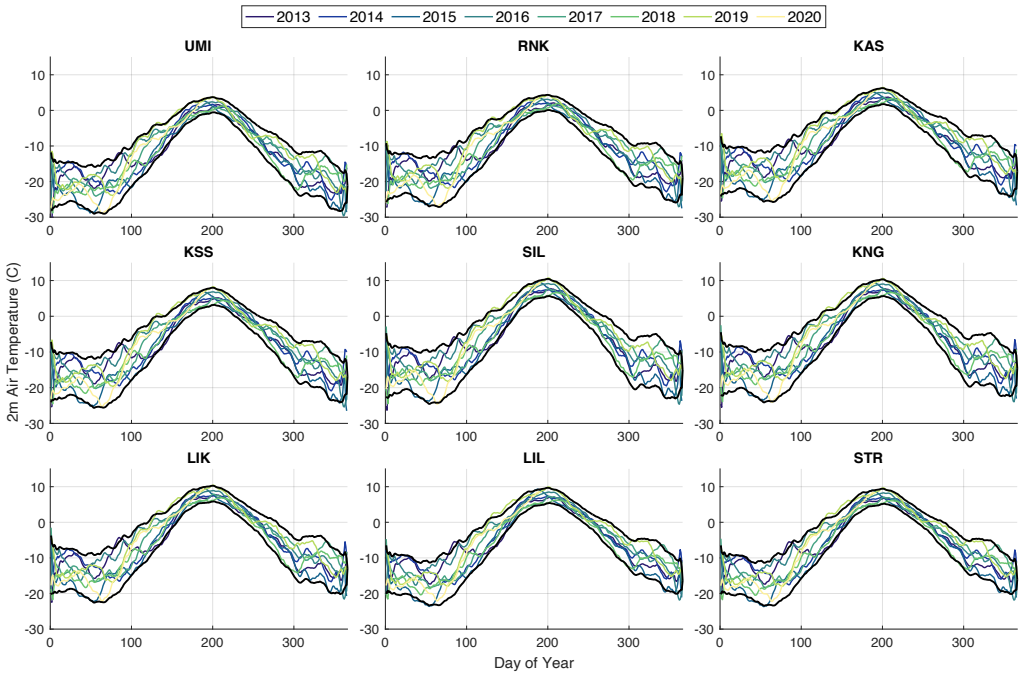

Figure C.2 Daily time series of fjord-average air temperature derived from ERA5 colored by year and climatology from the entire time series (black lines are average ± 1 standard deviation) All measurements were smoothed with a 30-day moving mean to highlight monthly trends.

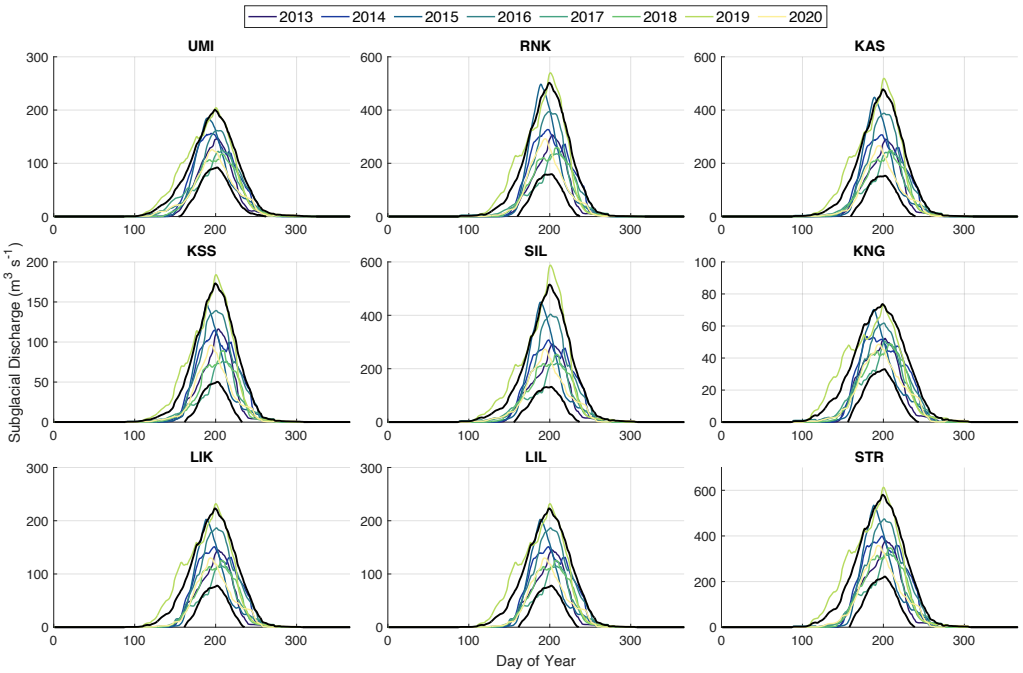

Figure C.3 Daily time series of subglacial discharge derived from Mankoff and others (2022; black lines) colored by year and climatology from the entire time series (black lines are average ± 1 standard deviation). All measurements were smoothed with a 30-day moving mean to highlight monthly trends.

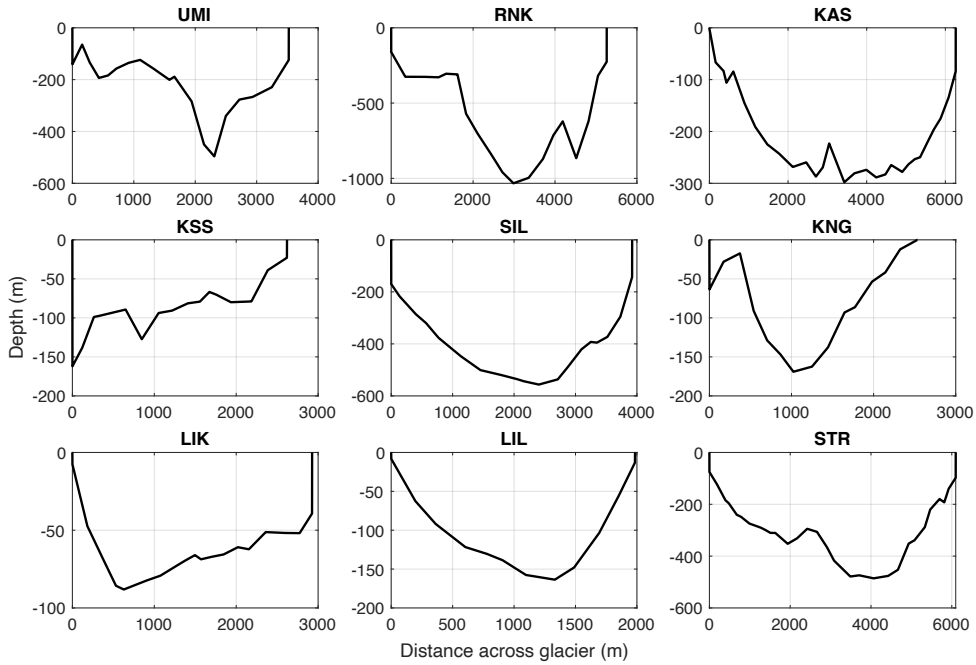

Figure C.4 Profile of the depth of the grounding line at the location of the terminus in 2017 as derived from BedMachine v5. Distance increases from south to north.

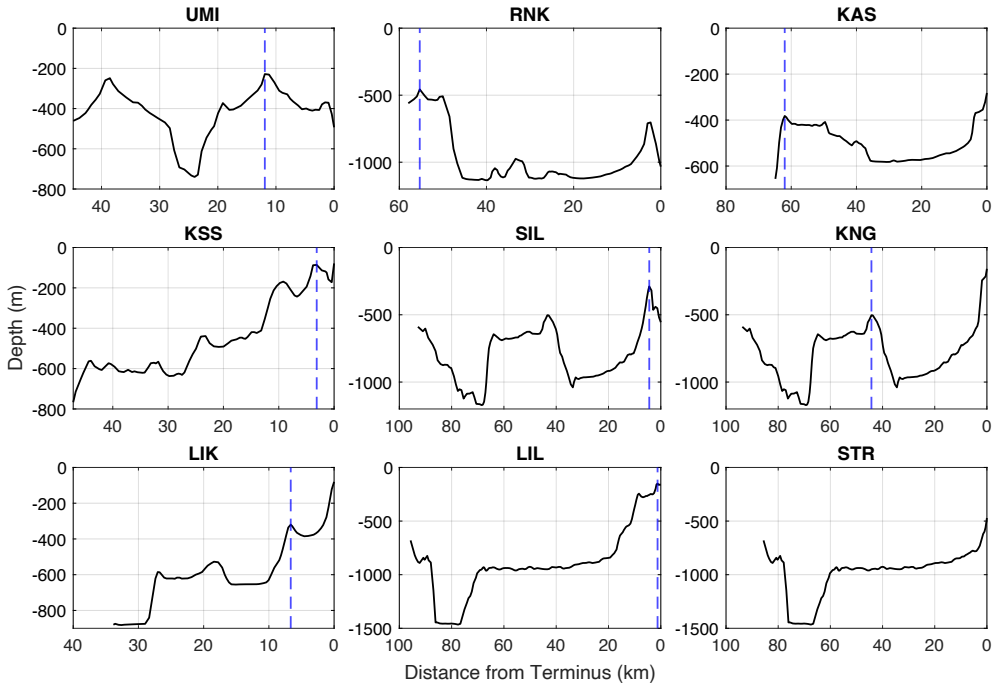

Figure C.5 Profile of the fjord bathymetry along the deepest point in the fjord between the 2017 terminus and the entrance to the fjord as derived from BedMachine v5. Distance increases away from the glacier terminus.

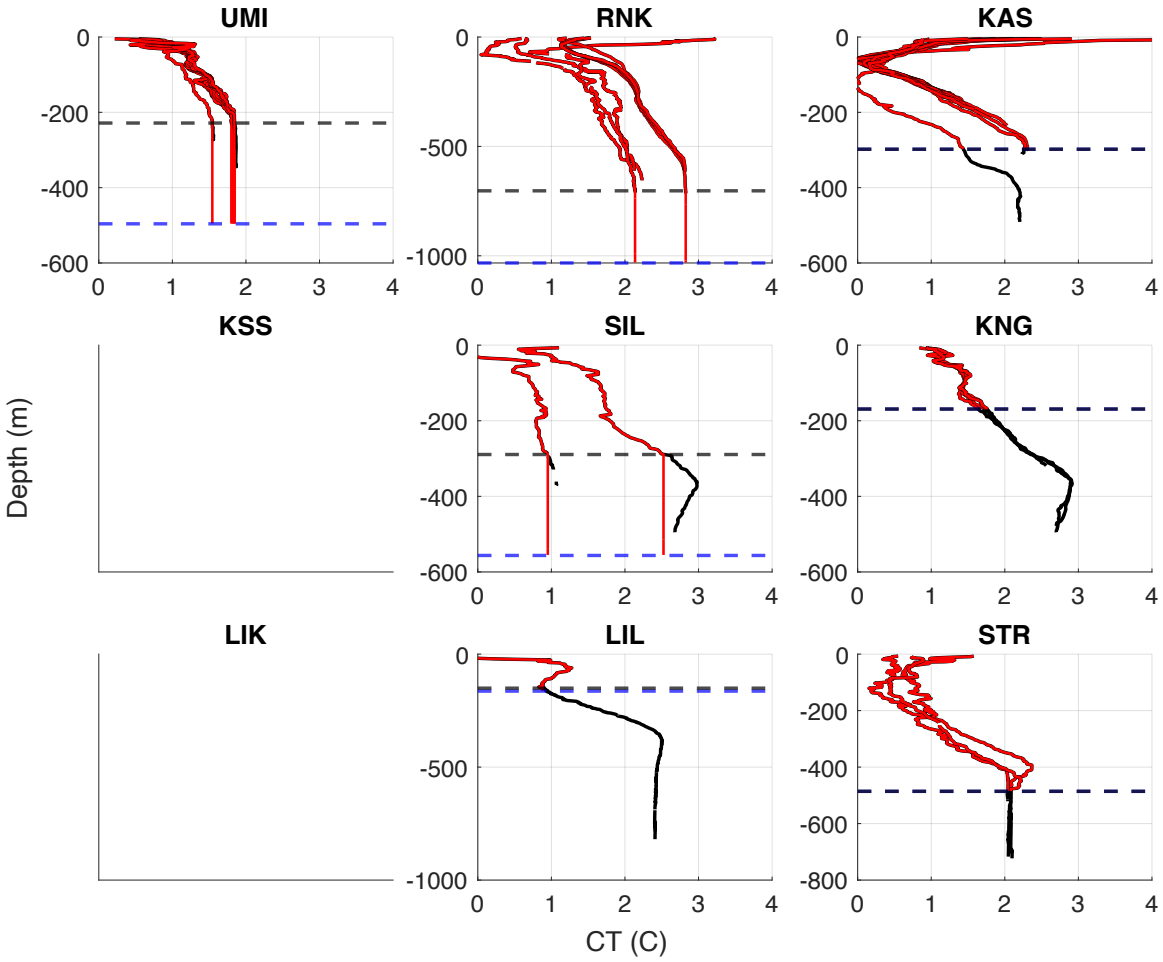

Figure C.6 Profiles of ocean temperature with depth for all fjords with available CTD Data from OMG and field data measurements. The dashed lines represent the grounding line depth (blue) and effective depth (i.e., sill depth if one is located between the cast and the grounding line (black). The original data is shown in black solid lines, whereas the extrapolated data used as input to the subglacial plume model is shown in red solid lines.

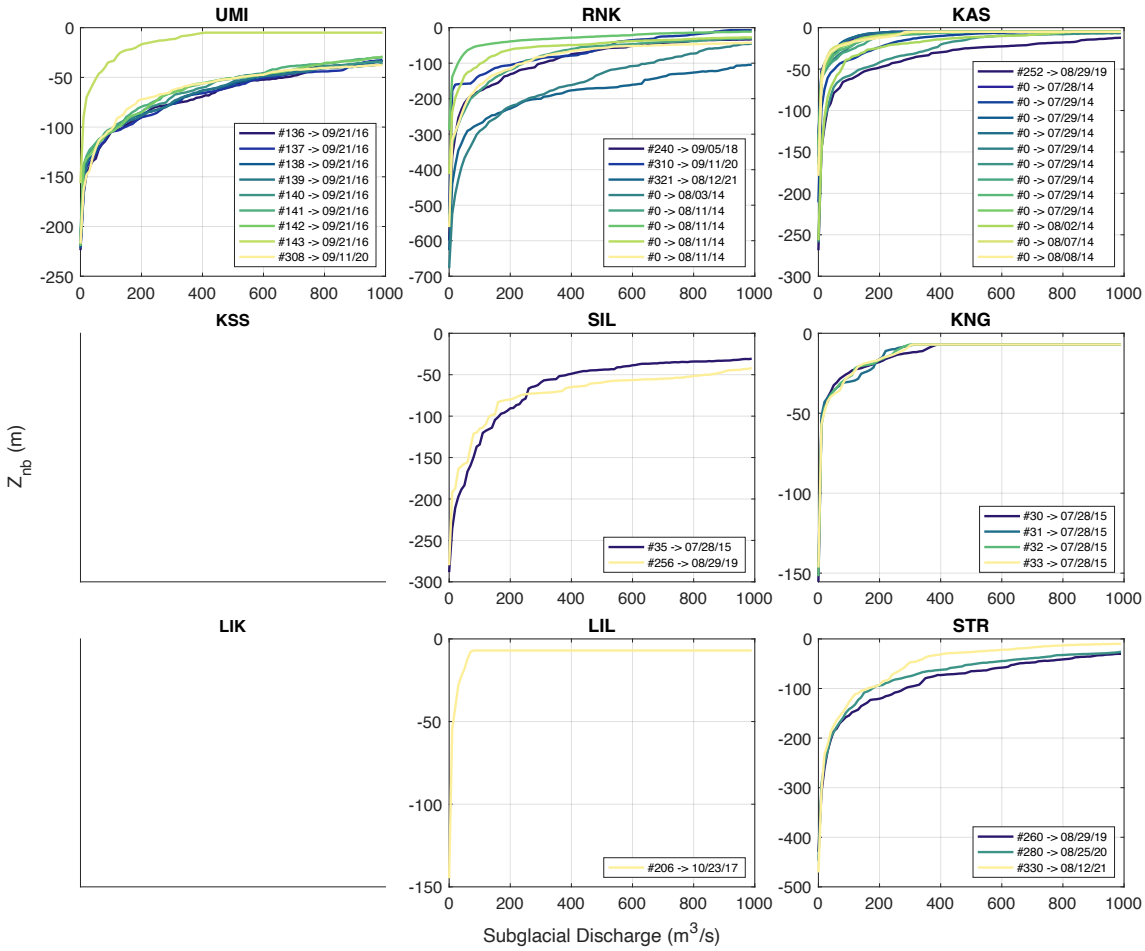

Figure C.7 Plume neutral buoyancy depth (Znb) derived from each CTD cast input into the subglacial plume model for all tested values of subglacial discharge with the legend showing the OMG CTD Cast ID Number and date. Casts that were derived from field data show an ID Number of #0.

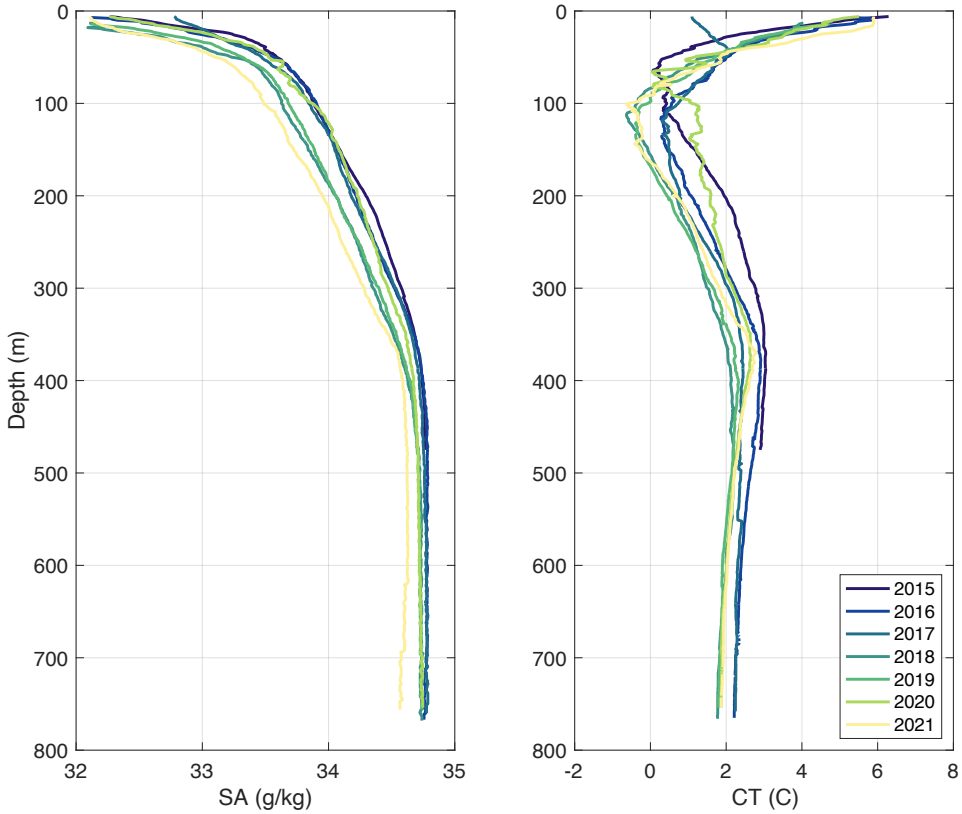

Figure C.8 Yearly averaged OMG CTD profiles with depth of the salinity (left) and temperature (right) of the water present in Uummannaq Trough.

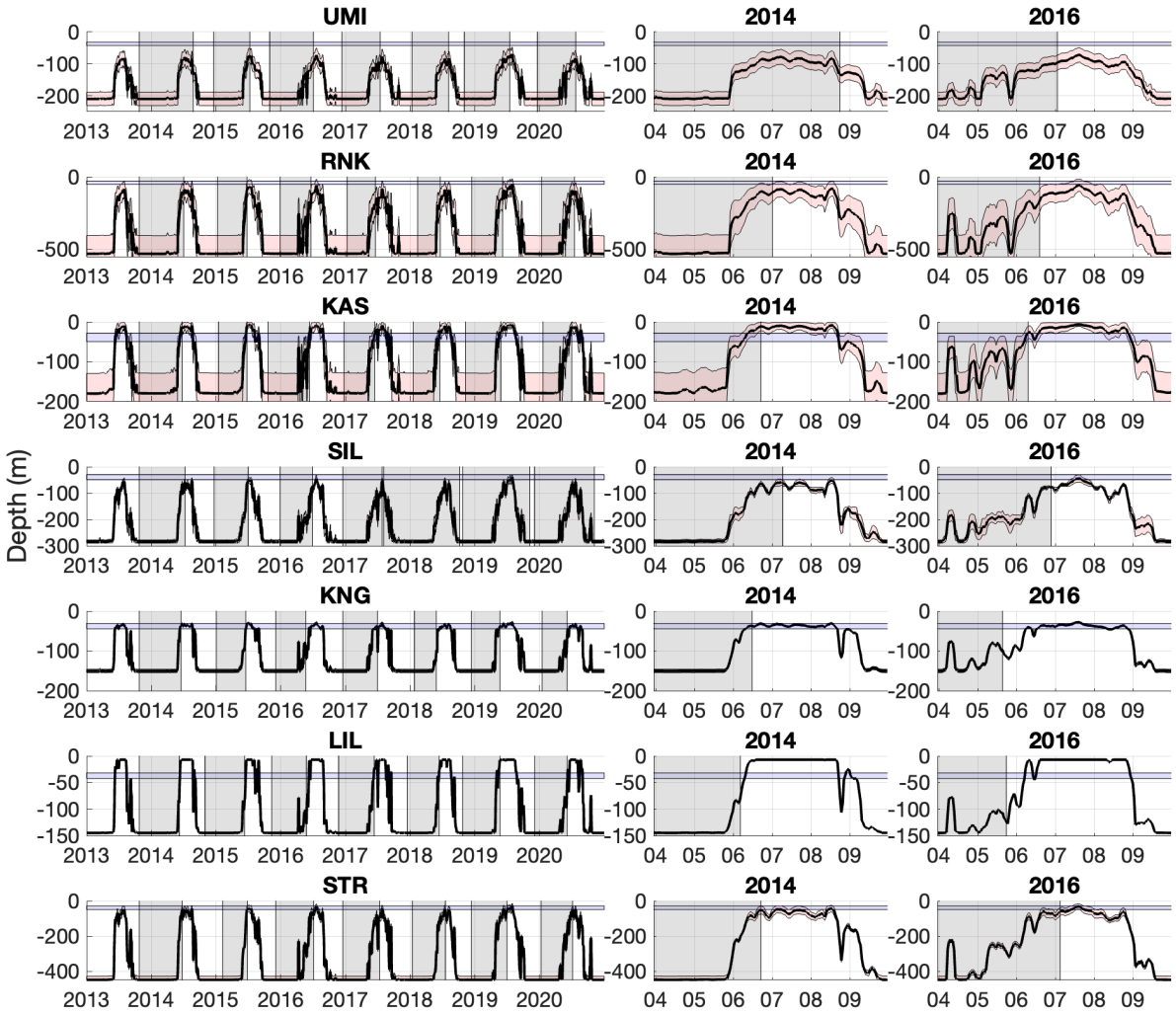

Figure C.9 Time series of plume neutral buoyancy depth (black lines with red shading for +/- 1 standard deviation) for all study fjords overlaid on seasonal ice mélange presence/absence data (grey shading, with grey indicating seasonal ice mélange is present) and the average iceberg keel depth within the ice mélange (blue shading) for the entire study period (left) and two annual subsections (middle and right).

REFERENCES CITED

CHAPTER I

Abib, N., Sutherland, D. A., Amundson, J. M., Duncan, D., Eidam, E. F., Jackson, R. H., Kienholz, C., Morlighem, M., Motyka, R. J., Nash, J. D., Ovall, B., & Pettit, E. C. (2023). Persistent overcut regions dominate the terminus morphology of a rapidly melting tidewater glacier. Annals of Glaciology, 1–12. https://doi.org/10.1017/aog.2023.38

Abib, N., Sutherland, D. A., Peterson, R., Catania, G., Nash, J. D., Emily, L., Stearns, L. A., & Bartholomaus, T. C. (2024). Ice mélange melt drives changes in observed water column stratification at a tidewater glacier in Greenland. The Cryosphere Discussions, March, 1–21. https://doi.org/10.5194/egusphere-2024-504

Benn, D. I., Aström, J., Zwinger, T., Todd, J., Nick, F. M., Cook, S., Hulton, N. R. J., & Luckman, A. (2017). Melt-under-cutting and buoyancy-driven calving from tidewater glaciers: New insights from discrete element and continuum model simulations. Journal of Glaciology, 63(240), 691–702. https://doi.org/10.1017/jog.2017.41

Benn, D. I., Cowton, T., Todd, J., & Luckman, A. (2017). Glacier Calving in Greenland. Current Climate Change Reports, 3, 282–290. https://doi.org/10.1007/s40641-017-0070-1

Carroll, D., Sutherland, D. A., Hudson, B., Moon, T., Catania, G. A., Shroyer, E. L., Nash, J. D., Bartholomaus, T. C., Felikson, D., Stearns, L. A., Noël, B. P. Y., & van den Broeke, M. R. (2016). The impact of glacier geometry on meltwater plume structure and submarine melt in Greenland fjords. Geophysical Research Letters, 43, 9739–9748. https://doi.org/10.1002/2016GL070170

Carroll, D., Sutherland, D. A., Shroyer, E. L., Nash, J. D., Catania, G. A., & Stearns, L. A. (2015). Modeling turbulent subglacial meltwater plumes: Implications for fjord-scale buoyancy-driven circulation. Journal of Physical Oceanography, 45(8), 2169–2185. https://doi.org/10.1175/JPO-D-15-0033.1

Catania, G. A., Stearns, L. A., Sutherland, D. A., Fried, M. J., Bartholomaus, T. C., Morlighem, M., Shroyer, E., & Nash, J. (2018). Geometric Controls on Tidewater Glacier Retreat in Central Western Greenland. Journal of Geophysical Research: Earth Surface, 123(8), 2024–2038. https://doi.org/10.1029/2017JF004499

Cowton, T., Slater, D., Sole, A., Goldberg, D., & Nienow, P. (2015). Modeling the impact of glacial runoff on fjord circulation and submarine melt rate using a new subgrid-scale parameterization for glacial plumes. Journal of Geophysical Research: Oceans, 120(2), 796–812. https://doi.org/10.1002/2014JC010324

Davison, B. J., Cowton, T. R., Cottier, F. R., & Sole, A. J. (2020). Iceberg melting substantially modifies oceanic heat flux towards a major Greenlandic tidewater glacier. Nature Communications, 11(5983). https://doi.org/10.1038/s41467-020-19805-7

Davison, B. J., Cowton, T., Sole, A., Cottier, F., & Nienow, P. (2022). Modelling the effect of submarine iceberg melting on glacier-adjacent water properties. Cryosphere, 16(4), 1181–1196. https://doi.org/10.5194/tc-16-1181-2022

Depoorter, M. A., Bamber, J. L., Griggs, J. A., Lenaerts, J. T. M., Ligtenberg, S. R. M., Van Den Broeke, M. R., & Moholdt, G. (2013). Calving fluxes and basal melt rates of Antarctic ice shelves. Nature, 502(7469), 89–92. https://doi.org/10.1038/nature12567

Enderlin, E. M., Howat, I. M., Jeong, S., Noh, M.-J., van Angelen, J. H., & van den Broeke, M. R. (2014). An improved mass budget for the Greenland ice sheet. Geophysical Research Letters, 41, 866–872. https://doi.org/10.1002/2013GL059010

Fried, M. J., Carroll, D., Catania, G. A., Sutherland, D. A., Stearns, L. A., Shroyer, E. L., & Nash, J. D. (2019). Distinct Frontal Ablation Processes Drive Heterogeneous Submarine Terminus Morphology. Geophysical Research Letters, 46(21), 12083–12091. https://doi.org/10.1029/2019GL083980

Fried, M. J., Catania, G. A., Bartholomaus, T. C., Duncan, D., Davis, M., Stearns, L. A., Nash, J., Shroyer, E., & Sutherland, D. (2015). Distributed subglacial discharge drives significant submarine melt at a Greenland tidewater glacier. Geophysical Research Letters, 42(21), 9328–9336. https://doi.org/10.1002/2015GL065806

Greene, C. A., Gardner, A. S., Wood, M., & Cuzzone, J. K. (2024). Ubiquitous acceleration in Greenland Ice Sheet calving from 1985 to 2022. Nature, 625(7995), 523–528. https://doi.org/10.1038/s41586-023-06863-2

Hager, A. O., Sutherland, D. A., & Slater, D. A. (2024). Local forcing mechanisms challenge parameterizations of ocean thermal forcing for Greenland tidewater glaciers. The Cryosphere, 18(2), 911–932. https://doi.org/10.5194/tc-18-911-2024

Holland, D. M., & Jenkins, A. (1999). Modeling thermodynamic ice-ocean interactions at the base of an ice shelf. Journal of Physical Oceanography, 29(8), 1787–1800. https://doi.org/10.1175/1520-0485(1999)029<1787:mtioia>2.0.co;2

Jackson, R. H., Nash, J. D., Kienholz, C., Sutherland, D. A., Amundson, J. M., Motyka, R. J., Winters, D., Skyllingstad, E., & Pettit, E. C. (2020). Meltwater Intrusions Reveal Mechanisms for Rapid Submarine Melt at a Tidewater Glacier. Geophysical Research Letters, 47. https://doi.org/10.1029/2019GL085335

Jenkins, A. (1999). The Impact of Melting Ice on Ocean Waters. Journal of Physical Oceanography, 29(9), 2370–2381. https://doi.org/10.1175/1520-0485(1999)029<2370:TIOMIO>2.0.CO;2

Jenkins, A. (2011). Convection-driven melting near the grounding lines of ice shelves and tidewater glaciers. Journal of Physical Oceanography, 41(12), 2279–2294. https://doi.org/10.1175/JPO-D-11-03.1

Kimura, S., Holland, P. R., Jenkins, A., & Piggott, M. (2014). The effect of meltwater plumes on the melting of a vertical glacier face. Journal of Physical Oceanography, 44(12), 3099–3117. https://doi.org/10.1175/JPO-D-13-0219.1

King, M. D., Howat, I. M., Candela, S. G., Noh, M. J., Jeong, S., Noël, B. P. Y., van den Broeke, M. R., Wouters, B., & Negrete, A. (2020). Dynamic ice loss from the Greenland Ice Sheet driven by sustained glacier retreat. Communications Earth & Environment, 1(1), 1–7. https://doi.org/10.1038/s43247-020-0001-2

Kochtitzky, W., Copland, L., King, M., Hugonnet, R., Jiskoot, H., Morlighem, M., Millan, R., Khan, S. A., & Noël, B. (2023). Closing Greenland's Mass Balance: Frontal Ablation of Every Greenlandic Glacier From 2000 to 2020. Geophysical Research Letters, 50(17), 1–9. https://doi.org/10.1029/2023GL104095

Kochtitzky, W., Copland, L., Van Wychen, W., Hugonnet, R., Hock, R., Dowdeswell, J. A., Benham, T., Strozzi, T., Glazovsky, A., Lavrentiev, I., Rounce, D. R., Millan, R., Cook, A., Dalton, A., Jiskoot, H., Cooley, J., Jania, J., & Navarro, F. (2022). The unquantified mass loss of Northern Hemisphere marine-terminating glaciers from 2000–2020. Nature Communications, 13(1), 5835. https://doi.org/10.1038/s41467-022-33231-x

Ma, Y., & Bassis, J. N. (2019). The Effect of Submarine Melting on Calving From Marine Terminating Glaciers. Journal of Geophysical Research: Earth Surface, 124, 334–346. https://doi.org/10.1029/2018JF004820

McNabb, R. W., & Hock, R. (2015). Variations in Alaska tidewater glacier frontal ablation, 1985-2013. Journal of Geophysical Research: Earth Surface, 120, 120–136. https://doi.org/10.1002/2014JF003276

Minowa, M., Schaefer, M., Sugiyama, S., Sakakibara, D., & Skvarca, P. (2021). Frontal ablation and mass loss of the Patagonian icefields. Earth and Planetary Science Letters, 561, 116811. https://doi.org/10.1016/j.epsl.2021.116811

Mortensen, J., Lennert, K., Bendtsen, J., & Rysgaard, S. (2011). Heat sources for glacial melt in a sub-Arctic fjord (Godthåbsfjord) in contact with the Greenland Ice Sheet. Journal of Geophysical Research: Oceans, 116, 1–13. https://doi.org/10.1029/2010JC006528

Podrasky, D., Truffer, M., Lüthi, M., & Fahnestock, M. (2014). Quantifying velocity response to ocean tides and calving near the terminus of Jakobshavn Isbræ, Greenland. Journal of Glaciology, 60(222), 609–621. https://doi.org/10.3189/2014JoG13J130

Rignot, E., Fenty, I., Xu, Y., Cai, C., & Kemp, C. (2015). Undercutting of marine-terminating glaciers in West Greenland. Geophysical Research Letters, 42, 5909–5917. https://doi.org/10.1002/2015GL064236

Slater, D. A., Benn, D. I., Cowton, T. R., Bassis, J. N., & Todd, J. A. (2021). Calving Multiplier Effect Controlled by Melt Undercut Geometry. Journal of Geophysical Research: Earth Surface, 126(7), 1–17. https://doi.org/10.1029/2021JF006191

Slater, D. A., Felikson, D., Straneo, F., Goelzer, H., Little, C. M., Morlighem, M., Fettweis, X., & Nowicki, S. (2020). Twenty-first century ocean forcing of the Greenland ice sheet for modelling of sea level contribution. Cryosphere, 14, 985–1008. https://doi.org/10.5194/tc-14-985-2020

Slater, D. A., Goldberg, D. N., Nienow, P. W., & Cowton, T. R. (2016). Scalings for submarine melting at tidewater glaciers from buoyant plume theory. Journal of Physical Oceanography, 46(6), 1839–1855. https://doi.org/10.1175/JPO-D-15-0132.1

Slater, D. A., Nienow, P., Sole, A., Cowton, T., Mottram, R., Langen, P., & Mair, D. (2017). Spatially distributed runoff at the grounding line of a large Greenlandic tidewater glacier inferred from plume modelling. Journal of Glaciology, 63(238), 309–323. https://doi.org/10.1017/jog.2016.139

Slater, D. A., Nienow, P. W., Cowton, T. R., Goldberg, D. N., & Sole, A. J. (2015). Effect of near-terminus subglacial hydrology on tidewater glacier submarine melt rates. Geophysical Research Letters, 42, 2861–2868. https://doi.org/10.1080/10550887.2011.581988

Slater, D. A., Nienow, P. W., Goldberg, D. N., Cowton, T. R., & Sole, A. J. (2017). A model for tidewater glacier undercutting by submarine melting. Geophysical Research Letters, 44, 2360–2368. https://doi.org/10.1002/2016GL072374

Smith, B., Fricker, H. A., Gardner, A. S., Medley, B., Nilsson, J., Paolo, F. S., Holschuh, N., Adusumilli, S., Brunt, K., Csatho, B., Harbeck, K., Markus, T., Neumann, T., Siegfried, M. R., & Zwally, H. J. (2020). Pervasive ice sheet mass loss reflects competing ocean and atmosphere processes. Science, 368(6496), 1239–1242. https://doi.org/10.1126/science.aaz5845

Straneo, F., & Heimbach, P. (2013). North Atlantic warming and the retreat of Greenland's outlet glaciers. Nature, 504(7478), 36–43. https://doi.org/10.1038/nature12854

Van Den Broeke, M. R., Enderlin, E. M., Howat, I. M., Kuipers Munneke, P., Noël, B. P. Y., Jan Van De Berg, W., Van Meijgaard, E., & Wouters, B. (2016). On the recent contribution of the Greenland ice sheet to sea level change. Cryosphere, 10, 1933–1946. https://doi.org/10.5194/tc-10-1933-2016

Wood, M., Rignot, E., Fenty, I., An, L., Bjørk, A., Broeke, M. Van Den, Cai, C., Kane, E., Menemenlis, D., Millan, R., Morlighem, M., Mouginot, J., Noël, B., Scheuchl, B., Velicogna, I., Willis, J. K., & Zhang, H. (2021). Ocean forcing drives glacier retreat in Greenland. Science Advances, 7(1), 1–10.

Wood, M., Rignot, E., Fenty, I., Menemenlis, D., Millan, R., Morlighem, M., Mouginot, J., & Seroussi, H. (2018). Ocean-Induced Melt Triggers Glacier Retreat in Northwest Greenland. Geophysical Research Letters, 45(16), 8334–8342. https://doi.org/10.1029/2018GL078024

Xu, Y., Rignot, E., Fenty, I., Menemenlis, D., & Flexas, M. M. (2013). Subaqueous melting of Store Glacier, west Greenland from three-dimensional, high-resolution numerical modeling and ocean observations. Geophysical Research Letters, 40, 4648–4653. https://doi.org/10.1002/grl.50825

CHAPTER II

Amaral T, Bartholomaus TC and Enderlin EM (2020) Evaluation of Iceberg Calving Models Against Observations From Greenland Outlet Glaciers. *Journal of Geophysical Research: Earth Surface* 125, 1–29. doi:10.1029/2019JF005444.

Amundson JM and others (2020) Formation, flow and break-up of ephemeral ice mélange at LeConte Glacier and Bay, Alaska. *Journal of Glaciology*, 1–14. doi:10.1017/jog.2020.29.

Benn DI and others (2017) Melt-under-cutting and buoyancy-driven calving from tidewater glaciers: New insights from discrete element and continuum model simulations. *Journal of Glaciology* 63(240), 691–702. doi:10.1017/jog.2017.41.

Benn DI, Warren CR and Mottram RH (2007) Calving processes and the dynamics of calving glaciers. *Earth-Science Reviews* 82, 143–179. doi:10.1016/j.earscirev.2007.02.002.

Bouguet J-Y (2000) Pyramidal Implementatioon of the Affine Lucas Kanade Feature Tracker Description of the algorithm. *Open CV Document, Intel, Microprocessor Research Labs*.

Brinkerhoff D, Truffer M and Aschwanden A (2017) Sediment transport drives tidewater glacier periodicity. *Nature Communications* 8(1). doi:10.1038/s41467-017-00095-5.

Van Den Broeke MR and others (2016) On the recent contribution of the Greenland ice sheet to sea level change. *Cryosphere* 10, 1933–1946. doi:10.5194/tc-10-1933-2016.

Bushuk M, Holland DM, Stanton TP, Stern A and Gray C (2019) Ice scallops: a laboratory investigation of the ice–water interface. *Journal of Fluid Mechanics* 873(2), 942–976. doi:10.1017/jfm.2019.398.

Carroll D and others (2016) The impact of glacier geometry on meltwater plume structure and

submarine melt in Greenland fjords. *Geophysical Research Letters* 43, 9739–9748. doi:10.1002/2016GL070170.

Catania GA and others (2018) Geometric Controls on Tidewater Glacier Retreat in Central Western Greenland. *Journal of Geophysical Research: Earth Surface* 123(8), 2024–2038. doi:10.1029/2017JF004499.

Chauché N and others (2014) Ice-ocean interaction and calving front morphology at two west Greenland tidewater outlet glaciers. *Cryosphere* 8(4), 1457–1468. doi:10.5194/tc-8-1457-2014.

Cowton TR, Todd JA and Benn DI (2019) Sensitivity of Tidewater Glaciers to Submarine Melting Governed by Plume Locations. *Geophysical Research Letters* 46, 11,219-11,227. doi:10.1029/2019GL084215.

Cowton T, Slater D, Sole A, Goldberg D and Nienow P (2015) Modeling the impact of glacial runoff on fjord circulation and submarine melt rate using a new subgrid-scale parameterization for glacial plumes. *Journal of Geophysical Research: Oceans* 120(2), 796–812. doi:10.1002/2014JC010324.

Cusack JM and others (in press) Internal waves excited by subglacial discharge: implications for tidewater glacier melt. *Geophysical Research Letters*. doi:10.1029/2022GL102426.

Dykes R, Brook M, Robertson C and Fuller I (2011) Twenty-first century calving retreat of Tasman glacier, Southern Alps, New Zealand. *Arctic, Antarctic, and Alpine Research* 43(1), 1–10. doi:10.1657/1938-4246-43.1.1.

Eidam EF, Sutherland DA, Duncan D, Kienholz C, Amundson JM and Motyka RJ (2020) Morainal Bank Evolution and Impact on Terminus Dynamics During a Tidewater Glacier Stillstand. *Journal of Geophysical Research: Earth Surface* 125(11), 1–20. doi:10.1029/2019jf005359.

Enderlin EM, Howat IM, Jeong S, Noh M-J, van Angelen JH and van den Broeke MR (2014) An improved mass budget for the Greenland ice sheet. *Geophysical Research Letters* 41, 866–872. doi:10.1002/2013GL059010.

Ezhova E, Cenedese C and Brandt L (2018) Dynamics of three-dimensional turbulent wall plumes and implications for estimates of submarine glacier melting. *Journal of Physical Oceanography* 48(9), 1941–1950. doi:10.1175/JPO-D-17-0194.1.

Fried MJ and others (2019) Distinct Frontal Ablation Processes Drive Heterogeneous Submarine Terminus Morphology. *Geophysical Research Letters* 46(21), 12083–12091. doi:10.1029/2019GL083980.

Fried MJ and others (2015) Distributed subglacial discharge drives significant submarine melt at a Greenland tidewater glacier. *Geophysical Research Letters* 42(21), 9328–9336.

doi:10.1002/2015GL065806.

Hager AO, Sutherland DA, Amundson JM, Jackson RH, Kienholz C, Motyka RJ and Nash JD (2022) Subglacial Discharge Reflux and Buoyancy Forcing Drive Seasonality in a Silled Glacial Fjord. Journal of Geophysical Research: Oceans, 127(5), 1–21. doi: 10.1029/2021JC018355

Hock R (1999) A distributed temperature-index ice- and snowmelt model including potential direct solar radiation. *Journal of Glaciology* 45(149), 101–111.

Hock R and Noetzli C (1997) Areal melt and discharge modelling of Storglaciären, Sweden. *Annals of Glaciology* 24, 211–216.

Holland DM, Thomas RH, De Young B, Ribergaard MH and Lyberth B (2008) Acceleration of Jakobshavn Isbræ triggered by warm subsurface ocean waters. *Nature Geoscience* 1, 659–664. doi:10.1038/ngeo316.

Holland DM and Jenkins A (1999) Modeling thermodynamic ice-ocean interactions at the base of an ice shelf. *Journal of Physical Oceanography* 29(8), 1787–1800.

Holmes FA, van Dongen E, Noormets R, Pętlicki M and Kirchner N (2022) Modelled 3D calving at Kronebreen, Svalbard, driven by tidal fluctuations and frontal melt. *The Cryosphere Discussions* 20(August), 1–26. https://doi.org/10.5194/tc-2022-152.

How P and others (2019) Calving controlled by melt-under-cutting: Detailed calving styles revealed through time-lapse observations. *Annals of Glaciology* 60(78), 20–31. doi:10.1017/aog.2018.28.

Howat IM, Joughin I, Fahnestock M, Smith BE and Scambos TA (2008) Synchronous retreat and acceleration of southeast Greenland outlet glaciers 2000-06: Ice dynamics and coupling to climate. *Journal of Glaciology* 54(187), 646–660. doi:10.3189/002214308786570908.

Hunter LE and Powell RD (1998) Ice foot development at temperate tidewater margins in Alaska. *Geophysical Research Letters* 25(11), 1923–1926. doi:10.1029/98GL01403.

Jackson RH and others (2022) The Relationship Between Submarine Melt and Subglacial Discharge From Observations at a Tidewater Glacier. *Journal of Geophysical Research: Oceans* 127(10), 1–22. doi:10.1029/2021JC018204.

Jackson RH and others (2020) Meltwater Intrusions Reveal Mechanisms for Rapid Submarine Melt at a Tidewater Glacier. *Geophysical Research Letters* 47. doi:10.1029/2019GL085335.

Jenkins A (2011) Convection-driven melting near the grounding lines of ice shelves and tidewater glaciers. *Journal of Physical Oceanography* 41(12), 2279–2294. doi:10.1175/JPO-D-11-03.1.

Jenkins A (1999) The impact of melting ice on ocean waters. *Journal of Physical Oceanography* 29, 2370–2381.

Jenkins A (1991) A One-Dimensional Model of Ice Shelf-Ocean Interactions. *Journal of Geophysical Research* 96(Cll), 20,671-20,677.

Kerr RC and McConnochie CD (2015) Dissolution of a vertical solid surface by turbulent compositional convection. *Journal of Fluid Mechanics* 765, 211–228. doi:10.1017/jfm.2014.722.

Kienholz C and others (2019) Tracking icebergs with time-lapse photography and sparse optical flow, LeConte Bay, Alaska, 2016-2017. *Journal of Glaciology* 65(250), 195–211. doi:10.1017/jog.2018.105.

Kimura S, Holland PR, Jenkins A and Piggott M (2014) The effect of meltwater plumes on the melting of a vertical glacier face. *Journal of Physical Oceanography* 44(12), 3099–3117. doi:10.1175/JPO-D-13-0219.1.

Kochtitzky W and others (2022) The unquantified mass loss of Northern Hemisphere marine-terminating glaciers from 2000–2020. *Nature Communications* 13(1), 5835. doi:10.1038/s41467-022-33231-x.

Ma Y and Bassis JN (2019) The Effect of Submarine Melting on Calving From Marine Terminating Glaciers. *Journal of Geophysical Research: Earth Surface* 124, 334–346. doi:10.1029/2018JF004820.

Malyarenko A, Wells AJ, Langhorne PJ, Robinson NJ, Williams MJM and Nicholls KW (2020) A synthesis of thermodynamic ablation at ice–ocean interfaces from theory, observations and models. *Ocean Modelling* 154, 101692. doi:10.1016/j.ocemod.2020.101692.

McConnochie CD and Kerr RC (2017) Testing a common ice-ocean parameterization with laboratory experiments. *Journal of Geophysical Research: Oceans* 122(7), 5905–5915. doi:10.1002/2017JC012918.

Mercenier R, Lüthi MP and Vieli A (2020) How Oceanic Melt Controls Tidewater Glacier Evolution. *Geophysical Research Letters* 47. doi:10.1029/2019GL086769.

Mercenier R, Lüthi MP and Vieli A (2019) A Transient Coupled Ice Flow-Damage Model to Simulate Iceberg Calving From Tidewater Outlet Glaciers. *Journal of Advances in Modeling Earth Systems* 11(9), 3057–3072. doi:10.1029/2018MS001567.

Morlighem M, Rignot E, Seroussi H, Larour E, Ben Dhia H and Aubry D (2011) A mass conservation approach for mapping glacier ice thickness. *Geophysical Research Letters* 38(19), 1–6. doi:10.1029/2011GL048659.

Motyka RJ, Dryer WP, Amundson J, Truffer M and Fahnestock M (2013) Rapid submarine melting driven by subglacial discharge, LeConte Glacier, Alaska. *Geophysical Research Letters* 40, 5153–5158. doi:10.1002/grl.51011.

Motyka R, Hunter L, Echelmeyer KA and Connor C (2003) Submarine melting at the terminus of a temperate tidewater glacier, LeConte Glacier, Alaska, U.S.A. *Annals of Glaciology* 36, 57–65.

Motyka RJ, Begét J and Bowen P (1998) Recent retreat of LeConte Glacier and Associated Calving and Iceberg Hazards. Alaska Division of Geological & Geophysical Surveys Report of Investigation 98-15, 9 p. doi: 10.14509/2590

Motyka R (1997) Deep-water calving at Le Conte Glacier, Southeast Alaska. Byrd Polar Research Center, The Ohio State University, Columbus, Ohio.

Mouginot J, Rignot E, Bjørk AA, van den Broeke M, Millan R, Morlighem M, Noël B, Scheuchl B and Wood M (2019) Forty-six years of Greenland Ice Sheet mass balance from 1972 to 2018. Proceedings of the National Academy of Sciences of the United States of America, 116(19), 9239–9244. doi: 10.1073/pnas.1904242116

O'Leary M and Christoffersen P (2013) Calving on tidewater glaciers amplified by submarine frontal melting. *Cryosphere* 7, 119–128. doi:10.5194/tc-7-119-2013.

O'Neel S, Echelmeyer KA and Motyka RJ (2001) Short-term flow dynamics of a retreating tidewater glacier: LeConte Glacier, Alaska, U.S.A. *Journal of Glaciology* 47(159), 567–578. doi:10.3189/172756501781831855.

Podrasky D, Truffer M, Lüthi M and Fahnestock M (2014) Quantifying velocity response to ocean tides and calving near the terminus of Jakobshavn Isbræ, Greenland. *Journal of Glaciology* 60(222), 609–621. doi:10.3189/2014JoG13J130.

Purdie H, Bealing P, Tidey E, Gomez C and Harrison J (2016) Bathymetric evolution of Tasman Glacier terminal lake, New Zealand, as determined by remote surveying techniques. *Global and Planetary Change* 147, 1–11. doi:10.1016/j.gloplacha.2016.10.010.

Rignot E, Fenty I, Xu Y, Cai C and Kemp C (2015) Undercutting of marine-terminating glaciers in West Greenland. *Geophysical Research Letters* 42, 5909–5917. doi:10.1002/2015GL064236.

Robertson CM, Benn DI, Brook MS, Fuller IC and Holt KA (2012) Subaqueous calving margin morphology at Mueller, Hooker and Tasman glaciers in Aoraki/Mount Cook National Park, New Zealand. *Journal of Glaciology* 58(212), 1037–1046. doi:10.3189/2012JoG12J048.

Schulz K, Nguyen AT and Pillar HR (2022) An Improved and Observationally-Constrained Melt

Rate Parameterization for Vertical Ice Fronts of Marine Terminating Glaciers. *Geophysical Research Letters* 49. doi:10.1029/2022gl100654.

Shreve RL (1972) Movement of Water in Glaciers. *Journal of Glaciology* 11(62), 205–214. doi:10.3189/s002214300002219x.

Slater DA and others (2022) Characteristic Depths, Fluxes, and Timescales for Greenland's Tidewater Glacier Fjords From Subglacial Discharge-Driven Upwelling During Summer. *Geophysical Research Letters* 49(10), 1–9. doi:10.1029/2021GL097081.

Slater DA, Benn DI, Cowton TR, Bassis JN and Todd JA (2021) Calving Multiplier Effect Controlled by Melt Undercut Geometry. *Journal of Geophysical Research: Earth Surface* 126(7), 1–17. doi:10.1029/2021JF006191.

Slater DA, Straneo F, Das SB, Richards CG, Wagner TJW and Nienow PW (2018) Localized Plumes Drive Front-Wide Ocean Melting of A Greenlandic Tidewater Glacier. *Geophysical Research Letters* 45, 12,350-12,358. doi:10.1029/2018GL080763.

Slater DA, Nienow PW, Goldberg DN, Cowton TR and Sole AJ (2017) A model for tidewater glacier undercutting by submarine melting. *Geophysical Research Letters* 44, 2360–2368. doi:10.1002/2016GL072374.

Slater DA, Nienow PW, Cowton TR, Goldberg DN and Sole AJ (2015) Effect of near-terminus subglacial hydrology on tidewater glacier submarine melt rates. *Geophysical Research Letters* 42, 2861–2868. doi:10.1080/10550887.2011.581988.

Straneo F and others (2013) Challenges to understanding the dynamic response of Greenland's marine terminating glaciers to oceanic and atmospheric forcing. *Bulletin of the American Meteorological Society* 94(8), 1131–1144. doi:10.1175/BAMS-D-12-00100.1.

Sugiyama S, Minowa M and Schaefer M (2019) Underwater Ice Terrace Observed at the Front of Glaciar Grey, a Freshwater Calving Glacier in Patagonia. *Geophysical Research Letters* 46(5), 2602–2609. doi:10.1029/2018GL081441.

Sutherland DA and others (2019) Direct observations of submarine melt and subsurface geometry at a tidewater glacier. *Science* 365, 369–374. doi:10.1126/science.aax3528.

Wagner TJW and others (2019) Large spatial variations in the flux balance along the front of a Greenland tidewater glacier. *Cryosphere* 13, 911–925. doi:10.5194/tc-13-911-2019.

Wagner TJW, James TD, Murray T and Vella D (2016) On the role of buoyant flexure in glacier calving. *Geophysical Research Letters* 43, 232–240. doi:10.1002/2015GL067247.

Warren C, Benn D, Winchester V and Harrison S (2001) Buoyancy-driven lacustrine calving, Glaciar Nef, Chilean Patagonia. *Journal of Glaciology* 47(156), 135–146. doi:10.3189/172756501781832403.

Wood M and others (2018) Ocean-Induced Melt Triggers Glacier Retreat in Northwest Greenland. *Geophysical Research Letters* 45(16), 8334–8342. doi:10.1029/2018GL078024.

CHAPTER III

Amundson, J. M., Fahnestock, M., Truffer, M., Brown, J., Lüthi, M. P., and Motyka, R. J.: Ice mélange dynamics and implications for terminus stability, Jakobshavn Isbrse, Greenland, J Geophys Res Earth Surf, 115, 1–12, https://doi.org/10.1029/2009JF001405, 2010.

Bao, W. and Moffat, C.: Impact of shallow sills on circulation regimes and submarine melting in glacial fjords, Cryosphere, 18, 187–203, https://doi.org/10.5194/tc-18-187-2024, 2024.

Bartholomaus, T. C., Stearns, L. A., Sutherland, D. A., Shroyer, E. L., Nash, J. D., Walker, R. T., Catania, G., Felikson, D., Carroll, D., Fried, M. J., Noël, B. P. Y., and Van Den Broeke, M. R.: Contrasts in the response of adjacent fjords and glaciers to ice-sheet surface melt in West Greenland, Ann Glaciol, 57, 25–38, https://doi.org/10.1017/aog.2016.19, 2016.

Beaird, N., Straneo, F., and Jenkins, W.: Spreading of Greenland meltwaters in the ocean revealed by noble gases, Geophys Res Lett, 42, 7705–7713, https://doi.org/10.1002/2015GL065003, 2015.

Carnahan, E., Catania, G., and Bartholomaus, T. C.: Observed mechanism for sustained glacier retreat and acceleration in response to ocean warming around Greenland, Cryosphere, 16, 4305–4317, https://doi.org/10.5194/tc-16-4305-2022, 2022.

Carroll, D., Sutherland, D. A., Shroyer, E. L., Nash, J. D., Catania, G. A., and Stearns, L. A.: Modeling turbulent subglacial meltwater plumes: Implications for fjord-scale buoyancy-driven circulation, J Phys Oceanogr, 45, 2169–2185, https://doi.org/10.1175/JPO-D-15-0033.1, 2015.

Carroll, D., Sutherland, D. A., Hudson, B., Moon, T., Catania, G. A., Shroyer, E. L., Nash, J. D., Bartholomaus, T. C., Felikson, D., Stearns, L. A., Noël, B. P. Y., and van den Broeke, M. R.: The impact of glacier geometry on meltwater plume structure and submarine melt in Greenland fjords, Geophys Res Lett, 43, 9739–9748, https://doi.org/10.1002/2016GL070170, 2016.

Carroll, D., Sutherland, D. A., Shroyer, E. L., Nash, J. D., Catania, G. A., and Stearns, L. A.: Subglacial discharge-driven renewal of tidewater glacier fjords, J Geophys Res Oceans, 122, https://doi.org/10.1002/2017JC012962, 2017.

Carroll, D., Sutherland, D. A., Curry, B., Nash, J. D., Shroyer, E. L., Catania, G. A., Stearns, L. A., Grist, J. P., Lee, C. M., and de Steur, L.: Subannual and Seasonal Variability of Atlantic-Origin Waters in Two Adjacent West Greenland Fjords, J Geophys Res Oceans, 123, 6670–6687, https://doi.org/10.1029/2018JC014278, 2018.

Catania, G. A., Stearns, L. A., Sutherland, D. A., Fried, M. J., Bartholomaus, T. C., Morlighem, M., Shroyer, E., and Nash, J.: Geometric Controls on Tidewater Glacier Retreat in Central Western Greenland, J Geophys Res Earth Surf, 123, 2024–2038, https://doi.org/10.1029/2017JF004499, 2018.

Catania, G., Stearns, L., Sutherland, D., Shroyer, E., and Nash, J.: Water temperature, salinity and hydrostatic pressure collected from subsurface moorings deployed by the research vessel Sanna in the Uummannaq Bay, west Greenland, from 2013-09-17 to 2015-07-12, NOAA National Centers for Environmental Information [data set], https://www.ncei.noaa.gov/archive/accession/0173969, 2018.

Cenedese, C. and Straneo, F.: Icebergs Melting, https://doi.org/10.1146/annurev-fluid-032522-100734, 2023.

Chauché, N., Hubbard, A., Gascard, J. C., Box, J. E., Bates, R., Koppes, M., Sole, A., Christoffersen, P., and Patton, H.: Ice-ocean interaction and calving front morphology at two west Greenland tidewater outlet glaciers, Cryosphere, 8, 1457–1468, https://doi.org/10.5194/tc-8-1457-2014, 2014.

Cowton, T., Sole, A., Nienow, P., Slater, D. A., Wilton, D., and Hanna, E.: Controls on the transport of oceanic heat to Kangerdlugssuaq Glacier, East Greenland, Journal of Glaciology, 62, 1167–1180, https://doi.org/10.1017/jog.2016.117, 2016.

Cowton, T. R., Sole, A. J., Nienow, P. W., Slater, D. A., and Christoffersen, P.: Linear response of east Greenland's tidewater glaciers to ocean/atmosphere warming, Proc Natl Acad Sci U S A, 115, 7907–7912, https://doi.org/10.1073/pnas.1801769115, 2018.

Davison, B. J., Cowton, T. R., Cottier, F. R., and Sole, A. J.: Iceberg melting substantially modifies oceanic heat flux towards a major Greenlandic tidewater glacier, Nat Commun, 11, https://doi.org/10.1038/s41467-020-19805-7, 2020.

Davison, B. J., Cowton, T., Sole, A., Cottier, F., and Nienow, P.: Modelling the effect of submarine iceberg melting on glacier-adjacent water properties, Cryosphere, 16, 1181–1196, https://doi.org/10.5194/tc-16-1181-2022, 2022.

Enderlin, E. M., Hamilton, G. S., Straneo, F., and Sutherland, D. A.: Iceberg meltwater fluxes dominate the freshwater budget in Greenland's iceberg-congested glacial fjords, Geophys Res Lett, 43, 11,287-11,294, https://doi.org/10.1002/2016GL070718, 2016.

Fahrner, D., Lea, J. M., Brough, S., Mair, D. W. F., and Abermann, J.: Linear response of the Greenland ice sheet's tidewater glacier terminus positions to climate, Journal of Glaciology, 67, 193–203, https://doi.org/10.1017/jog.2021.13, 2021.

FitzMaurice, A., Straneo, F., Cenedese, C., and Andres, M.: Effect of a sheared flow on iceberg motion and melting, Geophys Res Lett, 43, 12,520-12,527, https://doi.org/10.1002/2016GL071602, 2016.

Fried, M. J., Catania, G. A., Stearns, L. A., Sutherland, D. A., Bartholomaus, T. C., Shroyer, E., and Nash, J.: Reconciling Drivers of Seasonal Terminus Advance and Retreat at 13 Central West Greenland Tidewater Glaciers, J Geophys Res Earth Surf, 123, 1590–1607, https://doi.org/10.1029/2018JF004628, 2018.

Gade, H. G.: Melting of Ice in Sea Water: A Primitive Model with Application to the Antarctic Ice Shelf and Icebergs, J Phys Oceanogr, 189–198, 1979.

Greene, C. A., Gardner, A. S., Wood, M., and Cuzzone, J. K.: Ubiquitous acceleration in Greenland Ice Sheet calving from 1985 to 2022, Nature, 625, 523–528, https://doi.org/10.1038/s41586-023-06863-2, 2024.

Hager, A. O., Sutherland, D. A., and Slater, D. A.: Local forcing mechanisms challenge parameterizations of ocean thermal forcing for Greenland tidewater glaciers, EGUsphere, 2023, 1–33, https://doi.org/10.5194/egusphere-2023-746, 2023.

Howat, I. M., Box, J. E., Ahn, Y., Herrington, A., and McFadden, E. M.: Seasonal variability in the dynamics of marine-terminating outlet glaciers in Greenland, Journal of Glaciology, 56, 601–613, https://doi.org/10.3189/002214310793146232, 2010.

Jackson, R. H., Shroyer, E. L., Nash, J. D., Sutherland, D. A., Carroll, D., Fried, M. J., Catania, G. A., Bartholomaus, T. C., and Stearns, L. A.: Near-glacier surveying of a subglacial discharge plume: Implications for plume parameterizations, Geophys Res Lett, 44, 6886–6894, https://doi.org/10.1002/2017GL073602, 2017.

Jackson, R. H., Nash, J. D., Kienholz, C., Sutherland, D. A., Amundson, J. M., Motyka, R. J., Winters, D., Skyllingstad, E., and Pettit, E. C.: Meltwater Intrusions Reveal Mechanisms for Rapid Submarine Melt at a Tidewater Glacier, Geophys Res Lett, 47, https://doi.org/10.1029/2019GL085335, 2020.

Jenkins, A.: The Impact of Melting Ice on Ocean Waters, J Phys Oceanogr, 29, 2370–2381, https://doi.org/10.1175/1520-0485(1999)029<2370:TIOMIO>2.0.CO;2, 1999.

Joughin, I., Howat, I. M., Fahnestock, M., Smith, B., Krabill, W., Alley, R. B., Stern, H., and Truffer, M.: Continued evolution of Jakobshavn Isbrae following its rapid speedup, J Geophys Res Earth Surf, 113, 1–14, https://doi.org/10.1029/2008JF001023, 2008.

Kajanto, K., Straneo, F., and Nisancioglu, K.: Impact of icebergs on the seasonal submarine melt of Sermeq Kujalleq, Cryosphere, 17, 371–390, https://doi.org/10.5194/tc-17-371-2023, 2023.

Kimura, S., Holland, P. R., Jenkins, A., and Piggott, M.: The effect of meltwater plumes on the melting of a vertical glacier face, J Phys Oceanogr, 44, 3099–3117, https://doi.org/10.1175/JPO-D-13-0219.1, 2014.

King, M. D., Howat, I. M., Jeong, S., Noh, M. J., Wouters, B., Noël, B., and Van Den Broeke, M. R.: Seasonal to decadal variability in ice discharge from the Greenland Ice Sheet, Cryosphere, 12, 3813–3825, https://doi.org/10.5194/tc-12-3813-2018, 2018.

King, M. D., Howat, I. M., Candela, S. G., Noh, M. J., Jeong, S., Noël, B. P. Y., van den Broeke, M. R., Wouters, B., and Negrete, A.: Dynamic ice loss from the Greenland Ice Sheet driven by sustained glacier retreat, Commun Earth Environ, 1, 1–7, https://doi.org/10.1038/s43247-020-0001-2, 2020.

Krug, J., Durand, G., Gagliardini, O., and Weiss, J.: Modelling the impact of submarine frontal melting and ice mélange on glacier dynamics, Cryosphere, 9, 989–1003, https://doi.org/10.5194/tc-9-989-2015, 2015.

Mankoff, K. D., Noël, B., Fettweis, X., Ahlstrøm, A. P., Colgan, W., Kondo, K., Langley, K., Sugiyama, S., Van As, D., and Fausto, R. S.: Greenland liquid water discharge from 1958 through 2019, Earth Syst Sci Data, 12, 2811–2841, https://doi.org/10.5194/essd-12-2811-2020, 2020.

McDougall, T. J. and Barker, P. M.: Getting started with TEOS-10 and the Gibbs Seawater (GSW) Oceanographic Toolbox, 28 pp., 2011.

Millan, R., Jager, E., Mouginot, J., Wood, M. H., Larsen, S. H., Mathiot, P., Jourdain, N. C., and Bjørk, A.: Rapid disintegration and weakening of ice shelves in North Greenland, Nat Commun, 14, 1–10, https://doi.org/10.1038/s41467-023-42198-2, 2023.

Moon, T., Sutherland, D. A., Carroll, D., Felikson, D., Kehrl, L., and Straneo, F.: Subsurface iceberg melt key to Greenland fjord freshwater budget, Nat Geosci, 11, 49–54, https://doi.org/10.1038/s41561-017-0018-z, 2018.

Morlighem, M., Williams, C. N., Rignot, E., An, L., Arndt, J. E., Bamber, J. L., Catania, G., Chauché, N., Dowdeswell, J. A., Dorschel, B., Fenty, I., Hogan, K., Howat, I., Hubbard, A., Jakobsson, M., Jordan, T. M., Kjeldsen, K. K., Millan, R., Mayer, L., Mouginot, J., Noël, B. P. Y., O'Cofaigh, C., Palmer, S., Rysgaard, S., Seroussi, H., Siegert, M. J., Slabon, P., Straneo, F., van den Broeke, M. R., Weinrebe, W., Wood, M., and Zinglersen, K. B.: BedMachine v3: Complete Bed Topography and Ocean Bathymetry Mapping of Greenland From Multibeam Echo Sounding Combined With Mass Conservation, Geophys Res Lett, 44, 11,051-11,061, https://doi.org/10.1002/2017GL074954, 2017.

Morlighem, M., Williams, C., Rignot, E., An, L., Arndt, J. E., Bamber, J., Catania, G., Chauché, N., Dowdeswell, J. A., Dorschel, B., Fenty, I., Hogan, K., Howat, I., Hubbard, A., Jakobsson, M., Jordan, T. M., Kjeldsen, K. K., Millan, R., Mayer, L., Mouginot, J., Noël, B., O'Cofaigh, C., Palmer, S. J., Rysgaard, S., Seroussi, H., Siegert, M. J., Slabon, P., Straneo, F., van den Broeke, M. R., Weinrebe, W., Wood, M., and Zinglersen, K.: IceBridge BedMachine Greenland, Version 5, NASA National Snow and Ice Data Center

Distributed Active Archive Center [data set]. https://doi.org/10.5067/GMEVBWFLWA7X, 2022.

Murray, T., Scharrer, K., James, T. D., Dye, S. R., Hanna, E., Booth, A. D., Selmes, N., Luckman, A., Hughes, A. L. C., Cook, S., and Huybrechts, P.: Ocean regulation hypothesis for glacier dynamics in southeast Greenland and implications for ice sheet mass changes, J Geophys Res Earth Surf, 115, 1–15, https://doi.org/10.1029/2009JF001522, 2010.

Nick, F. M., Vieli, A., Howat, I. M., and Joughin, I.: Large-scale changes in Greenland outlet glacier dynamics triggered at the terminus, Nat Geosci, 2, 110–114, https://doi.org/10.1038/ngeo394, 2009.

Noël, B., Van De Berg, W. J., Van Meijgaard, E., Kuipers Munneke, P., Van De Wal, R. S. W., and Van Den Broeke, M. R.: Evaluation of the updated regional climate model RACMO2.3: Summer snowfall impact on the Greenland Ice Sheet, Cryosphere, 9, 1831–1844, https://doi.org/10.5194/tc-9-1831-2015, 2015.

Slater, D. A., Goldberg, D. N., Nienow, P. W., and Cowton, T. R.: Scalings for submarine melting at tidewater glaciers from buoyant plume theory, J Phys Oceanogr, 46, 1839–1855, https://doi.org/10.1175/JPO-D-15-0132.1, 2016.

Slater, D. A., Nienow, P. W., Goldberg, D. N., Cowton, T. R., and Sole, A. J.: A model for tidewater glacier undercutting by submarine melting, Geophys Res Lett, 44, 2360–2368, https://doi.org/10.1002/2016GL072374, 2017a.

Slater, D. A., Nienow, P., Sole, A., Cowton, T., Mottram, R., Langen, P., and Mair, D.: Spatially distributed runoff at the grounding line of a large Greenlandic tidewater glacier inferred from plume modelling, Journal of Glaciology, 63, 309–323, https://doi.org/10.1017/jog.2016.139, 2017b.

Slater, D. A., Carroll, D., Oliver, H., Hopwood, M. J., Straneo, F., Wood, M., Willis, J. K., and Morlighem, M.: Characteristic Depths, Fluxes, and Timescales for Greenland's Tidewater Glacier Fjords From Subglacial Discharge-Driven Upwelling During Summer, Geophys Res Lett, 49, 1–9, https://doi.org/10.1029/2021GL097081, 2022.

Straneo, F. and Cenedese, C.: The dynamics of greenland's glacial fjords and their role in climate, Ann Rev Mar Sci, 7, 89–112, https://doi.org/10.1146/annurev-marine-010213-135133, 2015.

Straneo, F., Sutherland, D. A., Holland, D., Gladish, C., Hamilton, G. S., Johnson, H. L., Rignot, E., Xu, Y., and Koppes, M.: Characteristics of ocean waters reaching greenland's glaciers, Ann Glaciol, 53, 202–210, https://doi.org/10.3189/2012AoG60A059, 2012.

Sulak, D. J., Sutherland, D. A., Enderlin, E. M., Stearns, L. A., and Hamilton, G. S.: Iceberg properties and distributions in three Greenlandic fjords using satellite imagery, Ann Glaciol, 58, 92–106, https://doi.org/10.1017/aog.2017.5, 2017.

Wilson, N., Straneo, F., and Heimbach, P.: Satellite-derived submarine melt rates and mass balance (2011-2015) for Greenland's largest remaining ice tongues, Cryosphere, 11, 2773–2782, https://doi.org/10.5194/tc-11-2773-2017, 2017.

Wood, M., Rignot, E., Fenty, I., An, L., Bjørk, A., Broeke, M. Van Den, Cai, C., Kane, E., Menemenlis, D., Millan, R., Morlighem, M., Mouginot, J., Noël, B., Scheuchl, B., Velicogna, I., Willis, J. K., and Zhang, H.: Ocean forcing drives glacier retreat in Greenland, Sci Adv, 7, 1–10, 2021.

Xu, Y., Rignot, E., Fenty, I., Menemenlis, D., and Flexas, M. M.: Subaqueous melting of Store Glacier, west Greenland from three-dimensional, high-resolution numerical modeling and ocean observations, Geophys Res Lett, 40, 4648–4653, https://doi.org/10.1002/grl.50825, 2013.

Zhao, K. X., Stewart, A. L., McWilliams, J. C., Fenty, I. G., and Rignot, E. J.: Standing Eddies in Glacial Fjords and Their Role in Fjord Circulation and Melt, J Phys Oceanogr, 53, 821–840, https://doi.org/10.1175/JPO-D-22-0085.1, 2023.

CHAPTER IV

Abib N and others (2024) Ice mélange melt drives changes in observed water column stratification at a tidewater glacier in Greenland. *The Cryosphere Discussions* (March), 1–21. doi:10.5194/egusphere-2024-504.

Amundson JM, Robel AR, Burton JC and Nissanka K (2024) A quasi-one-dimensional ice mélange flow model based on continuum descriptions of granular materials. *The Cryosphere Discussions* (March), 1–26.

Amundson JM and others (2020) Formation, flow and break-up of ephemeral ice mélange at LeConte Glacier and Bay, Alaska. *Journal of Glaciology*, 1–14. doi:10.1017/jog.2020.29.

Amundson JM, Fahnestock M, Truffer M, Brown J, Lüthi MP and Motyka RJ (2010) Ice mélange dynamics and implications for terminus stability, Jakobshavn Isbrse, Greenland. *Journal of Geophysical Research: Earth Surface* 115(1), 1–12. doi:10.1029/2009JF001405.

Bartholomaus TC and others (2016) Contrasts in the response of adjacent fjords and glaciers to ice-sheet surface melt in West Greenland. *Annals of Glaciology* 57(73), 25–38. doi:10.1017/aog.2016.19.

Black, TE and Joughin I (2022) MEaSUREs Weekly-To-Monthly Greenland Outlet Glacier Terminus Positions from Sentinel-1 Mosaics, Version 1. Boulder, Colorado USA. NASA

National Snow and Ice Data Center Distributed Active Archive Center. https://doi.org/10.5067/DGBOSSIULSTD. [02-07-2024].

Burton JC, Amundson JM, Cassotto R, Kuo CC and Dennin M (2018) Quantifying flow and stress in ice mélange, the world's largest granular material. *Proceedings of the National Academy of Sciences of the United States of America* 115(20), 5105–5110. doi:10.1073/pnas.1715136115.

Carnahan E, Catania G and Bartholomaus TC (2022) Observed mechanism for sustained glacier retreat and acceleration in response to ocean warming around Greenland. *Cryosphere* 16(10), 4305–4317. doi:10.5194/tc-16-4305-2022.

Carroll D and others (2018) Subannual and Seasonal Variability of Atlantic-Origin Waters in Two Adjacent West Greenland Fjords. *Journal of Geophysical Research: Oceans* 123, 6670–6687. doi:10.1029/2018JC014278.

Carroll D, Sutherland DA, Shroyer EL, Nash JD, Catania GA and Stearns LA (2017) Subglacial discharge-driven renewal of tidewater glacier fjords. *Journal of Geophysical Research: Oceans* 122. doi:10.1002/2017JC012962.

Carroll D and others (2016) The impact of glacier geometry on meltwater plume structure and submarine melt in Greenland fjords. *Geophysical Research Letters* 43, 9739–9748. doi:10.1002/2016GL070170.

Cassotto RK, Burton JC, Amundson JM, Fahnestock MA and Truffer M (2021) Granular decoherence precedes ice mélange failure and glacier calving at Jakobshavn Isbræ. *Nature Geoscience* 14(6), 417–422. doi:10.1038/s41561-021-00754-9.

Cassotto R, Fahnestock M, Amundson JM, Truffer M and Joughin I (2015) Seasonal and interannual variations in ice melange and its impact on terminus stability, Jakobshavn Isbræ, Greenland. *Journal of Glaciology* 61(225), 76–88. doi:10.3189/2015JoG13J235.

Catania GA and others (2018) Geometric Controls on Tidewater Glacier Retreat in Central Western Greenland. *Journal of Geophysical Research: Earth Surface* 123(8), 2024–2038. doi:10.1029/2017JF004499.

Chauché N and others (2014) Ice-ocean interaction and calving front morphology at two west Greenland tidewater outlet glaciers. *Cryosphere* 8(4), 1457–1468. doi:10.5194/tc-8-1457-2014.

Chudley TR, Howat IM, King MD and Negrete A (2023) Atlantic water intrusion triggers rapid retreat and regime change at previously stable Greenland glacier. *Nature Communications* 14(1), 1–10. doi:10.1038/s41467-023-37764-7.

Cowton T, Sole A, Nienow P, Slater DA, Wilton D and Hanna E (2016) Controls on the transport of oceanic heat to Kangerdlugssuaq Glacier, East Greenland. *Journal of Glaciology* 62(236), 1167–1180. doi:10.1017/jog.2016.117.

Davison BJ, Cowton T, Sole A, Cottier F and Nienow P (2022) Modelling the effect of submarine iceberg melting on glacier-adjacent water properties. *Cryosphere* 16(4), 1181–1196. doi:10.5194/tc-16-1181-2022.

Davison BJ, Cowton TR, Cottier FR and Sole AJ (2020) Iceberg melting substantially modifies oceanic heat flux towards a major Greenlandic tidewater glacier. *Nature Communications* 11(5983). doi:10.1038/s41467-020-19805-7.

Enderlin EM, Carrigan CJ, Kochtitzky WH, Cuadros A, Moon T and Hamilton GS (2018) Greenland iceberg melt variability from high-resolution satellite observations. *Cryosphere* 12, 565–575. doi:10.5194/tc-12-565-2018.

Enderlin EM, Hamilton GS, Straneo F and Sutherland DA (2016) Iceberg meltwater fluxes dominate the freshwater budget in Greenland's iceberg-congested glacial fjords. *Geophysical Research Letters* 43(21), 11,287-11,294. doi:10.1002/2016GL070718.

Fried MJ and others (2018) Reconciling Drivers of Seasonal Terminus Advance and Retreat at 13 Central West Greenland Tidewater Glaciers. *Journal of Geophysical Research: Earth Surface* 123(7), 1590–1607. doi:10.1029/2018JF004628.

Greene CA, Gardner AS, Wood M and Cuzzone JK (2024) Ubiquitous acceleration in Greenland Ice Sheet calving from 1985 to 2022. *Nature* 625(7995), 523–528. doi:10.1038/s41586-023-06863-2.

Hager AO, Sutherland DA and Slater DA (2024) Local forcing mechanisms challenge parameterizations of ocean thermal forcing for Greenland tidewater glaciers. *The Cryosphere* 18(2), 911–932. doi:10.5194/tc-18-911-2024.

Hersbach, H, Bell, B, Berrisford, P, Biavati, G, Horányi, A, Muñoz Sabater, J, Nicolas, J, Peubey, C, Radu, R., Rozum, I, Schepers, D, Simmons, A, Soci, C, Dee, D, and Thépaut, J-N (2023) ERA5 hourly data on single levels from 1940 to present. Copernicus Climate Change Service (C3S) Climate Data Store (CDS), DOI: 10.24381/cds.adbb2d47 (Accessed on 02-07-2024)

Howat IM, Box JE, Ahn Y, Herrington A and McFadden EM (2010) Seasonal variability in the dynamics of marine-terminating outlet glaciers in Greenland. *Journal of Glaciology* 56(198), 601–613. doi:10.3189/002214310793146232.

Hughes KG (2022) Pathways, Form Drag, and Turbulence in Simulations of an Ocean Flowing Through an Ice Mélange. *Journal of Geophysical Research: Oceans* 127(6), 1–17. doi:10.1029/2021JC018228.

Jackson RH and others (2017) Near-glacier surveying of a subglacial discharge plume: Implications for plume parameterizations. *Geophysical Research Letters* 44, 6886–6894. doi:10.1002/2017GL073602.

Jenkins A (2011) Convection-driven melting near the grounding lines of ice shelves and tidewater glaciers. *Journal of Physical Oceanography* 41(12), 2279–2294. doi:10.1175/JPO-D-11-03.1.

Joughin I, E. Shean D, E. Smith B and Floricioiu D (2020) A decade of variability on Jakobshavn Isbræ: Ocean temperatures pace speed through influence on mélange rigidity. *Cryosphere* 14, 211–227. doi:10.5194/tc-14-211-2020.

Joughin I and others (2008) Continued evolution of Jakobshavn Isbrae following its rapid speedup. *Journal of Geophysical Research: Earth Surface* 113, 1–14. doi:10.1029/2008JF001023.

Kajanto K, Straneo F and Nisancioglu K (2023) Impact of icebergs on the seasonal submarine melt of Sermeq Kujalleq. *Cryosphere* 17(1), 371–390. doi:10.5194/tc-17-371-2023.

Khazendar Al and others (2019) Interruption of two decades of Jakobshavn Isbrae acceleration and thinning as regional ocean cools. *Nature Geoscience* 12, 277–283. doi:10.1038/s41561-019-0329-3.

Kochtitzky W and others (2022) The unquantified mass loss of Northern Hemisphere marine-terminating glaciers from 2000–2020. *Nature Communications* 13(1), 5835. doi:10.1038/s41467-022-33231-x.

Lea JM (2018) The Google Earth Engine Digitisation Tool (GEEDiT) and the Margin change Quantification Tool (MaQiT) - simple tools for the rapid mapping and quantification of changing Earth surface margins. *Earth Surface Dynamics* 6, 551–561. doi:10.5194/esurf-6-551-2018.

Mankoff KD, Solgaard A, Colgan W, Ahlstrøm AP, Abbas Khan S and Fausto RS (2020) Greenland Ice Sheet solid ice discharge from 1986 through March 2020. *Earth System Science Data* 12(2), 1367–1383. doi:10.5194/essd-12-1367-2020.

Mankoff KD and others (2020) Greenland liquid water discharge from 1958 through 2019. *Earth System Science Data* 12(4), 2811–2841. doi:10.5194/essd-12-2811-2020.

McDougall TJ and Barker PM (2011) *Getting started with TEOS-10 and the Gibbs Seawater (GSW) Oceanographic Toolbox.* http://www.teos-10.org/pubs/gsw/v3_04/pdf/Getting_Started.pdf.

Morlighem M and others (2017) BedMachine v3: Complete Bed Topography and Ocean Bathymetry Mapping of Greenland From Multibeam Echo Sounding Combined With

Mass Conservation. *Geophysical Research Letters* 44, 11,051-11,061. doi:10.1002/2017GL074954.

Mouginot J and others (2019) Forty-six years of Greenland Ice Sheet mass balance from 1972 to 2018. *Proceedings of the National Academy of Sciences of the United States of America* 116(19), 9239–9244. doi:10.1073/pnas.1904242116.

Murray T and others (2010) Ocean regulation hypothesis for glacier dynamics in southeast Greenland and implications for ice sheet mass changes. *Journal of Geophysical Research: Earth Surface* 115(3), 1–15. doi:10.1029/2009JF001522.

Nick FM, Vieli A, Howat IM and Joughin I (2009) Large-scale changes in Greenland outlet glacier dynamics triggered at the terminus. *Nature Geoscience* 2(2), 110–114. doi:10.1038/ngeo394.

Shiggins CJ, Lea JM and Brough S (2023) Automated ArcticDEM iceberg detection tool: insights into area and volume distributions, and their potential application to satellite imagery and modelling of glacier-iceberg-ocean systems. *Cryosphere* 17(1), 15–32. doi:10.5194/tc-17-15-2023.

Slater DA and others (2022) Characteristic Depths, Fluxes, and Timescales for Greenland's Tidewater Glacier Fjords From Subglacial Discharge-Driven Upwelling During Summer. *Geophysical Research Letters* 49(10), 1–9. doi:10.1029/2021GL097081.

Slater DA and others (2020) Twenty-first century ocean forcing of the Greenland ice sheet for modelling of sea level contribution. *Cryosphere* 14, 985–1008. doi:10.5194/tc-14-985-2020.

Slater DA, Goldberg DN, Nienow PW and Cowton TR (2016) Scalings for submarine melting at tidewater glaciers from buoyant plume theory. *Journal of Physical Oceanography* 46(6), 1839–1855. doi:10.1175/JPO-D-15-0132.1.

Straneo F and others (2012) Characteristics of ocean waters reaching greenland's glaciers. *Annals of Glaciology* 53(60), 202–210. doi:10.3189/2012AoG60A059.

Straneo F and Heimbach P (2013) North Atlantic warming and the retreat of Greenland's outlet glaciers. *Nature* 504(7478), 36–43. doi:10.1038/nature12854.

Sulak DJ, Sutherland DA, Enderlin EM, Stearns LA and Hamilton GS (2017) Iceberg properties and distributions in three Greenlandic fjords using satellite imagery. *Annals of Glaciology* 58(74), 92–106. doi:10.1017/aog.2017.5.

Todd J and Christoffersen P (2014) Are seasonal calving dynamics forced by buttressing from ice mélange or undercutting by melting? Outcomes from full-Stokes simulations of Store Glacier, West Greenland. *Cryosphere* 8, 2353–2365. doi:10.5194/tc-8-2353-2014.

Walter JI and others (2012) Oceanic mechanical forcing of a marine-terminating greenland glacier. *Annals of Glaciology* 53(60), 181–192. doi:10.3189/2012AoG60A083.

Wood M and others (2021) Ocean forcing drives glacier retreat in Greenland. *Science Advances* 7(1), 1–10.

Wood M and others (2018) Ocean-Induced Melt Triggers Glacier Retreat in Northwest Greenland. *Geophysical Research Letters* 45(16), 8334–8342. doi:10.1029/2018GL078024.